Chapter 9
Renewable Energies

9.1 Introduction

As mentioned in Chapter 2, there are a number of fundamental sources of energy on earth, such as solar radiation, geothermal heat, and earth spinning combined with gravitational forces of the moon–Earth–sun planetary system. These kinds of energy sources are said to be renewable in the sense that they are never depleted. In contrast, other energy resources, such as fossil fuels (coal, natural gas, petroleum) and nuclear fuels (uranium, thorium), are nonrenewable and thus limited. Among the fundamental energy sources, solar energy is the only one that manifests in a multitude of direct and indirect forms on earth. The indirect forms of solar energy also have the attribute of being renewable; they are wind, waves, hydro energy, ocean thermal energy, and biomass energy. Figure 9.1 classifies the renewable energies.

Common to all renewable energies are these features: they are intermittent, fluctuant in intensity, and regionally or globally available. For example, solar energy is globally available (at every point of the earth's surface), but intermittent—it manifests during daytime between sunrise and sunset; geothermal energy is available locally, that is only in some regions of the earth, such as close to a volcano or to places with more intensive tectonic activity. Wind energy is mostly available over plains or open waters such as large lakes and ocean shores; this energy occurs intermittently, being strong in some seasons or not manifesting at all for some period of times. Tides occur along some ocean shores and are intermittent in nature.

Due to these intermittent-fluctuating and local features, special engineered systems must be devised to harvest and convert the renewable energies into more useful forms. Moreover, energy storage systems are applied to smooth the fluctuation in the primary source and to make the energy available, when possible, at all times.

Recall that in Chapter 2 the outlook for primary energy source availability on earth was analyzed, among which renewables are a part. In this chapter, the renewable energy features are analyzed in more detail, and the systems used to harvest and convert these energies are presented. In general, the aim of renewable energy systems is ultimately to convert these energies into commodities such as electric energy, thermal energy, chemical energy (stored in the form of fuels),

İ. Dinçer and C. Zamfirescu, *Sustainable Energy Systems and Applications*,
DOI 10.1007/978-0-387-95861-3_9,

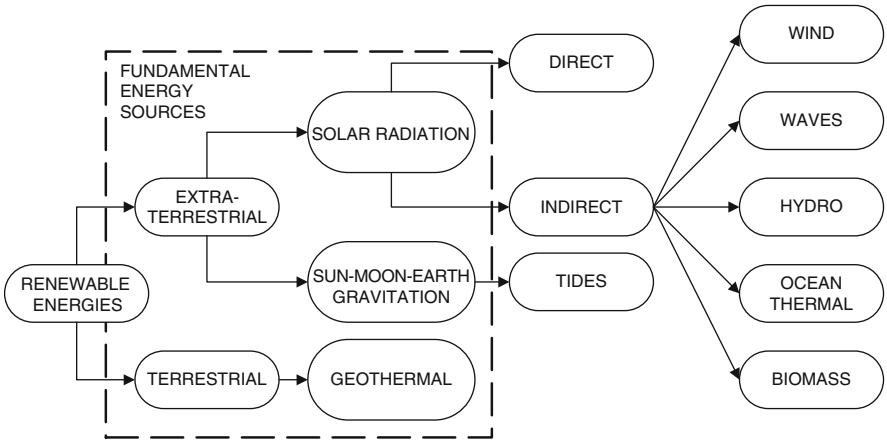

Fig. 9.1 Classification of renewable energies

potential energy (e.g., hydro energy), mechanical energy (e.g., compressed air energy), or biochemical energy (e.g., foods). Each kind of energy is discussed in detail in this chapter, together with the associated systems to convert, store, and use it.

9.2 Solar Energy

Figure 2.3 in Chapter 2 shows that from the total energy of the extraterrestrial solar radiation incident on earth's troposphere, 43% is direct beam radiation, 22% is hydro energy, 0.21% is wind energy, 0.02% is consumed by photosynthesis, and some minute percent is consumed by wave energy; the rest is dissipated into the atmosphere in other ways or reflected back in the extraterrestrial space. Therefore, the largest percent of solar radiation available for conversion on earth is direct beam radiation. This section analyzes especially direct beam radiation and its conversion into electricity and heat. However, some issues regarding diffuse radiation are also considered as they are important in solar energy conversion in many instances.

The basic conversion paths for converting direct solar radiation into other useful forms through engineered systems and devices are illustrated in Fig. 9.2. In principle, direct solar radiation can be converted using special "engineered" devices directly into electrical energy, thermal energy, chemical energy, biochemical energy, or it can be used "unconverted" as photonic energy. In the last form, solar energy is used as light—as the visible spectrum of solar radiation illuminates the earth's surface during the day.

When converted directly to electrical energy (e.g., through photovoltaic panels or other devices) solar energy can be transmitted to the electric grid, can be directly consumed, or can be stored (either as electric charge or by other mean of storing electric energy in other forms, viz. electric batteries, etc., see Chapter 11), or it can

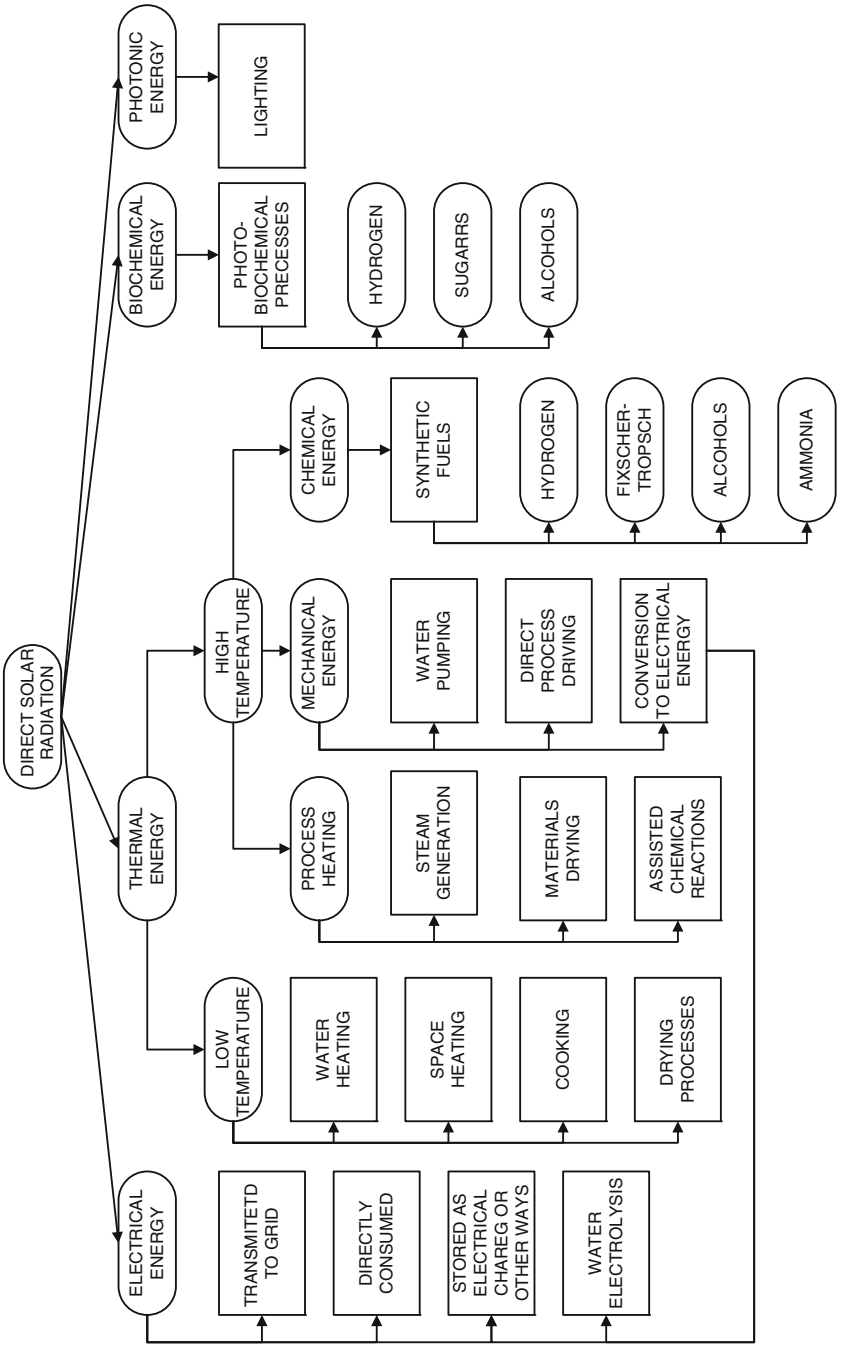

Fig. 9.2 Conversion paths of direct solar radiation with engineered systems

be converted into hydrogen through water electrolysis (see Chapter 13). When converted into thermal energy, low-, intermediate-, high-, or very high-temperature heat can be obtained (starting from the ambient temperature up to around 1,800°C). The low-temperature heat then can be used for water and space heating, for cooking, steam generation, process drying (like food drying, crop drying, paper pulp drying, etc.). Very high-temperature heat—obtained from concentrated solar radiation—can be used for process heating (including processes like thermally driven refrigeration, industrial processes, chemical processes, high-temperature materials drying, etc.). Also, the high-temperature heat can be converted into mechanical energy through solar-driven heat engines. This mechanical energy (as in the form of shaft turning) can be used for water pumping or direct driving of processes. Also, the mechanical energy can be converted into electrical energy through appropriate DC or AC electric generators.

Another path is to convert the high-temperature heat from concentrated solar radiation to chemical energy. This is a convenient form to store the solar energy. In this approach, chemical fuels are synthesized. Envisaged fuels are hydrogen (discussed in detail in Chapter 13), various Fischer–Tropsch fuels (formed from carbon dioxide/monoxide and hydrogen), alcohols, and ammonia. The primary materials for manufacturing synthetic fuels are taken from water (hydrogen), air (nitrogen), fossil fuels (carbon, hydrogen), and biomass (carbon, hydrogen).

The direct radiation can be used for driving photo-biochemical processes through special engineered devices and systems that mimic photosynthesis (so-called artificial photosynthesis, see Chapter 13) or other processes involving micro-organisms stimulated by light. Such processes lead to production of hydrogen, methane, some sugars, and alcohols, which can be further used as fuels. Of course, biochemical conversion of solar radiation also occurs naturally in living systems like green plants, or indirectly in animals that consume plants but use solar radiation for heating.

9.2.1 Thermodynamic Limits of Solar Energy Conversion

On average, the direct solar radiation illuminating the earth's surface, which consists of a flux of photons covering a spectrum of energies from infrared to ultraviolet, delivers 1.6 to 2.8 MWh annually for each square meter of the earth's surface. At the outer shell of the terrestrial atmosphere, the intensity of solar radiation, called the solar constant (see also Chapter 2), is taken on average as $I_{SC} = 1{,}353$ to 1,367 W/m^2, with a fluctuation of about 7% annually. Through photothermal solar radiation conversion, there is a process of conversion of solar radiation (which carries photonic energy) into high-temperature heat followed by conversion of the heat into mechanical energy (or shaft work). Because the mechanical energy may be converted into electrical energy, photothermal solar radiation conversion can be viewed as a means to generate either mechanical or electrical power. Photovoltaic solar radiation conversion results in the direct production of electric energy from solar energy

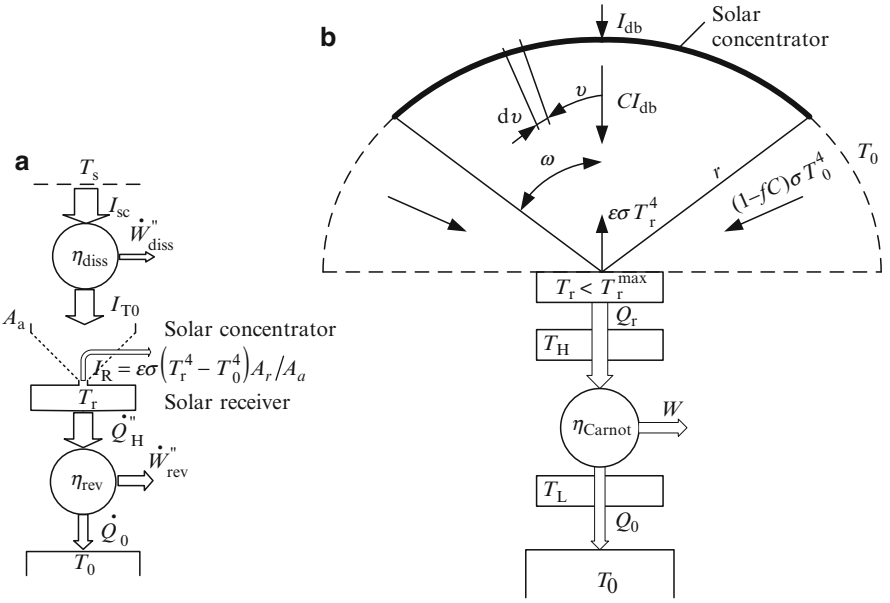

Fig. 9.3 Thermodynamic models for photothermal solar radiation conversion into work. (**a**) Model for exergy of insolation; (**b**) model accounting for solar concentration and heat transfer

using the photoelectric effect. It is important to have a theoretical model for converting solar radiation into work (electricity) and for determining the efficiency of this process.

9.2.1.1 Efficiency of Photothermal Solar Radiation Conversion into Work

A theoretical model for photothermal solar energy conversion can include a solar concentrator that generates heat from concentrated solar radiation and drives a Carnot heat engine operating between a high-temperature reservoir and the ambient temperature T_0. One can also consider in the model the existence of a temperature difference at the sink and the source owing to heat transfer. Thermodynamic modeling of the photothermal solar energy conversion is demonstrated in Fig. 9.3.

The model represented in Fig. 9.3a demonstrates the process of solar radiation conversion into work, which is affected by three factors: the sun, the terrestrial atmosphere, and the environment that exists at the terrestrial surface where the heat engine is located. The engineered system that generates work is simply made from a solar collector coupled to a heat engine directly. We assume first that there is no thermal resistance at the sink and source of the heat engine; this assumption will be relaxed thereafter. Between the sun and the collector is the terrestrial atmosphere. The atmosphere is responsible for ad hoc dissipation of the incident photonic radiation work and heat through various mechanisms such as scattering, absorption,

heating, evaporation, moving of air masses, and so on. The atmospheric dissipation can be modeled like a heat engine working between the outer shell of the atmosphere and the collector surface and operating as a "brake" with efficiency η_{diss}. The working fluid of such a heat engine is the so-called photonic gas, which is a representation of the photonic radiation. It is shown by many researchers, for example Bejan (2006), that such "equivalent" heat engine modeling makes sense thermodynamically, since photonic radiation can be viewed as thermal radiation, with both having the same electromagnetic nature and wave/particle behavior. If one denotes T_{S} as the temperature of the sun and T_{r} as the temperature of the solar receiver (see Fig. 9.3), then the efficiency of the "atmospheric brake" is

$$\eta_{\text{diss}} = \frac{\dot{W}''_{\text{diss}}}{I_{\text{SC}}} = \frac{I_{\text{SC}} - I_{\text{T0}}}{I_{\text{SC}}} = \varphi\left(1 - \frac{T_{\text{r}}}{T_{\text{S}}}\right), \quad \varphi \leq 1. \tag{9.1}$$

In the above equation, the parameter $\varphi \leq 1$ accounts for the Carnot abatement of the dissipater (its efficiency must be smaller or at most equal to that of a Carnot heat engine operating between the same temperatures). I_{SC} denotes the solar constant, which is the intensity of solar radiation on W/m^2 of terrestrial surface; $I_{\text{T0}} \leq I_{\text{SC}}$ represents the intensity of solar radiation incident on the solar collector; $\dot{W}''_{\text{diss}}$ is the atmospheric dissipation rate per unit of terrestrial surface. The solar collector has two components: a solar concentrator that reduces the area of the hot spot (using lenses or mirrors) from a large aperture area A_{a} to a small receiver area A_{r}. The receiver is, due to heating, at a higher temperature than that of ambient ($T_{\text{r}} > T_0$) and thus it loses heat through radiation accounting for (see the figure) $I_{\text{R}} = \varepsilon\sigma\left(T_{\text{r}}^4 - T_0^4\right)A_{\text{r}}/A_{\text{a}}$. The heat losses can be minimized by making $A_{\text{a}} \gg A_{\text{r}}$ and $\varepsilon \to 0$, where ε represents the emissivity factor of the solar receiver and $\sigma = 5.67 \times 10^{-8}\,\text{W/m}^2\,\text{K}^4$ is the Stefan–Boltzmann constant. Ideally, heat losses through radiation could be reduced to zero (even though this is not physically achievable in practice); in this case, the energy balance on the receiver reads $\dot{Q}''_{\text{H}} = I_{\text{T0}}$, which means that all the concentrated solar radiation that falls on the receiver is transformed into heat and delivered to the heat engine at the temperature T_{r}. The generated work by the reversible heat engine operating between T_{r} and T_0 represents the mechanical energy obtained through photothermal solar radiation conversion, and it is in these conditions that $\dot{W}''_{\text{rev}} = I_{\text{T0}}(1 - T_0/T_{\text{r}})$. The receiver temperature can be obtained by solving Eq. (9.1) for T_{r}, and one obtains

$$\dot{W}''_{\text{rev}} = I_{\text{T0}}\left[1 - \frac{T_0}{T_{\text{S}}} \times \frac{\varphi I_{\text{SC}}}{I_{\text{T0}} - (1-\varphi)I_{\text{SC}}}\right]. \tag{9.2}$$

The aim of this theoretical development is to find the maximum work generation from photothermal solar radiation conversion; therefore, one asks what is the maximum value of the $\dot{W}''_{\text{rev}}$. The answer can be found by considering what happens if the atmosphere is completely clear and the dissipation tends to zero. In this case $\varphi \to 1$ and the collector captures an incident radiation of the order of the solar

constant $I_{T0} \cong I_{SC}$. Since in this situation the work generated from solar radiation reaches the maximum possible (upper bound), Zamfirescu and Dincer (2008a) proposed the following equation:

$$\dot{E}x'' = I_{T0}\left(1 - \frac{T_0}{T_S} \times \frac{I_{SC}}{I_{T0}}\right), \quad I_{T0} \cong I_{SC} \tag{9.3}$$

to be adopted as the exergy content of the incident solar radiation (insolation). It can be observed that in the condition where $I_{T0} = I_{SC}$, the exergy of solar radiation becomes

$$\dot{E}x'' = I_{T0}\left(1 - \frac{T_0}{T_S}\right), \tag{9.4}$$

which was derived by many authors in various approaches (see Bejan 2006).

One may now find more realistic estimates of the amount of work that can be generated through photothermal conversion of solar radiation by accounting for some irreversibilities. After determining this amount of work, one can estimate the energy and exergy efficiencies of the conversion process. The model presented in Fig. 9.3b accounts for the optical process of concentration of the incident solar radiation, for radiation losses and for temperature drops at the source and sink of a heat engine driven by solar heat at high temperature T_r and connected with the environment at $T_0 \ll T_r$. The solar concentrator, which can be a mirror or a system of lenses, is shown abstractly in the figure as a hemisphere extending over a solid angle $\Omega_S < 2\pi$ above the solar receiver. Recall that according to definition a solid angle is the ratio between the area of a sphere segment and the square of the radius, measured in steradians (sr); therefore, the solid angle of a hemisphere is 2π. If the concentrator is used, the small hot spot of the solar receiver sees the sun on a larger solid angle $\Omega_C > \Omega_S$ without the concentrator (denoted in this case with Ω_S). The ratio between the two solid angles (with and without concentration) defines the concentration ratio $C = \Omega_C/\Omega_S \geq 1$. From the geometry shown in Fig. 9.3b, we can see that $\Omega_C = \pi \sin^2\omega$. If one denotes R_S as the radius of the solar disk and R_0 as the radius of a sphere centered on the earth and touching the sun, then the solid angle under which the receivers see the sun without a concentrator becomes $\Omega_s = \pi(R_s/R_0)^2$. Thus the concentration ratio is

$$C = \left(\frac{R_0}{R_S}\sin\omega\right)^2. \tag{9.5}$$

Note that the maximum concentration is obtained when the planar angle ω becomes $\pi/2$, that is when the receiver sees the sun under the whole hemisphere. In this case, the concentration ratio becomes $C_{max} = (R_0/R_S)^2 \cong 46{,}300$; if this situation occurs, then the solar receiver may be in thermodynamic equilibrium with the solar disk, that is $T_r = T_S$.

The radiation impacting the solar concentrator (the direct beam radiation, I_{db}) is smaller than the solar constant; thus one can simply write $I_{db} = \zeta I_{SC}, \zeta \leq 1$. This radiation is concentrated, thus

$$I_{r,db} = C\zeta I_{SC}, \tag{9.6}$$

where $I_{r,db} = CI_{db}$ is the concentrated solar radiation falling on the receiver. The aperture factor under which the receiver sees the environment that is the rest of the hemisphere (see Zamfirescu et al. 2009) is $1 - \sin^2\omega$; therefore, the environment at temperature T_0 emits radiation incident on the receiver according to

$$I_{r,0} = \left(1 - \sin^2\omega\right)\sigma T_0 = \left(1 - \tilde{C}\right)\sigma T_0, \tag{9.7}$$

where $\tilde{C} = C/C_{max}$ and one observes from Eq. (9.5) that $\sin^2\omega = \tilde{C}$.

The receiver itself should be a gray body with emissivity ε that emits radiation over the whole hemisphere according to

$$I_{r,e} = \varepsilon\sigma T_r^4. \tag{9.8}$$

The energy balance on the receiver, accounting for the incoming and outgoing energy rate, states that $\alpha\left(I_{r,db} + I_{r,0}\right) = I_{r,e} + Q_r$, where α is the receiver's absorptivity (namely what percent of the incoming radiation is absorbed) and Q_r is the heat delivered by the receiver to the heat engine (see Fig. 9.3b). Denoting the ratio $\chi = \varepsilon/\alpha$ as the "selective gray body factor," one obtains, using Eqs. (9.6) to (9.8), the following expression for the generated heat:

$$Q_r = \alpha\left[(\zeta C)I_{SC}C_{max} + \left(1 - \tilde{C}\right)\sigma T_0^4 - \sigma\left(\chi T_r^4\right)\right]. \tag{9.9}$$

The heat engine receives the heat flux Q_r at a lower temperature $T_H < T_r$ and discharges a heat fluid Q_L into the ambient air at $T_L > T_0$ to generate the mechanical work $W = Q_r - Q_L$. Assuming linear heat transfer irreversibilities at the sink and the source, $Q_r = U_H(T_r - T_H)$ and $Q_L = U_L(T_L - T_0)$, one can obtain the following expression:

$$\frac{W}{\left(\zeta\tilde{C}\right)I_{SC}\alpha C_{max}} = \left(1 + \frac{1 - \tilde{C}}{\zeta\tilde{C}}\theta_0^4 - \frac{\chi}{\zeta\tilde{C}}\theta_r^4\right)$$

$$\left\{1 - \theta_0\left[\theta_r - \theta_U\left(\zeta\tilde{C}\right)\alpha\left(1 + \frac{1 - \tilde{C}}{\zeta\tilde{C}}\theta_0^4 - \frac{\chi}{\zeta\tilde{C}}\theta_r^4\right)\right]^{-1}\right\}. \tag{9.10}$$

From the above expression, the following dimensionless temperatures are used:

$$\left.\begin{aligned} \theta_0 &= \frac{T_0}{T_S} \\ \theta_r &= \frac{T_r}{T_S} \\ \theta_U &= \frac{\sigma T_S^3}{U}; \quad \text{where} \quad U = \frac{(U_H U_L)}{(U_H + U_L)} \end{aligned}\right\}. \tag{9.11}$$

Note that the ratio W/C, which represents the amount of work generated by the photothermal energy converter per unit of square meter of the earth's surface illuminated by the solar radiation, can be maximized, according to Eq. (9.10), if (1) the maximum concentration is achieved ($\tilde{C} \to 1$); (2) the emitted radiation by the receiver is negligible with respect to the absorbed radiation ($\chi \to 0$); (3) the receiver absorbs all radiation ($\alpha \to 1$); and (4) the receiver is in thermodynamic equilibrium with the sun ($\theta_r \to 1$). In these conditions, the work generated per unit of surface (W/C) according to Eq. (9.10) coincides with that given above in Eq. (9.4).

The energy and exergy efficiencies based on the produced work (W/C) and the concentrated radiation incident on the receiver $C\zeta I_{sc}$ are defined by

$$\left.\begin{aligned} \eta &= \frac{W/C}{\zeta I_{SC}} \\ \psi &= \frac{W/C}{\zeta I_{SC}(1 - T_0/T_S)} \end{aligned}\right\}. \tag{9.12}$$

Using Eq. (9.10), the energy and exergy efficiencies become

$$\left.\begin{aligned} \eta &= \alpha\left(1 + \frac{1-\tilde{C}}{\zeta\tilde{C}}\theta_0^4 - \frac{\chi}{\zeta\tilde{C}}\theta_r^4\right)\left(1 - \frac{\theta_0}{\theta_r - Q_r/(UT_S)}\right) \\ \psi &= \alpha\left(1 + \frac{1-\tilde{C}}{\zeta\tilde{C}}\theta_0^4 - \frac{\chi}{\zeta\tilde{C}}\theta_r^4\right)\left(1 - \frac{\theta_0}{\theta_r - Q_r/(UT_S)}\right)/(1 - \theta_0) \end{aligned}\right\}. \tag{9.13}$$

Note that these conversion efficiencies are functions of the following parameters:

- Climatologic parameters such as average environment temperature (θ_0) and direct beam radiation intensity (ζ)
- Optical parameters of the solar collector such as concentration ratio (C), hemispherical absorptivity of the solar receiver (α), ratio of hemispherical emissivity, and absorptivity of solar receiver (χ)
- Heat engine parameters such as the geometric mean of heat transfer resistance at the sink and the source (U)

Some theoretical idealizations can be applied to the efficiency equations (9.13). For example, one can assume that the receiver is a black body ($\alpha = 1, \chi = 1$), the sky is perfectly clean and does not dissipate solar radiation at all ($\zeta = 1$), and there

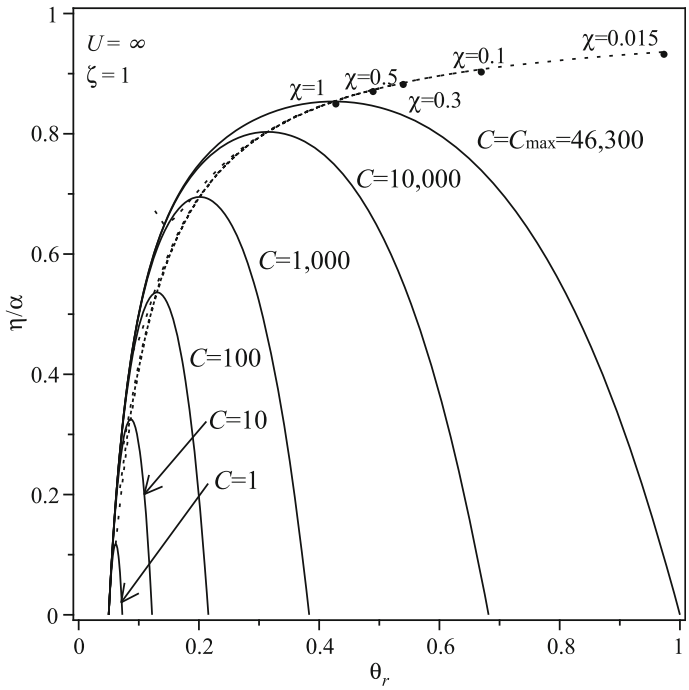

Fig. 9.4 Photothermal solar energy conversion efficiency for $\theta_0 = 0.05$ [modified from Zamfirescu et al. (2009)]

is no heat transfer resistance at the sink and source of the reversible heat engine ($U = \infty$). In these conditions, the energy efficiency becomes

$$\eta = \left[1 + \left(\frac{1}{\tilde{C}} - 1\right)\theta_0^4 - \frac{1}{\tilde{C}}\theta_r^4\right]\left(1 - \frac{\theta_0}{\theta_r}\right). \tag{9.14}$$

If in Eq. (9.14) one assumes maximum concentration of solar radiation ($\tilde{C} = 1$), then one can determine at which θ_r one obtains the maximum efficiency. Assuming $T_0 = 288$ K, that is, $\theta_0 = 0.05$ one obtains a known result, namely $\eta_{max} = 0.853$ for $\theta_r = 0.42$ or $T_r = 2{,}443$ K. This is a known result revised, for example, in Bejan (2006), and it represents the upper limit of the efficiency of a solar-driven reversible heat engine operating with maximum concentration under a clear sky, with no heat losses and no temperature differences due to heat transfer at the sink and the source. Better efficiency can be obtained if the receiver is more selective ($\chi < 1$). The maximum efficiency in such case can be calculated from Eq. (9.13): $\eta_{max} = 0.91$ for $\chi = 0.1$ or $\eta_{max} = 0.93$ for $\chi = 0.015$. More results based on Eq. (9.13) are seen in Fig. 9.4. It can be observed that the efficiency always has a maximum at a certain receiver temperature (given dimensionless as θ_r).

The maximum energy and exergy efficiency (divided by absorptivity of the receiver α) are indicated in Fig. 9.5 assuming infinite heat transfer conductance at

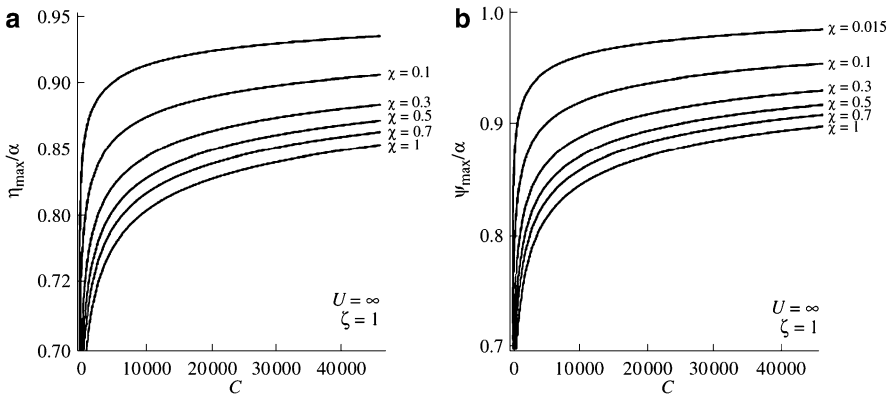

Fig. 9.5 Maximum energy (**a**) and exergy (**b**) efficiency for $\theta_0 = 0.05$, assuming infinite heat transfer conductance at the source and the sink [modified from Zamfirescu et al. (2009)]

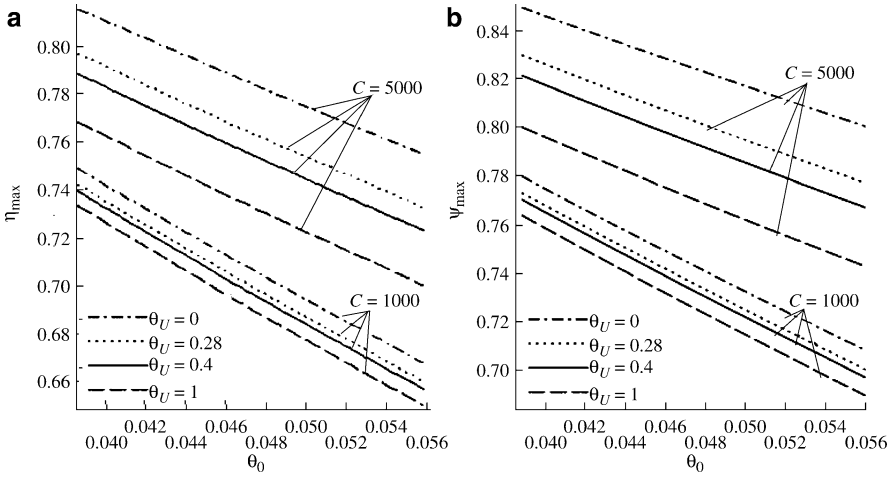

Fig. 9.6 Maximum energy (**a**) and exergy (**b**) efficiency of photothermal solar energy conversion as a function of ambient temperature, for various heat transfer conductances and concentration ratios [modified from Zamfirescu et al. (2009)]

the source and sink sides of the reversible heat engine. Figure 9.6 indicates the influence of heat transfer conductances involved in Eq. (9.13). The heat transfer conductances are given in the form of θ_U according to Eq. (9.11).

9.2.1.2 Efficiency of Photoelectric Energy Conversion of Solar Radiation into Work

Photoelectric energy conversion involves dislocation of electric charges in a substance caused by the energy of photons. When a photon is absorbed by a semiconductor, it promotes an electron in a high energy state and thus generates one electron–hole

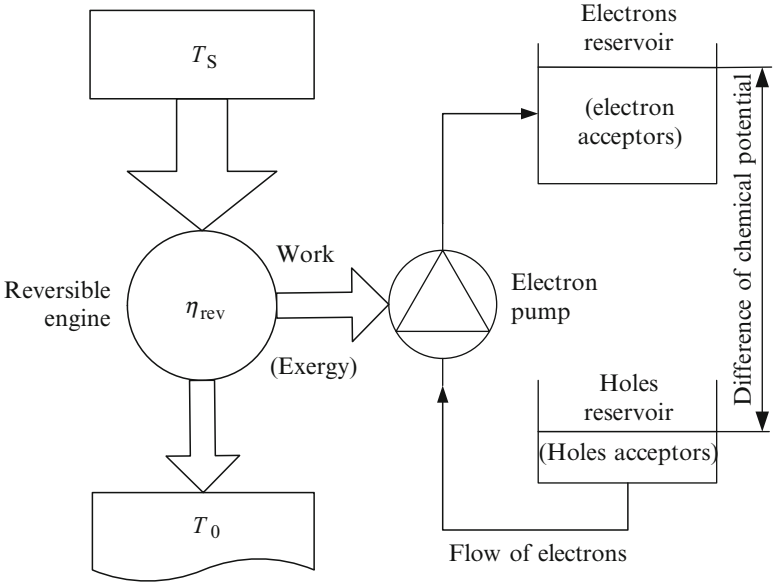

Fig. 9.7 Thermodynamic model for photoelectric solar energy conversion

pair that generates a voltage across the semiconductor junction. The same basic process happens at the molecular level where photons dislocate electrons, which causes transfer of charge between two molecules (one called the donor and the other the acceptor). The photoelectric conversion process can be modeled as in Fig. 9.7.

In the above model, there is an engine operating between two thermal reservoirs. This engine is similar to a heat engine. It operates with solar radiation, which in fact contains thermal radiation. The engine is in contact with the radiation of the sun at temperature T_S and rejects radiation in the ambient air (sensed in the form of heat) at temperature T_0. The work generated by this engine, assumed reversible, is given by the Carnot factor $1 - T_0/T_S$ as a proportion of the energy input; this work is used to drive an electron pump that takes electrons from a reservoir (hole reservoir) at low chemical potential and discharges them in a reservoir of high chemical potential. Other devices (not shown), external to this system, may take electrons from the high potential reservoir and discharge them at the low potential reservoir. When the two processes—moving electrons up and down—run at the same rate, then the overall system operates at steady state.

According to Markvart and Landsberg (2002) the electrochemical potential difference is given by the following equations:

$$\left.\begin{aligned} \Delta\mu &= e\Delta\Upsilon, \text{ in photovoltaic cells} \\ \Delta\mu &= kT\ln\left(\frac{pq}{p_0q_0}\right), \text{ in photochemical reactions} \\ \Delta\mu &= e\Delta\Upsilon + k_BT\ln\left(\frac{pq}{p_0q_0}\right), \text{ in photosynthesis} \end{aligned}\right\}, \tag{9.15}$$

where $e = 1.602 \times 10^{-19}$ C is the elementary electric charge, $\Delta\Upsilon$ is the light-induced electrostatic potential difference, p is the probability that an electron occupies the excited state, q is the probability that a hole occupies the donor state, and the index 0 indicates the probability of recombination of electrons and holes. Note that for all three conversion devices considered in Eq. (9.15)—photovoltaic cells, photochemical reactions, and photosynthesis systems—the processes require "dislocated" electrons; therefore, all these processes are photo/electric driven and the model shown in Fig. 9.7 is valid for all. By definition, the electrochemical potential combines the potential energy stored in chemical form and the electrostatic field. Thus electrochemical potential is the sum of the chemical and electric potentials, that is, $\mu_{ec} = \mu_{ch} + \mu_{el}$, where $\mu_{el} = nF\Delta V = e(nN_A\Delta V) = e\Delta\Upsilon$, where n is the number of electron transfer per mol of reaction product, $F = eN_A$ is the constant of Faraday, N_A is the Avogadro number, ΔV is the local electrostatic potential, and $\Delta\Upsilon$ is the electrostatic potential associated with 1 mol of reaction product. Thus in Eq. (9.15) the variation of potential is electrostatic by its nature for the photovoltaic case, is chemical for the photochemical case, and is electrochemical for the photosynthesis case. Thus the most general form of potential involved in photo/electric radiation conversion is "electrochemical potential."

The energy transmitted to a process in the form of work can be quantified by Gibbs energy variation, which at an infinitesimal scale is $dG = \sum d(\mu_i n_i) - s\,dT + v\,dP$, where μ_i is the chemical potential of specie "i" whose number of mols is n_i. In photonic driven processes (photovoltaic, photochemical, photosynthesis) the processes evolve at constant pressure and temperature, thus $dG = \sum d(\mu_i n_i)$. If a reaction occurs (stimulated by light), then the Gibbs energy of the reaction will be $\Delta G = \sum \Delta(\mu_i n_i) = \Delta\mu_{el}$. The Gibbs free energy of the reaction affects the reaction equilibrium whose equilibrium constant is $K_{eq} = \exp(-\Delta G/RT) = \exp(-\Delta\mu_{el}/RT)$, where R is the universal gas constant and T is the process temperature. Further, the equilibrium constant is related to the reaction rate of the forward (k_f) and backward (k_b) reactions through the following equation: $k_f = k_b K_{eq} = k_b \exp(-\Delta\mu_{el}/RT)$; thus the reaction rate is a function of electrochemical potential variation (induced by the photonic energy), $k_f = k_f(\Delta\mu_{el})$. Moreover, the reaction product generation rate is proportional with the reaction rate $\dot{n}_{prod} = \text{const} \cdot k_f$, where $\dot{n}_{prod}$ is given in mol per second; thus $\dot{n}_{prod} = \dot{n}_{prod}(\Delta\mu_{el})$.

The energy rate developed/consumed by the reaction is given by $\dot{W} = \dot{n}_{prod} \times \Delta\mu$. This energy is supplied to the system from the exterior (in our case it originates from photonic energy). Figure 9.8 illustrates qualitatively the typical dependence of the reaction rate with electrochemical potential. Note that the variation indicated in the figure is typical of any electrochemical-driven reaction, regardless of the driving energy sources from photons or an electric generator or something else. In essence, this diagram says that if the reaction rate (and implicitly the rate of production or the current) increases, the electrochemical potential must decrease. When the electrochemical potential is nil, the rate of reaction is at a maximum, as is denoted on the figure with $k_{f,sc}$; the index "f,sc" is borrowed from photovoltaics where it has the meaning "short circuit" (i.e., the current is at a maximum but the difference in chemical potential is nil).

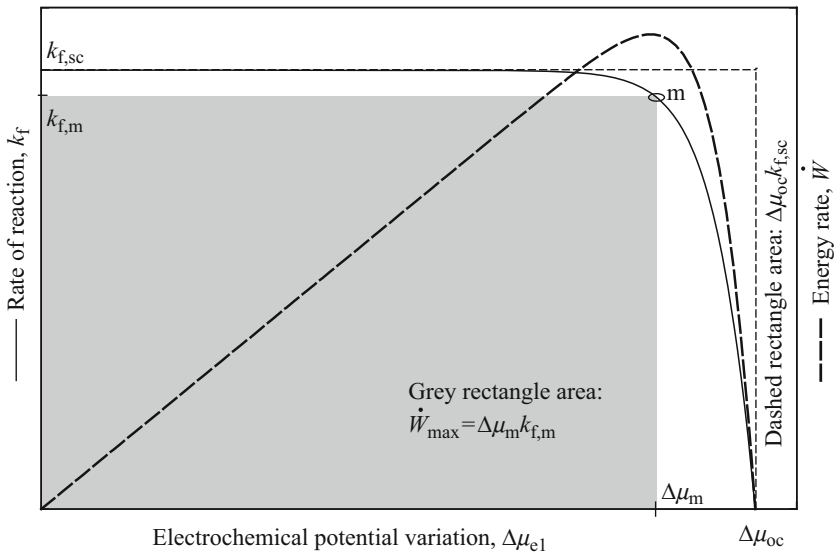

Fig. 9.8 Rate of reaction and reaction energy rate variation of electrochemical potential

This is a consequence of the limitation of the power supplied to the reaction ($\dot{W}$ is quasi-constant and bounded). In contrast, if the reaction rate decreases, necessarily the electrochemical potential increases. At the limit, when the reaction rate is nil (there is no current and no chemical production) the maximum potential is obtained, as indicated on the figure with $\Delta\mu_{oc}$ (the index "oc" is borrowed this time from "open circuit" used in photovoltaics). Figure 9.8 also shows qualitatively (with dashed line) the energy rate calculated as the product $\dot{W} = \dot{n}_{prod} \times \Delta\mu$. This curve has a maximum at $\Delta\mu_m$ with the $\dot{W}_{max} = \Delta\mu_m \times k_{f,m} \times$ const.

Observe here the analogy between the qualitative results for the photo/electric solar energy conversion indicated in Fig. 9.8 and the results for photothermal solar energy conversion shown in Fig. 9.4. Both show a maximum of the developed work. The analogue variables are the temperature and electrochemical potential on the abscissa, and the heat flux and the reaction rate (equivalent with molar production rate or current) on the ordinate. Quantitative calculation and plots will be shown later in this section regarding the photovoltaic power conversion. The analytical treatment is general (that is valid for photovoltaics, photochemical and photosynthesis) and the aim to determine the maximum efficiency of the process.

In Fig. 9.8, the maximum work generated by the conversion process is given by the area of the gray rectangle. The area of the dashed rectangle is $\Delta\mu_{oc} \times k_{f,sc}$, and it is similar to an energy rate that never can be developed by the process. It is useful to define the ratio of the "filling factor" as the ratio of the areas of the gray rectangle over the dashed rectangle.

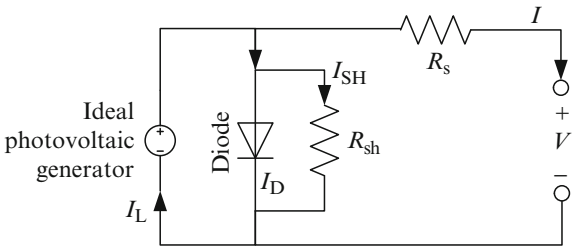

Fig. 9.9 Equivalent electrical circuit of a PV cell

The magnitude of the filling factor is useful in determining the maximum energy rate generation from the open circuit potential and the short circuit reaction rate, which are determinable quantities. The maximum energy rate generation becomes

$$\dot{W}_{\max} = \text{const} \cdot \Delta\mu_{\text{m}} \times k_{\text{f,m}} = \text{const} \cdot \text{FF} \times \Delta\mu_{\text{oc}} \times k_{\text{f,sc}}. \tag{9.16}$$

Therefore, the energy and exergy efficiency of photo/electric solar energy conversion are

$$\left.\begin{aligned} \eta &= \frac{\text{const} \cdot \text{FF} \times \Delta\mu_{\text{oc}} \times k_{\text{f,sc}}}{I_{\text{SC}} \times A} \\ \psi &= \frac{\text{const} \cdot \text{FF} \times \Delta\mu_{\text{oc}} \times k_{\text{f,sc}}}{I_{\text{SC}}(1 - T_0/T_{\text{S}}) \times A} \end{aligned}\right\}, \tag{9.17}$$

where A is the area exposed to solar radiation and $I_{\text{SC}}(1 - T_0/T_{\text{S}})$ represents the reversible work per unit of area (the exergy) that drives the process according to the model illustrated in Fig. 9.7. It is instructive to apply the general equation [Eq. (9.17)] for the case of photovoltaic systems. Their particular form in this case becomes

$$\left.\begin{aligned} \eta &= \frac{\text{FF} \times V_{\text{oc}} \times I_{\text{sc}}}{I_{\text{rated}} \times A} \\ \psi &= \frac{\text{FF} \times V_{\text{oc}} \times I_{\text{sc}}}{I_{\text{rated}}(1 - T_0/T_{\text{S}}) \times A} \end{aligned}\right\}, \tag{9.18}$$

where I_{rated} represents the solar irradiance under ratio conditions; typically for PV cells $I_{\text{rated}} = 1{,}000\ \text{W/m}^2$.

Three factors must be determined in order to calculate Eq. (9.18): the filling factor, the open circuit voltage, and the short circuit current. For this reason, one has to develop the current–voltage diagram of the PV (photovoltaic cell). The equivalent electric circuit of a PV cell is presented in Fig. 9.9. It consists of a source of photovoltaic current in parallel with a diode and a shunt resistor (R_{sh}). In series with the external load is the internal resistor (R_{s}). The photovoltaic current I_{L} splits into three currents such that $I_{\text{L}} = I + I_{\text{D}} + I_{\text{sh}}$.

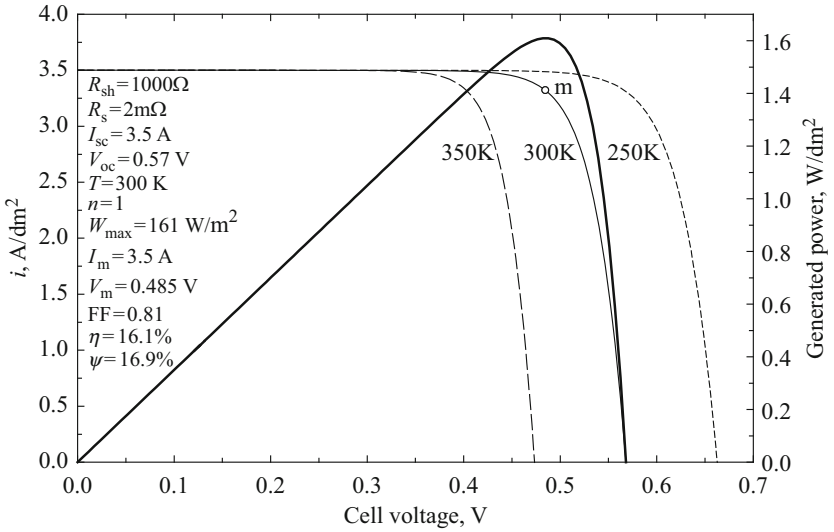

Fig. 9.10 Current density vs. voltage and power density vs. voltage of a typical PV cell

The Shockley equation gives the current through the diode as a function of the voltage and the temperature; using the Shockley equation one obtains

$$I = I_L - I_0\left\{\exp\left[\frac{e(V+IR_s)}{nk_BT}\right]-1\right\} - \frac{V+IR_s}{R_{SH}}, \tag{9.19}$$

where I_0 is the reverse saturation current of the diode, e is the elementary electrical charge, n is the diode ideality factor (unity for the ideal diode), k_B is the Boltzmann constant, and T is the temperature.

When operating in an open circuit, the voltage on the load becomes $V = V_{oc} = I_0R_{sh}$, where the residual current depends on the temperature according to $I_0 = [k_BT/(eR_s)]\ln(I_L/I_0 - 1)$. When it operates in a short circuit, the voltage on the cell vanishes, thus $I_{sc} \cong I_L$.

Figure 9.10 reports the calculated results for a typical PV cell showing the current density and the power density in correlation with the cell voltage. The filling factor is 81%. The cell is rated under a solar irradiance of 1,000 W/m^2. In these conditions, the cell efficiencies are 16.1% (energy based) and 16.9% (exergy based) for standard temperature. Typical PV cells reach 10% to 15% energy efficiency; the advanced ones can reach 25% while some recently developed cells achieve 40%.

9.2.1.3 Solar Exergy Maps

The efficiency of the solar radiation conversion and the power generated per square meter of collector surface depend on the intensity of the solar radiation and the local temperature. These parameters vary with geographical location, the time of day,

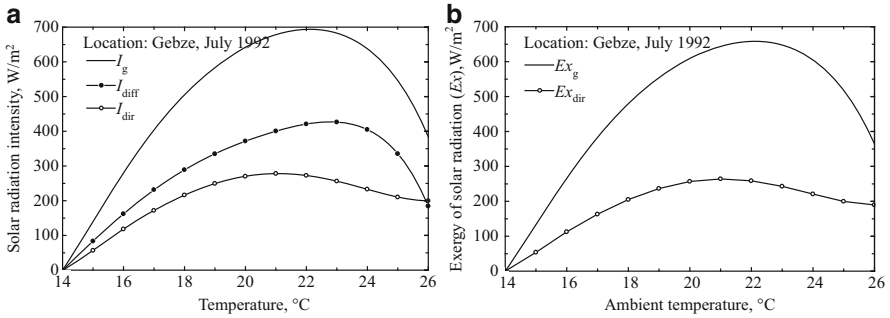

Fig. 9.11 Solar radiation intensity and exergy at Gebze, Turkey, correlated with ambient temperature [data from Dincer et al. (1996a)]

and the season. Information about the direct beam radiation and diffuse radiation is required for many reasons including design of solar collectors, design of buildings, design of heating, ventilation and air conditioning systems, snow melt calculations in hilly areas, climate prediction, and so on. Thus, both diffuse and global radiations are recorded at many meteorological stations and other institutions around the globe and are centralized in databases. Here through global radiation one notes the sum of direct beam radiation (coming directly from sun) and diffuse radiation (reflected on the surface by other bodies, including the clouds). Thus, $I_g = I_{dir} + I_{diff}$, where indices g, dir, and diff stand for global, direct, and diffuse radiation, all expressed in watts per square meter of the earth's surface.

It is important to determine the thermodynamic limits of solar radiation conversion at geographic locations and for each season such that the opportunity of installing solar power generation capacities can be judged on a rational basis. Thus exergy of solar radiation can be calculated for each geographic location. Moreover, it has been observed that the intensity of solar radiation can be correlated with local temperature variation. For example, Dincer et al. (1996a) show polynomial correlations between local temperature and global and diffuse radiation in Gebze, Turkey (approx. 40°N, 29°E). Using these correlations, one can predict the exergy content of solar radiation in Gebze, as shown in Fig. 9.11. For the case presented, which corresponds to the average values recorded for July 1992, one can observe that the diffuse radiation was quite high.

The exergy of the solar radiation, meaning the maximum expected work that can be generated by converting solar energy in July 1992 in Gebze, calculated with Eq. (9.4), was around 650 W/m^2. If only direct beam radiation is used for conversion, then the corresponding exergy is around 300 W/m^2 at maximum. If the solar concentrator would be tracing the sun, assuming a tilt angle of 45°, the maximum expected exergy becomes $\sqrt{2} \times 300 \cong 425$ W/m^2, or around 900 W/m^2 is the global radiation is used in exergy calculation.

Solar exergy maps were developed by Joshi et al. (2009a) including several geographic locations in the United States and India. The direct beam radiation intensity on a tilted surface (tracking the sun) was used for calculation of the exergy

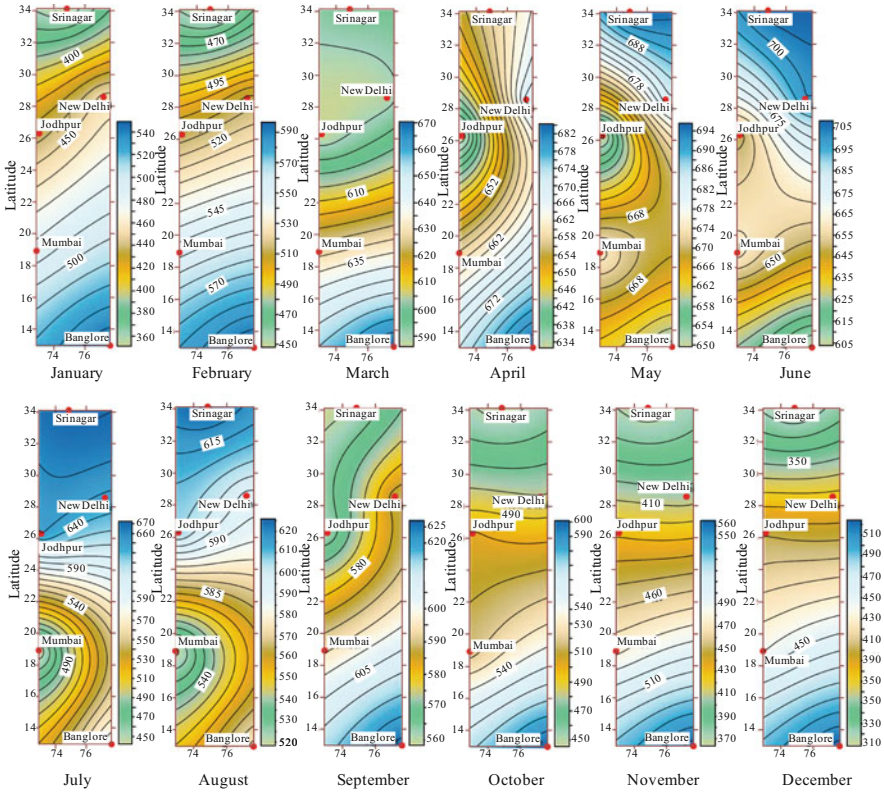

Fig. 9.12 Solar exergy maps for Indian cities (horizontal axis: the longitude) [modified from Joshi et al. (2009a)]

according to Eq. (9.4); diffusion radiation was not considered in the development of the solar exergy maps. Figure 9.12 shows the solar exergy maps for India as developed by Joshi et al. (2009a).

The solar energy conversion is more complete when cogeneration of electricity (work) and heat is applied. This can be done with various systems. For example, if a solar-driven heat engine is used, the heat ejected by the heat engine can be recovered at a temperature level that makes convenient the use of the associated thermal energy for some purpose. If a photovoltaic panel is employed to generate electricity from solar radiation, special arrangements can be designed to recover also some of the heat that is generated (on the panel surface) by the incident solar radiation.

One can define an exergy efficiency of power and heat cogeneration from solar radiation. The efficiency must be reported with respect to the exergy of the incident radiation. The corresponding formula is given as follows:

$$\psi = \frac{\dot{W} + \dot{E}x_{\text{th}}}{\dot{E}x}, \tag{9.20}$$

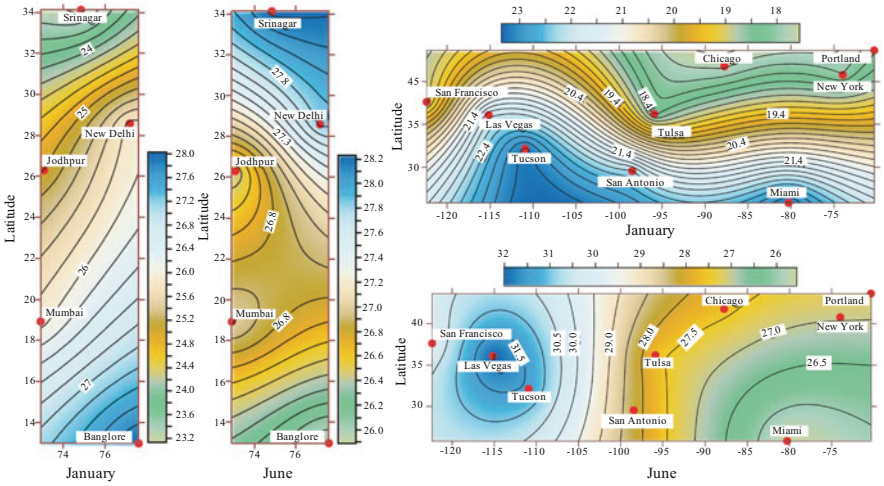

Fig. 9.13 Exergy efficiency maps for power and heat cogeneration developed for India and the U.S. (horizontal axis: the longitude) [modified from Joshi et al. (2009a)]

where $\dot{E}x$ is the exergy of the insolation (incident solar radiation), $\dot{W}$ is the generated power, and $\dot{E}x_{\text{th}}$ is the exergy associated with the generated thermal energy. The exergy of the solar radiation can be calculated as indicated by Eq. (9.4). The generated power depends on the efficiency of the conversion system. As shown above, the thermodynamic limit of photothermal solar energy conversion efficiency is ~84% for black body receivers and goes toward 90% for selective gray body receivers. If photo/electric conversion is applied, then the generated power depends on the filling factor of the specific process; with photovoltaics $\dot{W} = \text{FF} \times V_{\text{oc}} \times I_{\text{sc}}$.

Normally, the expected efficiency of photovoltaics is 10% to 15% as mentioned above. The exergy of the generated thermal energy also depends on the process. If one assumes that the solar energy converter heats a heat transfer fluid and increases its exergy from $\dot{E}x_{\text{in}}$ at inlet to $\dot{E}x_{\text{out}}$ at outlet, then the thermal exergy generated by the system would be $\dot{E}x_{th} = \dot{E}x_{\text{out}} - \dot{E}x_{\text{in}}$. In the case that the temperature of the heat transfer fluid does not change very much during the energy transfer process, then the thermal exergy can be calculated with $\dot{E}x_{\text{th}} = \dot{Q} \times (1 - T_0/\bar{T}_{\text{th}})$, where $\bar{T}_{\text{th}}$ is the average temperature at which the generated heat is made available, $\dot{Q} = \dot{H}_{\text{out}} - \dot{H}_{\text{in}}$ is the generated heat flux, and $\dot{H}$ is the enthalpy rate of the heat transfer fluid.

Solar exergy efficiency maps were developed by Joshi et al. (2009a) for India and the U.S. assuming the typical efficiency of a photovoltaic–thermal system (to be introduced later) that cogenerates power and heat. These maps are shown in Fig. 9.13. The heat generated is at a low-temperature level (under 100°C) and the corresponding exergy efficiencies calculated with Eq. (9.20) are in the range of 20% to 30%. Maps indicating solar exergy and exergy efficiency of the solar radiation conversion are useful for installing and designing solar energy systems because they indicate in a concise way the thermodynamic limits of solar energy conversion

for each geographic location and season. For example, the maps above show that Tucson is a better place than Portland for solar energy harvesting since one expects about 5% more conversion efficiency.

9.2.2 Solar Thermal Energy

As stated above, the thermodynamic limits of solar radiation conversion are important and must be known when any solar energy project is started. These limits are upper bound estimates. When the actual application is determined, various kinds of irreversibilities can be accounted for in the analysis, and accurate estimation of the conversion efficiency of each system can be obtained. We will analyze here and in the subsequent section various types of solar energy conversion systems. First, we focus in those systems that generate thermal energy from solar radiation; next the systems that generate electricity will be discussed; other systems (cogeneration, hydrogen generation) also will be briefly analyzed.

In principle, two kinds of systems exist for conversion of solar radiation into heat: nonconcentrating and concentrating solar radiation system. The systems that do not concentrate solar radiation operate at lower temperature (typically below 100°C) and are used in general for water heating or space heating or drying (see Fig. 9.2). They are mainly based on solar panel and solar pond designs. The solar concentrator uses optics (mirrors and lenses) to generate high-temperature heat on small area spots.

9.2.2.1 Passive Solar Heating

Solar passive heating is a technique of using solar thermal energy through designs that use few or no mechanical systems (i.e., no pumps, or fans, or evacuated tube collectors, or other advanced technologies). Passive solar energy mainly involves special arrangements of building facades and windows. Solar passive technology also may include solar stills (which are simple arrangements that produce water distillation through the greenhouse effect) or solar ponds, which will be introduced in the subsequent paragraphs.

Simple arrangements like south-facing widows allow a good transmittance of photonic energy inside the building; the light is then reflected and partially absorbed by the walls and eventually it reaches windows from the inside where it is partially reflected back and partly refracted toward the outside. Thus there is a positive accumulation of solar energy inside the building, during the daytime. The construction materials, such as internal walls, the building shell, and so on, store the thermal energy accumulated during the day and enable a temporal phase shift between solar radiation availability and heat utilization. The windows' glassing shows high transmittance for short waves (2–3 μm) and is relatively opaque to long infrared waves that are emitted by the building elements; thus, infrared radiation has a good chance to dissipate inside the building, and this is a form of passive solar heat.

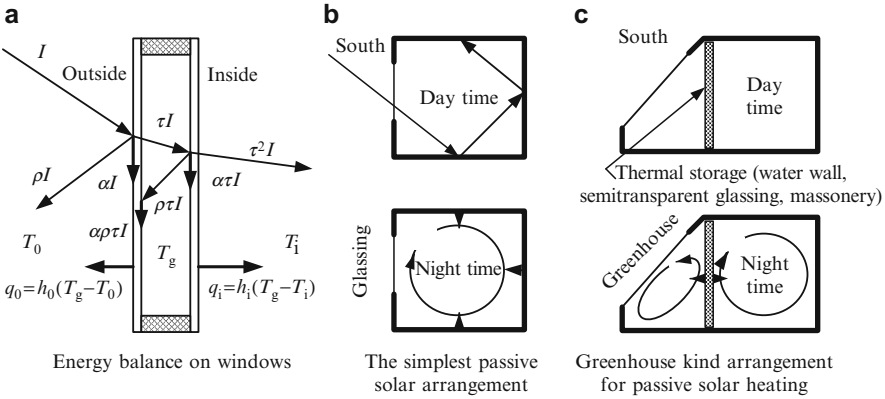

Fig. 9.14 Solar passive heating arrangements

The energy balance in double windows is suggested schematically in Fig. 9.14(a). Basically, the incident irradiation I (in W/m^2) is reflected by the exterior glassing outside (ρI, where ρ is the reflectivity), partly absorbed (αI), and partly transmitted (τI). The transmitted rays fall on the inner glassing where they are again reflected ($\rho\alpha I$) toward the outer glassing, partly absorbed in the glassing ($\alpha\tau I$), and partly transmitted toward the inside ($\tau^2 I$). The two types of glassing are heated by the absorbed radiation—the outer glassing with $\alpha(1+\rho\tau)I$ and the inner with $\alpha\tau I$—and thus they are at a higher temperature than both the outside air and the inside air. Therefore, heat transfer occurs between the glassing and the inner and outer spaces.

Assuming an average glassing temperature T_g, then the heat transfer toward the outside, per unit of glassing area, is $q_0 = h_0(T_g - T_0)$, and toward the inside is $q_i = h_i(T_g - T_i)$. Note that the absorption coefficient in single glassing can be up to 30%, allowing thus for rather high temperatures on their surface. The transmittance for perpendicular incidence can reach 90% for simple glassing, and 65% to 80% for two-pane glassing. The energy balance on the double glassing can be solved for the average temperature of the panes; it is $T_g = T_0 + T_i + 12/\bar{h}(\alpha I + \alpha\rho\tau I + \alpha\tau I)$, where $\bar{h}$ is the average heat transfer coefficient $\bar{h} = 0.5\,(h_0 + h_i)$.

Figure 9.14b,c suggests some possible passive solar heating arrangements that use no mechanical means and no solar collectors. The simplest arrangement is that of a south-facing window. During the daytime, solar rays heat the room and also the masonry back wall, floor, and ceiling, which accumulate heat during the day. In the nighttime, the air from the room is heated by the walls, which are at a slightly higher temperature. Natural heat convection currents are formed in the room during the night as indicated in the figure. One advanced design is shown in Fig. 9.14c, which uses a greenhouse and thermal storage. The greenhouse has a southward glassing with a tilted surface to capture more solar radiation. In between the room and the greenhouse a thermal storage device in the form of a wall is placed. This can be a masonry wall, or a water wall (that is, a water reservoir shaped as a wall), or semitransparent glassing materials with good thermal storage behavior. During the

daytime, the greenhouse temperature increases and the accumulated heat is stored in the wall. During the nighttime, the accumulated heat is discharged in both directions, toward the room and toward the greenhouse, with a preference for the room direction because of slightly larger temperature gradients.

9.2.2.2 Solar Ponds and Other Solar Thermal Storage Systems

The use of thermal energy storage is essential for solar thermal systems because in this way one can compensate for the solar energy intermittence and fluctuation in intensity. Several classes of storage may be required for a single installation depending on the scale, kind, and application (see Dincer and Dost 1996). For example, heating and hot water applications can use thermal storage in water itself, phase change materials, soil, rock, and other solids.

A variety of solids are also used; rock particles of 20 to 50 mm in size are most prevalent. Well-designed packed rock beds have several desirable characteristics for energy storage. The heat transfer coefficient between the air and the solid is high, the cost of the storage material is low, the conductivity of the bed is low when air flow is not present, and a large heat transfer area can be achieved at low cost by reducing the size of the particles. Chapter 11 reviews thermal storage system in detail. The particularity of solar thermal energy consists in its high range of temperature levels. Thermal storage at very high temperature is required by many thermal applications including heat-to-power conversion or synthetic fuel production. Thermal storage in oil–rock systems (in which the energy is stored in a mixture of oil and rock in a tank) for hot water and heat-recovery applications are examples of medium-temperature applications, while those in molten nitrate salt systems use high temperatures.

Solar ponds are passive solar systems that do these two functions in one single device. The principle of the solar pond is to create, with the help of solar heating, a salinity concentration gradient in a pool of salt water. Figure 9.15 introduces the operating principle of the solar pond. Basically, the solar pond is a pool of salt water placed in a position such that it is well illuminated by the solar radiation. Mostly, the solar radiation comes from the southerly direction during the day if the device is located in the Northern Hemisphere (note that the representation in the figure reflects the situation from the Northern Hemisphere; if placed in the Southern Hemisphere, the solar rays will come mostly from the north). The solar pond has three working zones (or layers). At the upper level is placed the convective zone of thickness X_1, as indicated in the figure. It follows the nonconvective zone until the depth X_2, and at the bottom of the pool is the heat storage zone.

Figure 9.15 shows details for each operating layer of the solar pond. The upper convective zone is fed with fresh water of a density close to the density of fresh water in the upper part to maintain the cleanliness of the pond and replenish lost water due to superficial evaporation process. As suggested in the figure, a part of the solar radiation incident on the surface is lost by reflection, while some other part

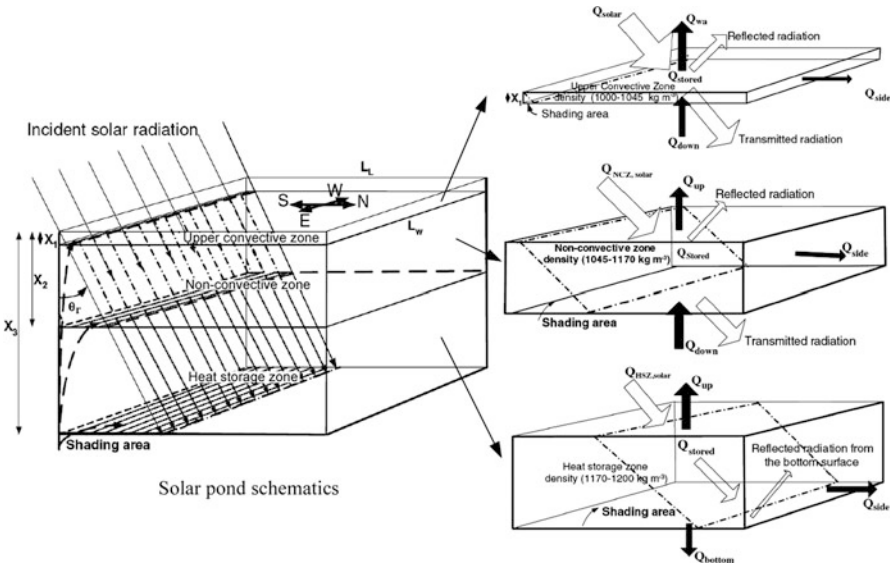

Fig. 9.15 Illustration of the operating principle of a solar pond with details of the three specific working zones [modified from Karakilcik et al. (2006)]

(Q_{wa}) is transmitted to the surrounding air through heat convection and water evaporation. The remaining, major part of the incident solar radiation is transmitted to the nonconvective layer.

This nonconvective layer plays the role of thermal insulation. It is composed of salty water layers whose brine density gradually increases up to about 1,170 kg/m^3. This layer allows an extensive amount of solar radiation to penetrate into the storage zone while inhibiting the propagation of long-wave solar radiation from escaping because water is opaque to infrared radiation.

The third layer is the heat storage zone with relatively uniform density, at the highest value within the pond. A considerable part of the solar energy is absorbed and stored in this region. This layer has the highest temperature; hence, the strongest thermal interactions occur between this zone and the adjacent insulated bottom-wall and insulated side-walls.

The relative thickness of each of the zones of a solar pond is about 7% for the convective layer, 40% for the insulating layer, and 53% for the heat storage layer. The heat stored in the lower layer can be recovered by a pumping system that continuously draws brine at a higher temperature and returns it at a lower temperature. The average temperature gradient between the upper and lower layers of the pond varies from about 8° to 10°C in the colder months to 25° to 30°C in the hotter months. The bottom layer can reach 50° to 80°C during the summer. Figure 9.16 shows the calculated results for the conversion efficiencies of a typical solar pond and their variation from the winter to the summer season. Each zone of the pond has an associated energy efficiency, as indicated in the following Eq. (9.21) by the subscripts

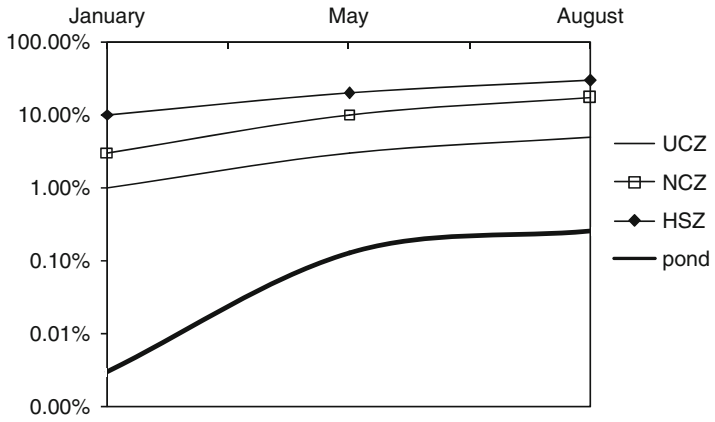

Fig. 9.16 Characteristic conversion efficiencies of a solar pond and its subsystems [data from Karakilcik et al. (2006)]

UCZ, NCZ, HSZ representing the upper convective zone, the nonconvective zone, and the heat storage zone, respectively:

$$\left.\begin{aligned} \eta_{\mathrm{UCZ}} &= \frac{Q_{\mathrm{NCZ}}}{Q_{\mathrm{solar}}} \\ \eta_{\mathrm{NCZ}} &= \frac{Q_{\mathrm{HSZ}}}{Q_{\mathrm{NCZ}}} \\ \eta_{\mathrm{HSZ}} &= \frac{Q_{\mathrm{stored}}}{Q_{\mathrm{HSZ}}} \\ \eta_{\mathrm{pond}} = \eta_{\mathrm{UCZ}}\eta_{\mathrm{NCZ}}\eta_{\mathrm{HSZ}} &= \frac{Q_{\mathrm{stored}}}{Q_{\mathrm{solar}}} \end{aligned}\right\}, \tag{9.21}$$

where η_{pond} is the overall energy efficiency of the solar pond.

The energy efficiency of the pond is very low, a fact that makes solar ponds economically justifiable only when the investment cost is low. Mostly, the efficiency of the pond is degraded by the losses in the upper convective layer.

9.2.2.3 Solar Thermal Collectors

Here we discuss all types of solar collectors used to convert solar energy into heat from a low temperature to a very high temperature. The usual thermal collectors employed for water heating do not concentrate the solar radiation. The types that concentrate the solar radiation are used mostly for electricity generation through heat engines. However, recent trends are to use concentrated solar radiation for process heating. A classification of solar thermal collectors is shown in Fig. 9.17.

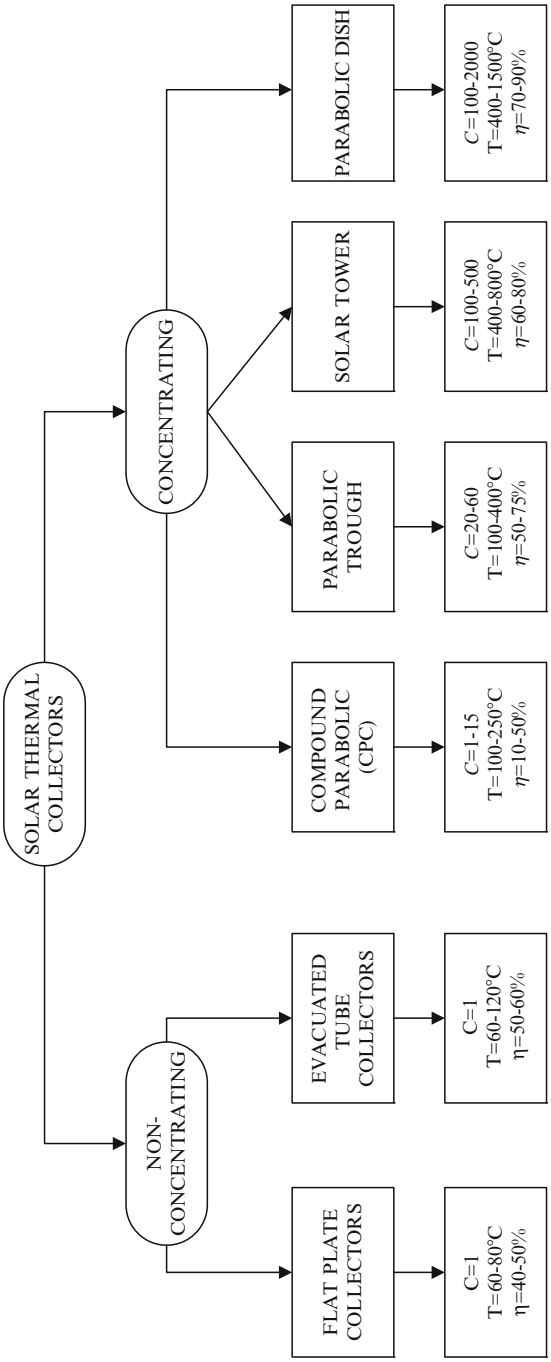

Fig. 9.17 Solar thermal collectors

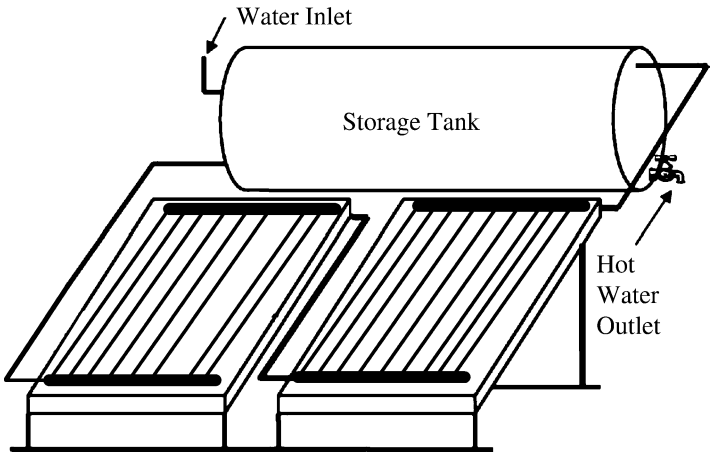

Fig. 9.18 Water heater system with flat plate solar collectors

Flat plate collectors are simply made from a number of tubes assembled in a flat box with glassing and a black back-plate. Water is circulated through the tubes that are exposed to incident solar radiation as indicated in Fig. 9.18. Flat-type solar collectors have good efficiency when used for water heating at temperatures higher than the ambient temperature up to 25°C. If the temperature is higher, the collector efficiency decreases due to heat losses through heat transfer by convection to the environment. For higher temperature applications, the use of evacuated tube collectors becomes more efficient than simple glass collectors. Evacuated tube collectors use vacuum to reduce heat losses by convection. They consist of a tube-in-tube assembly, where the outer tube is of transparent glass and is a vacuum. The inner tube is circulated by a heat transfer fluid or a two-phase working fluid having the role of transmitting the solar thermal energy. In the two-phase fluid case, the system works like a heat pipe.

Operation at higher temperature necessitates concentration of the solar radiation. Compound parabolic collectors are so-called nonimaging collectors that are able to concentrate solar radiation up to 15 times. The term *nonimaging* refers to the type of optics; that is, the concentrator does not form an image of the sun on the solar receiver. The compound parabolic collectors do not necessitate solar tracking, because their geometry is such that the solar rays are reflected on a hot spot regardless of the sun's position. For temperatures higher than about 200°C, the nonimaging concentrator shows major heat losses, and thus the preferred concentrators are of the imaging type. The imaging concentrators use optical systems to create an image of the sun on a small hot spot (the solar receiver). Imaging concentrators can concentrate the radiation on a line or on a spherical point. The imaging concentrators must track the sun in order to be able to focus the sun on the receiver. Parabolic collectors are those that concentrate the solar radiation along a line.

A solar tower consists of a field of mirrors, called heliostats, that track the sun and concentrate the radiation on a receiver placed on a tower. The receiver normally is of the line type made on an assembly of tubes. Other geometry variations are

Table 9.1 Characteristics of some solar collectors

Collector	Acurex 3001	M.A.N. M480	Luz LS-1	Luz LS-2	Luz LS-2	Luz LS-3
Year	1981	1984	1984	1985	1988	1989
Area (m^2)	34	80	128	235	235	545
Aperture (m)	1.8	2.4	2.5	5	5	5.7
Length (m)	20	38	50	48	48	99
Receiver diameter (mm)	51	58	42	7	7	7
Concentration ratio	36:1	41:1	61:1	71:1	71:1	82:1
Optical efficiency	0.77	0.77	0.734	0.737	0.764	0.8
Receiver absorptivity	0.96	0.96	0.94	0.94	0.99	0.96
Mirror reflectivity	0.93	0.93	0.94	0.94	0.94	0.94
Receiver emittance	0.27	0.17	0.3	0.24	0.19	0.19
Operating temperature (°C)	295	307	307	349	390	390

Data from Zamfirescu et al. (2008)

possible for the receiver of the solar tower; one can say that the concentration type in the case of the solar tower is somewhere in between line-type concentration and point-type concentration. The highest temperatures are obtained with solar dishes that use paraboloidal mirrors to focus the solar radiation on a point. Actually, the focal point has an elliptic shape.

The main characteristics and the performance of some parabolic systems constructed and tested in the 1980s are listed in Table 9.1. Regarding point concentrators, there have been a number of small-scale designs tried in the last decades, as summarized by Zamfirescu et al. (2008). The Omnium-G concentrator has a 6-m-diameter paneled dish that provides 7 to 12 kW of thermal power under 1,000 W/m^2 insolation. The "test bed" concentrator had an 11-m paneled dish and provided 76 kW thermal power. The Lajet concentrator comprises 24 1.5-m-diameter dishes and delivers 33 kW of thermal power. The Advanco concentrator provides 74 kW thermal power using a 10.6-m-diameter paneled dish. General Electric's Parabolic Dish Concentrator 1 used a 12-m paneled dish to provide 72.5 kW of heat. Power Kinetics had a 9-m square-shaped paneled concentrator that delivered 28 kW to a boiler under 0.88 to 0.94 kW/m^2 insolation. The Acurex Parabolic Dish Concentrator 2 used an 11-m paneled dish providing 800 W of concentrated solar heat per square meter of aperture. Boeing created a solar point concentrator equipped with 0.6 × 0.7 m mirror panels with an optical efficiency of up to 0.8, which provides a concentration ratio of 3,000. The ENTCH Fresnel Concentrator Lens used panels of 0.67 × 1.2 m and could only provide an optical efficiency of 0.68 at a concentration ratio of 1,500. Currently, the largest single-dish power system is Australia's Big Dish with an aperture of 20 m, which produces 200 kW of thermal power feeding a 500°C boiler.

Apart from the dish concentrator (of paraboloidal surface), another established system for solar thermal power generation is the Fresnel mirror formed from an assembly of plain or curved surface mirrors suspended from a frame structure. The individual mirrors point toward a single focal point where the solar receiver is placed. For tracing the sun, the whole assembly rotates around the azimuth and zenith angles. A similar option is represented by Fresnel lenses that use the light refraction phenomenon to focus the incident radiation.

Although line and point concentrators have been around, there is a cost and technological gap that needs to be closed in order to exploit their high efficiencies. The performance factors of a dish system can be greatly degraded with changes in geometry, and therefore accuracy and rigidity are important for their design. The optical efficiency of the solar concentrator, concentration ratio, and the intercept factor, which will be defined rigorously in the subsequent paragraphs, are important factors defining the system performance. Some cost estimations were compiled in Zamfirescu et al. (2008). On average, for an optical efficiency of 0.90 to 0.93, a concentration ratio of 2,000 to 5,000, an intercept factor of 0.98, and a lifetime of 30 years, a low-cost price estimate is \$200 to \$350 per m^2. Another cost estimate is based on the Acurex concentrator having an optical efficiency of 0.86 and a concentration ratio of 1,900 costing \$330 per m^2 for a production scale of 100,000 units/year.

Back-silvered glass is the standard design for the mirrors having 94% reflectivity. The reflector can be a single layer, which is more efficient and more expensive, or it can be broken into components, which is cheaper but less efficient. Another option is the stretched membrane mirror of which manufacture involves a vacuum process. Singular element stretched membrane mirrors have demonstrated optical efficiencies of 0.915, which is lower than that of the best glass-metal mirrors, but at a lower cost.

Two methods of tracking the sun are used with line and point concentrators. In the first method, sensors provide optical feedback of the sun's position to allow for variable tracking. In the second method, the system is preprogrammed to follow the sun based on the local longitude, latitude, and time. Line focus concentrators in general track the sun in one direction, namely along the polar axis. The second axis alignment is adjusted daily or weekly. The azimuth tacking is applied to point-focus concentrators because it allows for constant two-axis tacking.

In the design of the concentrating solar collector there is a trade-off between optics and heat losses. The solar collector efficiency represents the ratio between the heat absorbed by the solar receiver $\dot{Q}_\mathrm{r}$ and the incident solar radiation I_{T0}, normal on the collector's aperture of area A_a. Thus the thermal efficiency of the solar collector is $\eta_{\mathrm{coll}} = \dot{Q}_\mathrm{r}/(I_{\mathrm{T0}}A_\mathrm{a})$. The solar collector can be divided into two subsystems. The first is the optical subsystem, having the role to concentrate the solar radiation on the small spot receiver. The efficiency of the optical subsystem, called optical efficiency, can be defined as the intensity of the concentrated light over the intensity of the incident light. Because of optical losses due to reflectivity, transmissivity, optical error, and shading, $I_\mathrm{r}A_\mathrm{r} < I_{\mathrm{T0}}A_a$; thus the ratio between the two is the optical efficiency $\eta_{\mathrm{opt}} = (I_\mathrm{r}A_\mathrm{r})/(I_{\mathrm{T0}}A_a)$. The second subsystem is the thermal one, which converts the incident concentrated light radiation into heat. Several thermal radiation and heat convection losses are characteristic of this subsystem. The efficiency of this subsystem is known as thermal efficiency. The receiver's absorbance, emittance, and heat transfer coefficient by convection affect mostly the thermal efficiency, which is defined as the ratio of the absorbed heat and the concentrated solar radiation $(I_\mathrm{r}A_\mathrm{r})$, written as $\eta_{\mathrm{th}} = \dot{Q}_\mathrm{r}/(I_\mathrm{r}A_\mathrm{r})$. Thus, one can say

that the solar collector efficiency is given by $\eta_{\text{coll}} = \eta_{\text{opt}} \times \eta_{\text{th}}$. The energy balance on the solar receiver reads

$$I_{\text{r}} A_{\text{r}} = \dot{Q}_{\text{r}} + U A_{\text{r}} (T_{\text{r}} - T_0), \tag{9.22}$$

where U is the linearized heat loss coefficient of the receiver, assumed at the temperature T_{r}, higher than that of the environment T_0. If one divides Eq. (9.22) with $(I_{\text{T0}} A_a)$, the collector efficiency is obtained as follows (note that $C = A_{\text{a}}/A_{\text{r}}$ is the concentration ratio):

$$\eta_{\text{coll}} = \eta_{\text{opt}} \times \left[1 - \frac{U(T_{\text{r}} - T_0)}{C I_{\text{T0}} \eta_{\text{opt}}} \right], \tag{9.23}$$

which identifies that

$$\eta_{\text{th}} = 1 - \frac{U(T_{\text{r}} - T_0)}{C I_{\text{T0}} \eta_{\text{opt}}}. \tag{9.24}$$

Equations (9.22) to (9.24) are general and apply to all types of solar collectors classified in Fig. 9.17. We will detail next the optics point concentrator, as it is very instructive. For a point concentrator, the optical efficiency is large when most of the concentrated radiation is captured by the solar receiver surface placed in the vicinity of the focal point, that is, when the hot spot exposed to the radiation has a large area. However, a large hot spot area means large heat losses through radiation or possibly through convection.

The optics of a paraboloidal dish solar concentrator including the definition of the main parameters like the rim angle, aperture, parabola equation, and the focal distance is described in Fig. 9.19a, which illustrates the profile of a paraboloidal mirror targeting the sun. The image of the solar disk is incident on every point of the mirror surface under an angle of about 32 min (~0.54°) and is specularly reflected toward the focal point under the same angle. In the focal plane, the solar disk image will be deformed, depending on the location of any particular point on the mirror. The points from the rim circle produce mostly deformed images; this maximum deformation is indicated with D_{FP} in the figure. The minimal deformation corresponds to the central point of the mirror (note that this point is generally shaded). The mirror's reflectivity, shading, glazing transmissivity, absorptivity, and other parameters affect the quality of the optical image formed in the focal plane. The relevant parameters for optical modeling of the solar dish are defined in Table 9.2. Based on the definition of the optical efficiency (above) and the definitions presented in Table 9.2,

$$\eta_{\text{opt}} = \zeta \rho \gamma \tau \alpha. \tag{9.25}$$

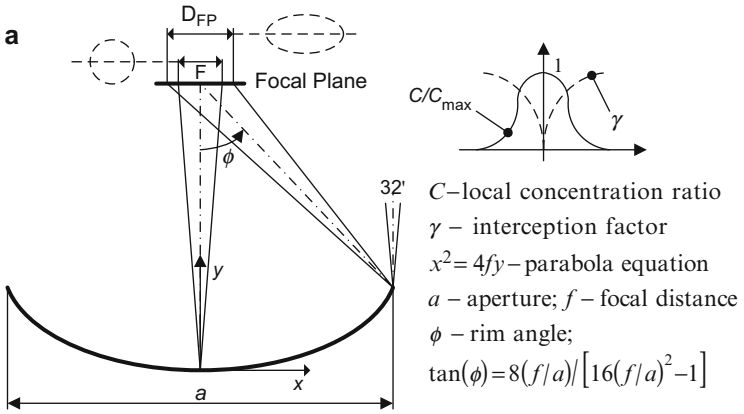

Optical parameters of solar concentrator

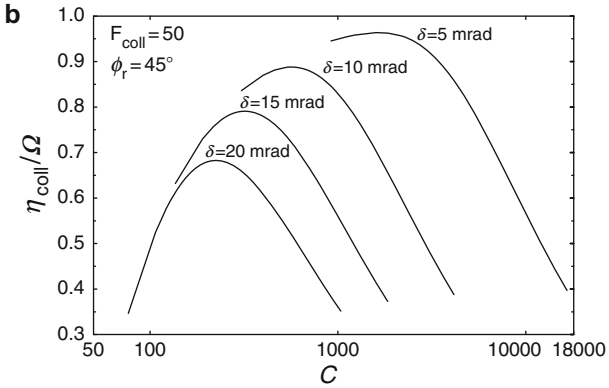

Point focus collector efficiency

Fig. 9.19 Optical model and efficiency of a point-focus solar collector with a rim angle $\phi_r = 45°$, as a function of the concentration ratio and optical errors δ [modified from Zamfirescu et al. (2008)]

For design calculation, the values of shading, reflectivity, transmissivity, and absorptivity are assumed to be average values. The statistical dispersion of their values, however, is taken into account through several kinds of optical errors. Thus, we will express the optical efficiency by two factors. The first factor is the optical factor introduced here as follows:

$$\Omega = \zeta \rho \tau \alpha. \tag{9.26}$$

The optical factor is calculated with averaged values for the reflectivity, transmissivity, and absorptivity, and it has values in the range of 0.75 to 0.85 depending

Table 9.2 Relevant optical parameters characterizing the optics of a solar dish concentrator

Name	Definition	Remarks
Shading factor	$\zeta = \frac{A_u}{A_a}$	It represents the ratio between unshaded mirror area and aperture area.
Reflectivity	$\rho = \frac{I_\rho}{I_{T0}}$	The reflected solar radiation intensity over the incident radiation intensity. Reflectivity accounts for imperfect specular reflection.
Intercept factor	$\gamma = \frac{\int_0^{A_{ab}} I \, dA}{I_\rho A_u}$	Not all concentrated radiation falls on the absorber surface. There is a practice to reduce the absorber surface in order to minimize the heat transfer. Thus, one accepts that some concentrated radiation is lost. The intercept factor represents the ratio between the radiation power falling on the absorber and the power associated to the radiation reflected toward the focal point.
Transmissivity	$\tau = \frac{I_\tau A_{ab}}{\gamma I_\rho A_u}$	In the case when the absorber is covered by glazing (a practice intended to reduce the heat loss via convection), a part of the incident (concentrated) radiation is lost due to transmission through glazing. The transmissivity represents the ratio between transmitted power through glazing and the radiation power incident on glazing.
Absorptivity	$a = \frac{I_c}{I_\tau}$	It represents the ratio between the absorbed heat flux and the power associated with the radiation incident on the absorber.

on the quality of the optics. The second factor is the intercept γ, which accounts also for statistical dispersion of the reflectivity and other optical errors (see Table 9.2). Note that

$$\eta_{opt} = \Omega\gamma. \tag{9.27}$$

Figure 9.19a also presents (qualitatively) the variation of the intercept factor in the focal plane, in the vicinity of the focal point (see the upper right corner). The intercept factor is nil in the focal point because no surface area can be associated with one single point; therefore, no radiation is "intercepted." The parameter x in the plot $\gamma(x)$ is the radial coordinate originating in the focal point. In measure with increasing x, the amount of intercepted light increases over a disk centered at the focal point; thus, the intercept factor increases and eventually reaches the unity value. The derivative of the $\gamma(x)$ represents the local concentration ratio that obviously has a maximum right at the focal point. The geometric concentration ratio is related to the optical system geometry, optical errors, and the intercept factor through the fact that γ is a function of A_r.

There are several kinds of optical errors that affect the quality of the solar image projected on the receiver's surface. All of the optical errors cited in the following discussion represent statistical means relative to the entire area of the solar concentrator. A first, unavoidable error is caused by the nonuniform angular distribution of solar radiation beam, δ_{sun}. Even though this is a small contribution to the overall optical error, it cannot be neglected; it has a typical value of one fourth of the solar angle, namely 2.3 mrad. Other errors are the slope error of the concentrator δ_{slope}

(typically 2–3 mrad), the specularity δ_ω (typically 0.5–1 mrad), and the pointing error δ_p, meaning the receiver is not placed exactly at the focal point. These individual angular errors produce an overall optical error accounted for by $\delta^2 = \delta_{sun}^2 + \delta_{slope}^2 + \delta_\omega^2 + \delta_p^2$.

Using the above derivations, it can be shown that the collector efficiency can be analytically expressed as $\eta_{coll}\Omega = \gamma(1 - F_{coll}/C\gamma)$, where $F_{coll} = U(T_r - T_0)/(I_{T0}\zeta\rho\tau\alpha)$ is a collector factor depending on the solar absorber temperature (assumed at the average), the insolation, and optical properties. Figure 9.19b illustrates the variation of collector efficiency (expressed as $\eta_{coll}\Omega$) with the concentration ratio for several optical errors δ. It is clearly observed that the efficiency increases with the quality of the surface (smaller δ), which occurs each time there is an optimal concentration ratio for which the collector efficiency is maximum. The existence of this maximum can be explained intuitively:

- If the concentration ratio is too low, then the concentrated radiation is low, and the heat absorbed by the receiver is low.
- If the concentration ratio is too high, then the receiver temperature and thus the heat losses to the ambient air are higher; thus, the heat absorbed by the receiver is also low.

In general, the optical factor is high (0.8–0.95), which indicates that the point-focus solar concentrators can reach an efficiency over 70%.

9.2.2.4 Solar Thermal Applications

The applications of solar thermal energy are classified in Fig. 9.2 into three categories, namely, heating, production of mechanical energy, and conversion to chemical energy. Many processes require heat as input. Some examples are suggested in Fig. 9.2 (water heating, space heating, cooking, drying, etc.) but the list is long (e.g., it may include solar refrigeration, various industrial processes, and many others). An important application is conversion of thermal energy into work using heat engines. This application is discussed largely in Section 9.2.3.2 regarding the conversion of solar energy into chemical energy; hydrogen production appears to be very important for the sustainable development. Various paths to produce hydrogen from solar thermal energy are analyzed in Chapter 13.

Illustrative Example: Drying Food Products with Solar Thermal Energy

In this example, the efficiency of a solar dryer for food products comprising an air heater driven by solar energy and a drying chamber is analyzed. The example is taken from Tiris et al. (1995). Drying is a method of preservation of food products. The system is presented schematically in Fig. 9.20. The air is taken from outside and circulated by a blower over a valve and electrical heater, a flowmeter, followed by a solar air heater and a drying chamber. The flow rate and pressure drop over the air heater are measured with appropriate instruments. The drying chamber includes a rack with food products among which warmed air is circulated.

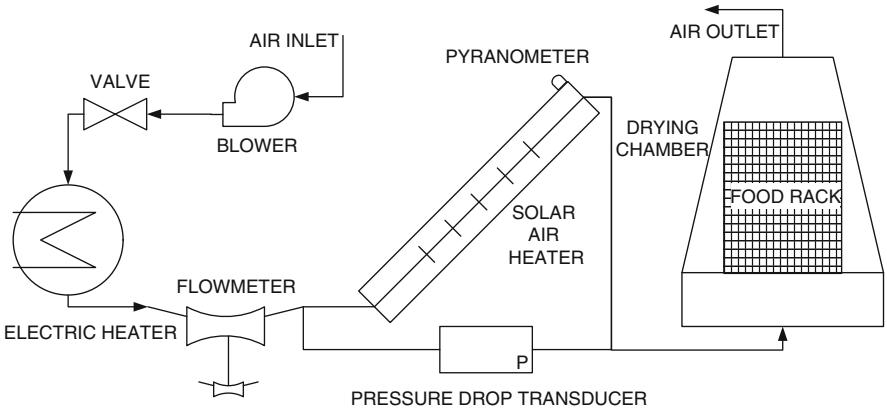

Fig. 9.20 Solar food drying system [modified from Tiris et al. (1995)]

The air dryer is a parallel-piped–shaped box that includes helical-type aluminum wires painted in black and functioning as an absorbent surface for solar radiation and an extended surface to enhance the heat transfer to the air. During the experiments, the air-solar collector has been tilted at 30° pointing in a southerly direction. The collector glassing has been made from polyester combined with transparent glass wool, conferring elasticity, durability, acoustic dumping, and high transmittance. The valve in the diagram has the role of air flow regulation, while the electric resistance was used to pretest the solar drying process and to preselect the air entrance temperature in the solar heater. A star-type pyranometer has been used to measure the solar radiation on the tilt surface. The wind speed and the air humidity were also recorded. Several kinds of foods were dried in this system in a series of experiments by Tiris et al. (1995). The moisture contents and weight changes of the test samples were determined based on measurements.

The efficiency of the solar air heater was calculated with $\eta_{\mathrm{SAH}} = \left(\dot{m}c_{\mathrm{p}}\right)_{\mathrm{air}}(T_{\mathrm{out}} - T_{\mathrm{in}})/I_{\mathrm{T0}}$. The process efficiency is based on absolute air humidity determinations in the drying chamber. Namely, the efficiency of the process is calculated by $\eta_{\mathrm{dry}} = (x_{\mathrm{out}} - x_{\mathrm{in}})/(x'' - x_{\mathrm{in}})$, where x'' is the saturation humidity of the air at inlet; note that because the air takes humidity from the products, it is always the case that $x_{\mathrm{out}} > x_{\mathrm{in}}$.

The results indicate that the collector efficiency η_{SAH} was around 40% to 80% while the drying process efficiency varied in time during the process depending on the type of food product. Initially, the process efficiency is higher, and while the process evolves the efficiency diminishes. For a mass velocity of the air of 0.055 kg/m^{2}s, the results were correlated according to Fig. 9.21. The beans show the best efficiency, which at the beginning of the process is about 90% and decreases to around 35% after 35 hours of drying. The efficiency varies by process, starting in the range 20% to 90%, the lowest value being for chili peppers. At the end of the process, the efficiencies are in the range of 7% to 30%. The average

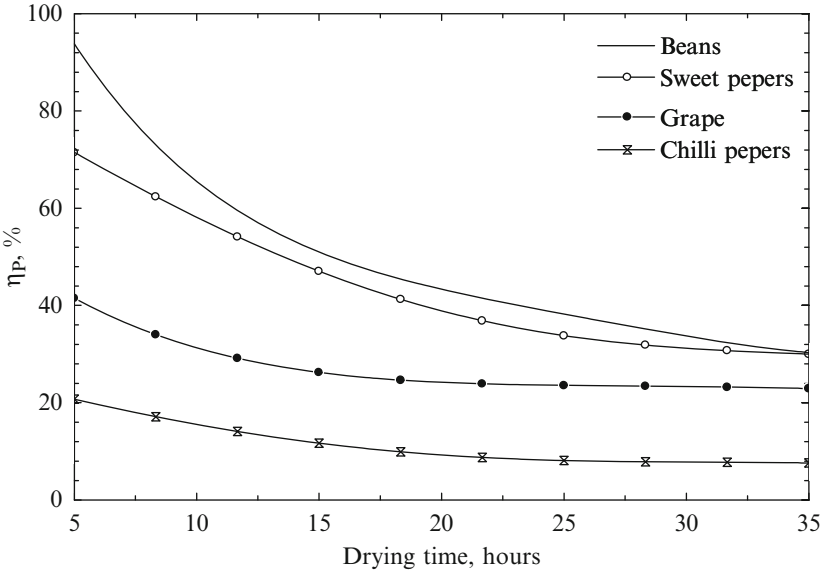

Fig. 9.21 Process efficiency of solar dryer for food products [data from Tiris et al. (1995)]

process efficiency is in the range 30% to 80%, and higher air flow rates are recommended for obtaining higher efficiencies.

Illustrative Example: Solar Refrigeration

In this example, it is shown how absorption refrigeration systems save energy when driven by solar radiation during the summer. On a summer day there is high solar radiation, and at the same time there is a peak demand of air conditioning. However, due to a higher ambient temperature, power generation during the summer is lower. Thus, an absorption-driven refrigeration system has a better chance to have higher thermal-to-cooling efficiency than an electrically driven vapor compression system. A system using an absorption machine operating with a mixture of R22 and DMETEG (DiMethyl Ether Tetra Ethylene Glycol) is exemplified here based on the results by Dincer et al. (1996b). The system has been designed to provide 4.65 kW of cooling load at −5°C and operates at a condensation pressure of 16 bar and an evaporation pressure of 4.8 bar. The solar collector is thermally connected with the vapor generator of the absorption machine, which operates at 80° to 100°C. The coefficient of performance (COP) of the system is defined in the usual manner as

$$\mathrm{COP} = \dot{Q}_e / \left(A_c I_{T0} + \dot{W}_p\right),$$

where $\dot{Q}_e$ is the evaporator capacity (see Fig. 9.22a), I_{T0} is the insolation on tilted surface (in W/m^2), A_c is the collector area (in m^2); one also has $A_c I_{T0} \dot{Q}_g$, where $\dot{Q}_g$ is the vapor generator capacity. The results show COP is in the range of 0.3 to 0.6 and correlated with the generator temperature and the temperature difference between the absorber and the evaporator ($T_a - T_e$) and are presented in Fig. 9.22b.

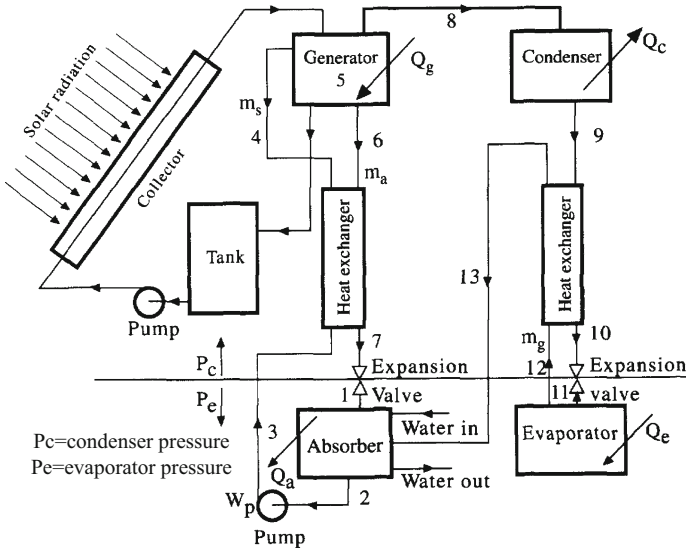

(a) The system

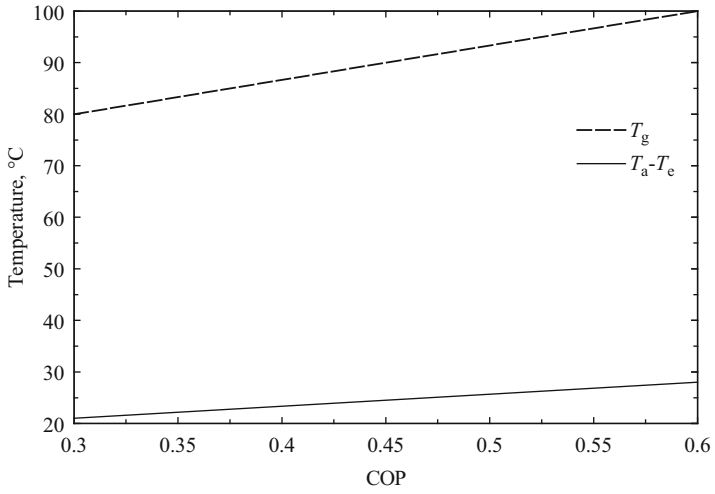

(b) The COP correlated with system temperatures

Fig. 9.22 Solar absorption refrigeration system operating with R22-DMETEG [modified from Dincer et al. (1996b)]

9.2.3 Solar Electricity

The classification of solar conversion systems from Fig. 9.2 suggests two major paths to generate electric power from solar energy: photovoltaics (where electricity is obtained by direct conversion of solar energy) and conversion of solar thermal

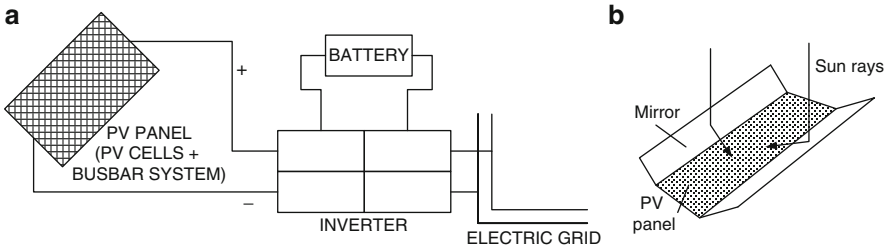

Fig. 9.23 (**a**) Simplified PV system diagram and (**b**) a V-trough concentrator

energy into mechanical energy followed by conversion of mechanical energy into electrical energy. There also may be some additional ways to generate solar electricity, namely by producing synthetic fuels with solar thermal energy and then converting the fuels into electrical energy by combusting them either in mechanical systems connected with heat engines or in fuel cell systems. However, one may argue that this path is rather a means of storage of solar energy for longer durations, because it has the quality to decouple the energy production from energy demand. We will focus in the next two sections on the photovoltaic system and solar-driven heat engines dedicated to generating electricity as the sole product.

9.2.3.1 Photovoltaic Systems

Photovoltaic systems comprise a number of elements such as photovoltaic panels, a tracking system (in some cases), an inverter (grid connection system), and an electrical storage system (batteries, reversible fuel cells together with hydrogen storage tank, or fuel cell/water electrolyzer system), such as indicated in a simplified manner in Fig. 9.23a. The most important component of these is the PV panel. The elemental component of a PV panel is the PV cell, which is a p–n semiconductor junction exposed to solar radiation. As already discussed above, the photons incident on the p–n junction dislocate electric charges in the form of electron–hole pairs. The many semiconductor junctions (PV cells) that constitute the PV panel are connected to a busbar system to form a series of parallel networks of sources. On the surface of the panel there is a "competition" for space occupation between the PC cells and the busbar system. On the one hand, one needs to install as many PV cells as possible per square meter of panel to have a higher number of electric generators; on the other hand, one needs to allocate as much space as possible to the busbar system in order to reduce the internal resistance of the panel. Thus, the efficiency of the PV panel can be written as the product of the PV cell efficiency and the efficiency of the busbar.

The efficiency of the PV cell itself (the semiconductor junction) is mostly affected by the filling factor. The operating temperature also affects the cell efficiency. Silicon-based and Ga-As-based semiconductors are currently the most used in PV panels because their price and efficiency are well balanced. Table 9.3 gives the efficiency of some PV cells for air mass zero and the beginning of

Table 9.3 Characteristics of the main types of PC cells

Cell type	Mass (kg/m^2)	Cost (k/m^2$)	Cost (k$/kg)	Efficiency (%) 28°C	58°C	η_{cell} at 100°C	$\eta_{cell,conc}$ at 100°C[a]
Si (200 μm)	0.55	11.0	20	13.5	11.9	9.7	17.0
High η Si (100 μm)	0.28	14.0	50	16.0	14.2	11.6	20.3
Double junction (100 μm)	0.83	116.2	140	22.0	20.7	18.8	32.9
Triple junction	0.85	127.5	150	25.0	23.3	20.9	36.6
Quadruple junction	0.86	133.3	155	28.8	26.8	24.1	42.2

η given with respect to 1,350 W/m^2 incident normal radiation
Data from Joshi et al. (2009b)
[a]At $C = 1.75$

life conditions at three temperatures: 28°C, 58°C, and 100°C. Note that higher operation temperatures on PV cells can be due to the solar radiation concentration.

For a concentration ratio of 1.75 the cell temperature becomes about 100°C. Note that the efficiency of the PV cell decreases with increasing temperature and increasing light concentration. However, the overall effect of light concentration is an increased efficiency of the cell, where the efficiency of the panel is given by

$$\eta_{cell,conc} = \eta_{cell} \times C, \tag{9.28}$$

where $\eta_{cell,conc}$ is the efficiency of the cell subjected to concentrated radiation. In Table 9.3, both the η_{cell} and $\eta_{cell,conc}$ for the 100°C operation temperature case are indicated. Note that a concentration as small as 1.75 can be easily obtained by adding side mirrors (known as V-trough concentrators) to the PV panel. The principle of V-trough concentrators is illustrated in Fig. 9.23b.

For each PV cell type Table 9.3 shows the weight per unit of the panel surface assembled with the respective cells and the cost per unit of panel weight. Currently, intensive research efforts are being pursued for development of PV cells with a quadruple semiconductor junction on a wafer. Table 9.4 lists the efficiencies of the components involved in a photovoltaic installation. For electricity storage, two cases can be considered: electricity storage in batteries and in reversible fuel cells. In the last case the storage medium is hydrogen (and possibly oxygen). The efficiency of the storage is defined as the energy retrieved per energy stored. In the reversible fuel cell system the efficiency is about 56% (energy) and 52% (exergy) for hydrogen/oxygen generation from water electrolysis during the storage phase and about 60% for the electricity retrieved during fuel cell operation of the storage system. Thus the storage efficiency is about 25% (energy) and 23% (exergy). If batteries are used for storage, approximately the same efficiency is expected.

The efficiency of a grid-connected system is represented by the product of the efficiency of the PV panel, the inverter efficiency, and the efficiency of other system

Table 9.4 Average energy and exergy efficiencies of the components of a photovoltaic plant

Component	Energy efficiency	Exergy efficiency
Photovoltaic panel	Monthly power generation as delivered to the grid per incident solar radiation per unit of area	Monthly power generation as delivered to the grid per incident solar exergy per unit of area
	11.2–12.4%	9.8–11.5%
Charge regulators	D.C. power output over D.C. power input	D.C. power output over D.C. power input
	85–90%	85–90%
Inverter	A.C. power delivered to the grid per D.C. power input	A.C. power delivered to the grid per D.C. power input
	85–90%	85–90%
Electricity storage (battery, reversible fuel cell)	Energy retrieved per energy stored (Note: in reversible fuel cells hydrogen is the storage medium)	Exergy retrieved per exergy stored
	25%	23%

Data from Joshi et al. (2009b)

components (η_{other}) such as electrical cables and resistors. Note that a grid-connected system may not require electricity storage systems. Thus, the grid-connected system without storage has an efficiency of

$$\eta_{\text{PV,GC}} = \eta_{\text{panel}} \times \eta_{\text{inverter}} \times \eta_{\text{other}}. \tag{9.29}$$

The annual average of a typical grid-connected PV system (without storage) is about 6%, while the inverter's annual average efficiency is 75%, and that of PV panel itself about 7% to 8%. If the system comprises electricity storage (the case in which it is not necessary for the system to be grid connected), the annual efficiency is about 3%.

Calculation of energy and exergy efficiency of the PV cells is based on Eq. (9.18); however, when PV cells are used within a PV panel, the arrangement is such that the cells necessarily heat up while they are exposed to heat transfer toward a colder environment. Thus the generated exergy by the panel is on one side electrical ($\dot{E}x_{\text{el}} = \text{FF} \times V_{\text{oc}} \times I_{\text{sc}}$) and on another side thermal, namely $\dot{E}x_{\text{th}} = (1 - T_0/T_{\text{cell}}) \times (UA)_{\text{cell}} \times (T_{\text{cell}} - T_0)$; this thermal exergy is lost. Thus the exergy efficiency of the PV cell is

$$\begin{aligned}\psi_{\text{PV}} &= \frac{\dot{E}x_{\text{el}} - \dot{E}x_{\text{th}}}{\dot{E}x_{\text{solar}}} \\ &= \frac{\text{FF} \times V_{\text{oc}} \times I_{\text{sc}} + (1 - T_0/T_{\text{cell}}) \times (UA)_{\text{cell}} \times (T_{\text{cell}} - T_0)}{(1 - T_0/T_{\text{S}}) I_{\text{T0}}},\end{aligned} \tag{9.30}$$

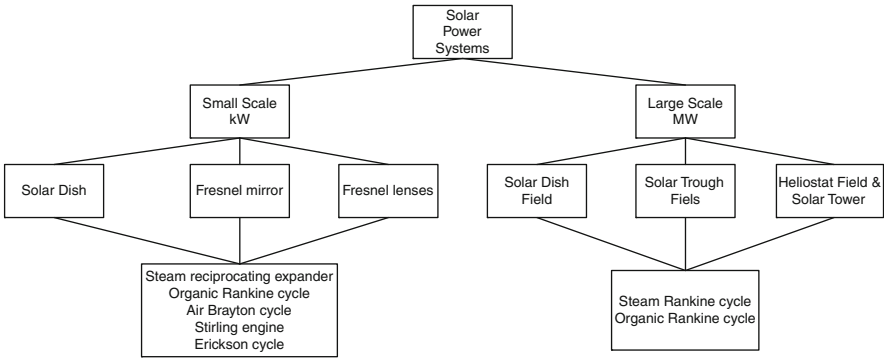

Fig. 9.24 Solar heat engines for power generation [modified from Zamfirescu et al. (2008)]

where I_{T0} is the global solar radiation on a tilted surface, while I_{sc} represents the short circuit current of the PV cell. The quantity $(UA)_{cell}$ represents the product of the superficial heat transfer coefficient between the panel and surroundings and the heat transfer area associated with the panel. Because of the associated heat losses, the exergy efficiency of the solar panel is lower than the energy efficiency by about 2%.

9.2.3.2 Solar-Driven Heat Engines for Power Generation

Solar-driven heat engine systems for power generation consist of solar-concentrating collectors that generate high-temperature heat to drive heat engines (e.g., Rankine or Brayton cycles). The heat engine produces shaft work that in turn drives an electrical generator. Such systems can be connected to the grid or they can work independently, such as the case in which electrical energy storage is applied to compensate for the intermittence of the solar source. In larger systems, a field of collectors is used to capture the solar energy, which is transmitted by means of a heat transfer fluid or a solar-produced synthetic fuel to a centralized power plant. In small-scale systems every individual unit is equipped with a low-power heat engine, usually placed in the focal point of a solar concentrator, close to the solar receiver. Small-scale systems are mainly based on paraboloidal dish solar-concentrating collectors.

In Fig. 9.24, a classification of solar power plant systems that use heat engines driven by solar thermal energy is suggested. The systems were classified into two categories: small-scale production capacities (of the order of kW) and large-scale ones from a few MW to hundreds of MW installed capacity. The type of solar concentrator and the type of heat engine for each category are indicated.

Low-power generation systems that normally use Rankine power generators operated with organic fluids (e.g., toluene), known also as organic Rankine cycles (ORC), are believed to be the most effective. Ammonia–water, ammonia, and other refrigerants are also working fluids worth considering in Rankine engines of low capacity that can use low-cost refrigeration compressors of the scroll or screw

type in reverse, namely as expanders. This feature increases the marketability of independent low-power solar-driven generators.

Other heat engine options are Stirling engines, which operate at very high pressures, of the order of 200 bar, and temperatures in the range of 700° to 800°C working with helium or hydrogen. Moreover, hydrogen is highly flammable, which imposes severe safety issues. A drawback with these systems is that hydrogen and helium leak easily, which raises maintenance problems. However, Stirling systems are very compact and reach high engine efficiency, which is around 40%, according to the review by Zamfirescu et al. (2008), leading to overall electricity production efficiency of 22% to 23% for 10 h/day operation and installed capacity of 10 to 25 kW. One of the main drawbacks of using Stirling engines in solar applications is the long warm-up time needed, which is at odds with the reality of solar energy's fluctuating nature.

Open-air Brayton cycle engines mounted at the dish focal point were also used in some applications (see Zamfirescu et al. 2008). They operate efficiently at higher receiver temperatures than what are usual for Stirling and Rankine cycles, that is, over 1,000°C where Brayton engines may attain over 26% efficiency. These cycles operate with air at once passing and they use internal heat recovery through heat exchanger between the incoming and outgoing flows.

Regarding large-scale solar technology, significant progress has been made with nine power-generating stations totaling 354 MW power-generating capacity that were built in California's Mojave Desert by the 1980s. These systems use parabolic trough collectors to collect heat and generate steam for a Rankine cycle. On average, large-scale solar trough steam power plants obtain 120 to 175 W of electric power per square meter of solar collector at a 350°C steam temperature.

Most of the large-scale solar plants are hybridized with natural gas or coal combustion. Figure 9.25 presents a significant example of a hybridized power plant. The net capacity of such systems, known as integrated solar combined cycle systems, is at least 10% for a capital cost of $3–5 million per installed MW.

The second representative large-scale power plant technology is based on solar tower concentrators. Dish-based systems are more cost competitive than parabolic troughs, mainly due to their better performance. Table 9.5 presents the main performance parameters of three kinds of nonhybridized large-scale solar power generation systems. The levelized electricity cost (see definition below) decreases with the installed performance.

Solar power plants entail lower maintenance costs than do fossil fuel power plants. The levelized cost of generated electricity is therefore affected mainly by the investment cost. According to the definition, the levelized electricity cost (LEC) is calculated based on the capital cost (CC), the maintenance cost (MC), and the lifetime (LT) according to the following basic equation:

$$\mathrm{LEC} = (\mathrm{CC} + \mathrm{MC})/(\mathrm{LT} \times \eta_{\mathrm{e}} \times \bar{I}_{\mathrm{T0}}), \tag{9.31}$$

where η_{e} is the solar to electrical energy conversion efficiency and $\bar{I}_{T0}$ is the global solar radiation averaged over the lifetime of the system.

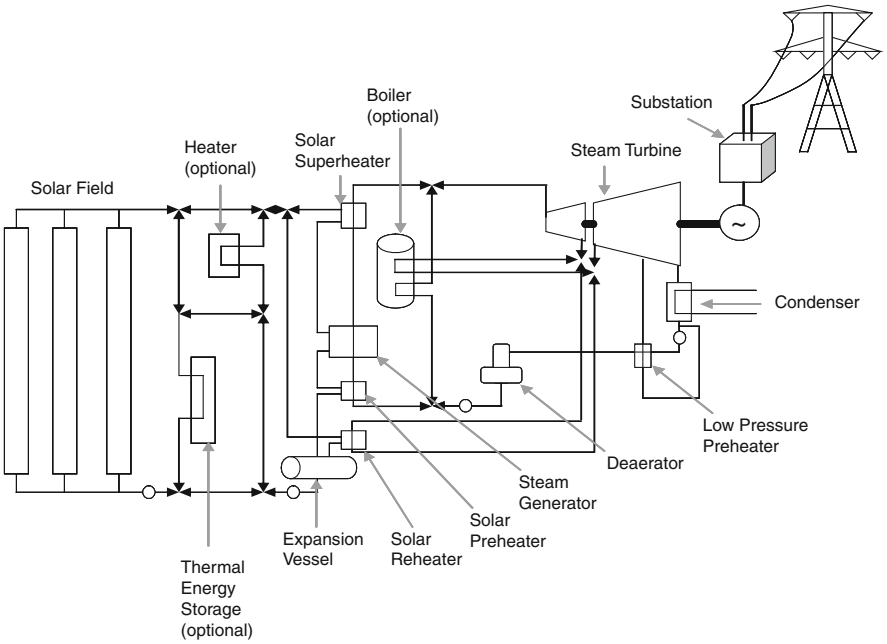

Fig. 9.25 Schematic of a hybrid solar trough power plant [modified from Zamfirescu et al. (2008)]

Table 9.5 Summary of performance of large-scale systems

Technology	Parabolic trough + oil	Solar tower system	Solar dish field
Mean net efficiency	14%	14%	20%
Specific power generation (kW h/m^2 year)	308	316.5	340
Levelized capital costs (\$/kW h_e year)	2.39	4.22	2–4
Operation and maintenance (¢/kW h)	4.96	6.05	4–6
Levelized electricity cost (LEC) (\$/kW h_e)	0.248–0.295	0.240–0.310	0.2–0.4

Data from Zamfirescu et al. (2008)

9.2.3.3 Solar Electric Storage

All large-scale systems are equipped with solar energy storage facilities. Solar power plants use typically high-temperature thermal storage in molten salt. Solar dish fields with centralized power generation are believed to be the most viable solution for the future because they provide the highest efficiency among all other systems. Chemical storage has been also applied in a test, using either the ammonia decomposition/synthesis loop or the sulfur trioxide $2SO_3 + 196.4\,\text{kJ/mol} \leftrightarrow 2SO_2 + O_2$, chemical loop for thermochemical storage or the loop based on ammonium hydrogen sulfate $NH_4HSO_4 + 132\,\text{kJ/mol} \leftrightarrow NH_3 + H_2SO_4$. In Chapter 11 we provide more information about thermal energy systems applicable to solar energy.

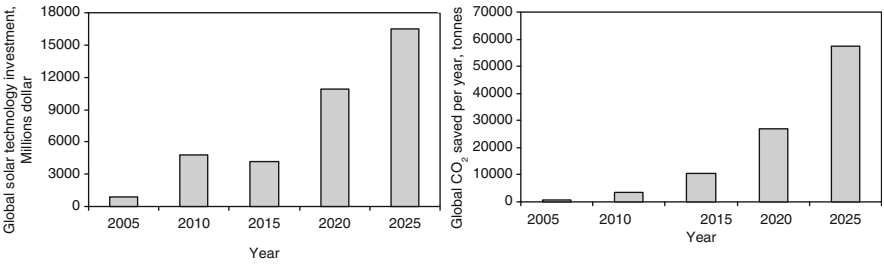

Fig. 9.26 Predictions of solar-electric technology investment and the resulting CO_2 mitigation [data from Zamfirescu et al. (2008)]

9.2.3.4 Solar Electric Applications

Obviously, solar electric power generation can be applied to a broad range of applications. Solar generators can operate either stand-alone or as grid-connected systems for electricity generation. One remarkable application is to use solar electricity to drive electrolysers for hydrogen generation. This application is discussed in detail in Chapter 13.

Water irrigation systems with electricity generated by PV panels to drive pumps became familiar in recent decades. Other applications of PV electricity are for highway signaling, remote located traffic indicators, and many other remote systems or aerospace applications. Thermoelectric concentrated solar generators are of medium to large scale. Low-scale concentrated power system (CSP) using heat engines appear to be an emerging technology that is not yet commercially available. Concentrated solar power generators were also found to be an attractive option for satellites and space missions, in which they operate outside the terrestrial atmosphere.

Two important advantages of solar electricity are reducing pollution and mitigating the release of CO_2. It is predicted that solar electric systems will proliferate in future years. The carbon dioxide mitigation can be estimated based on the installed electric power production capacity that replaces fossil fuel power plants. Zamfirescu et al. (2008) reported a correlation between the predicted evolution of investments in solar electric power technology and the carbon dioxide saved per annum (Fig. 9.26).

9.2.4 Solar to Biochemical Energy Conversion

Another route to solar energy conversion, indicated in the general classification form in Fig. 9.2, is the solar-biochemical one. In this case, special organisms are able to conduct light-stimulating enzymatic processes that convert biological matter from various substrates into biochemical energy present in various organic

molecules such as glucose, sucrose, carbohydrates, and fibers. Some of the bacteria generate combustible gases like hydrogen, ammonia, or methane. Green leaf plants perform the photosynthesis reaction, which mainly leads to fiber formation and the growth of the plants. Plants themselves are the source of the biomass, which, as already mentioned, is one of the renewable energy sources on the earth. Conversion of solar energy through hydrogen via the biological route is explained in detail in Chapter 13, where some general aspects regarding photo-bio-chemical energy conversion are also discussed.

9.2.5 Solar Multigeneration Systems

One principal characteristic of solar radiation is that it embeds two kinds of useful energies in it: light (or photonic radiation) and heat (or thermal radiation. It is known that the infrared spectrum of the solar radiation is viewed as a form of heat. When solar radiation is used to generate electricity, a part of the harvested energy is lost and converted into heat. It makes good sense to generate electricity and heat from solar radiation. In this way, much better solar energy utilization is achieved than with systems that generate only electricity or heat.

Moreover, it is possible to generate more products than heat and electricity from solar radiation with only one system. Electricity, high-temperature heat, low-temperature heat, refrigeration, hydrogen, oxygen, synthetic fuels, and chemicals can be generated simultaneously or in various combinations using solar energy. In Chapter 12 we discuss integrated multigeneration systems, which use various kinds of primary energy sources including solar. Two kinds of solar multigeneration systems have received much attention in recent years, namely photovoltaic/thermal systems and concentrated solar heating and power systems. Both of these are known as solar cogeneration systems. We discuss in this section only the solar cogeneration systems and refer the reader to Chapter 12 for some examples of solar multi-generation systems.

9.2.5.1 Photovoltaic–Thermal Systems

If exposed to a low solar concentration ratio, the temperature of a PV panel increases, as mentioned above. In this case, the PV cell efficiency decreases, but the overall panel efficiency increases. There is a limit to the operating temperature of the PC cells, which, depending on the construction, is in the range of about 60° to 100°C. Lowering the PV panel temperature is a means of increasing the efficiency. If cooling is applied with the help of a heat transfer fluid to a PV panel, its temperature can be maintained between 40° and 80°C (depending on the solar radiation intensity and on whether concentration systems are applied). The heat recovered from PV panel cooling is thus a good level of temperature to be used in a multitude of applications. Consequently, PV/T (photovoltaic–thermal) systems

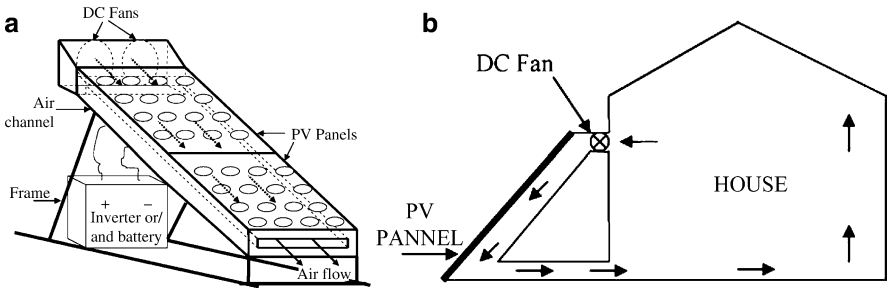

Fig. 9.27 Typical arrangement of PV/T systems using air as the heat transfer fluid (**a**) and their application in space heating (**b**) [modified from Joshi et al. (2009b)]

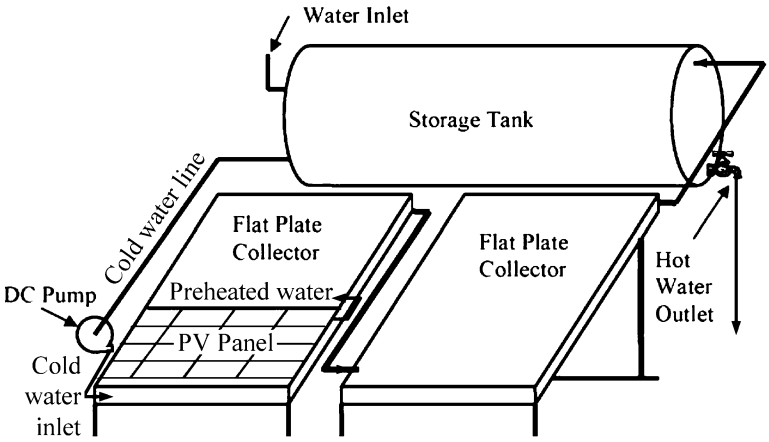

Fig. 9.28 Hot water production with PV/T systems [modified from Joshi et al. (2009b)]

make sense for both increasing the efficiency of power generation and increasing the efficiency of solar resource utilization.

Water, glycol–water, and air are typical heat transfer fluids used in PV/T systems. Hot water can be used for space heating, sanitary water heating, greenhouse heating, solar drying, solar stills, and other purposes. A typical PV/T arrangement that uses air as the heat transfer fluid is illustrated in Fig. 9.27a. The warmed air produced by such a system is at a sufficient temperature for supplying a crop drying facility or for heating a living space as in the arrangement suggested in Fig. 9.27b. When water is used as the cooling medium, arrangements can be made to combine PV technology with a flat plate solar thermal collector. Thus, water at its lower temperature can flow underneath a PV panel so that, through heat transfer, it cools the panel and improves its efficiency. Water is preheated in this way and then passed through flat plate solar thermal collectors for further heating. The diagram of a system as such, used for space and water heating in a residence, is suggested in Fig. 9.28.

The energy and exergy efficiency of the cogeneration system are usually defined as useful electricity and heat generated, expressed in energy or exergy units, respectively, over the consumed solar resource (again in energy exergy units). Thus the energy efficiency can be considered the resource utilization efficiency as, according to its definition, this efficiency is equivalent to the sum of the electrical and thermal efficiencies: $\eta_{cog} = \eta_e + \eta_{th}$. It is also possible to define the energy efficiency of the cogeneration system considering that the electricity is a more valuable product than the heat (Joshi et al. 2009b).

Assume that one disposes of some amount of thermal energy. A good power plant can convert this heat into electricity with $\eta_{PP} = 30$–40% energy efficiency. Thus, in order to generate a quantity of electricity W_e, the amount of heat generated is $Q_e = W_e/\eta_{PP}$. In a cogeneration system, the useful output can be expressed as the sum of the equivalent thermal energy used to generate electricity (Q_e) and the thermal energy that is used as heat (Q_{th}). Thus, the amount of useful heat is ($Q_e + Q_{th}$). By dividing this heat by the total solar energy used we obtain

$$\eta_{cog} = \frac{Q_e + Q_{th}}{I_{T0}} = \frac{W_e/\eta_{PP}}{I_{T0}} + \frac{Q_{th}}{I_{T0}} = \frac{\eta_e}{\eta_{PP}} + \eta_{th}. \tag{9.32}$$

Note that in the above equation the energy quantities are expressed per unit of irradiated surface and I_{T0} is the global solar radiation on the tilted surface. According to general practice (see Joshi et al. 2009b), it is customary to assume the electricity generation efficiency $\eta_{PP} = 38\%$. Thus, a typical air-based PV/T system, which may have a thermal efficiency of 40% and a PV electric efficiency of 8%, corresponds to a solar energy utilization efficiency of 8% + 40% = 48% if the electricity and heat production are directly added, or, if Eq. (9.30) is applied, the cogeneration energy efficiency becomes $8\%/0.48 + 40\% = 57\%$ which is more meaningful.

Solar stills use thermal energy from solar radiation to force water evaporation in a closed environment with the purpose of purifying or distilling brackish water with high salinity. Solar stills can be in this case coupled with a PV panel in order to run the necessary pumps within a PV/T kind of arrangement.

The exergy efficiency of the PV/T systems is substantially higher than that of simple PV systems because of their ability to recover and use the heat generated by the panel. The exergy efficiency of a PV cell that makes part of a PV/T assembly can be estimated by

$$\begin{aligned}\psi_{cog} &= \frac{\dot{E}x_e + \dot{E}x_{th}}{\dot{E}x_{solar}} \\ &= \frac{FF \times V_{oc} \times I_{sc} + (1 - T_0/T_{cell}) \times (UA)_{cell} \times (T_{cell} - T_0)}{(1 - T_0/T_S) I_{T0}}.\end{aligned} \tag{9.33}$$

Table 9.6 System parameters for the experimental PV/T system

Parameter	Value
PV module efficiency	15%
Short circuit current of PV module	4.8 A
Area of the module	139 cm^2
Number of modules per panel (series connected)	36
Open circuit voltage of the panel	21.7 V
Heat loss coefficient from glassing	2.8 W/m^2 K
Heat loss coefficient from channel bottom	0.62 W/m^2 K
Average air velocity in PV/T duct	2 m/s
Tilt angle (New Delhi)	28°

Data from Joshi et al. (2009c)

Exergy efficiency of air-cooled PV/T system is about 30% higher than that of the system wasting the heat generated by the PV panel. Based on the data from Joshi et al. (2009b), it can be estimated that if water is used as the heat transfer fluid, then the solar energy utilization efficiency becomes 25% higher than that of air-cooled PV/T, which means as much as double with respect to PV-only systems. The efficiency of the PV/T panel can be increased even more if a V-concentrator is applied, which leads to an increase of PV/TR efficiency of up to 30% with respect to settings without the concentrator.

Illustrative Example: PV/T System

An experimental PV/T system built and tested at IIT Delhi by Joshi et al. (2009c) is presented here to demonstrate the performance achievement and the system parameters. The experimental setting is similar to that described graphically in Fig. 9.27a; basically, it heats air by flowing it underneath the PV panel, using for this purpose a fan that consumes the electrical energy generated by the panel itself. The calculation of the efficiency of the system takes into account that a part of the generated power is internally consumed.

In Table 9.6, the general constructive parameters of the system are presented. Its panel is made from modules connected in series. The air channel underneath the panel is thermally insulated for better transmission of the thermal energy into the air. The system measures the temperature, air velocity, light intensity, and electric current/voltage probes every hour. The obtained readings for one typical summer day are presented in Fig. 9.29. It can be observed that the temperature difference between the warm PV cell and the exterior temperature is significant, varying from 9°C in the morning to 17°C at noon and to 4°C in the evening. This amount of temperature difference shows that there is a rather good potential to recover thermal energy from the air.

The energy and exergy efficiencies obtained with the PV/T system are presented in Fig. 9.30. For facilitating data interpretation, the variation of the global solar radiation is superimposed on the same figure. In the morning, when the solar radiation starts to grow in intensity and the panel surface temperature is reduced, the electrical efficiency of the system is high (10.5%). At noon, when the solar

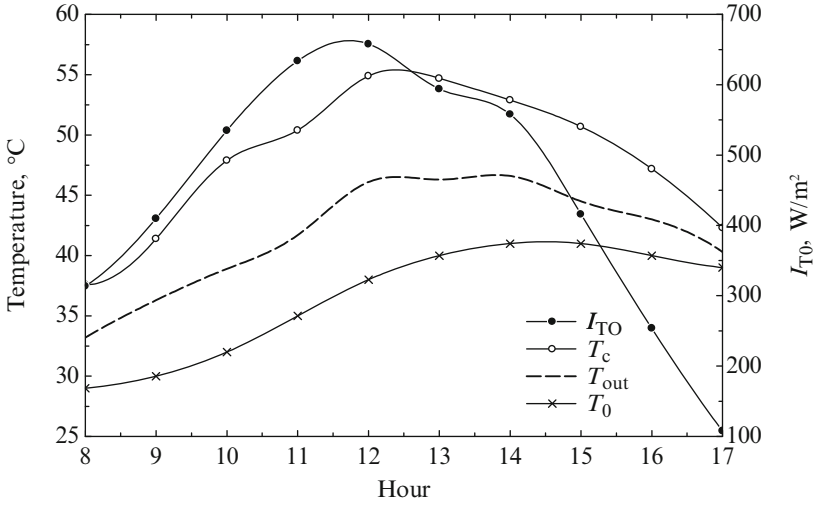

Fig. 9.29 Recorded experimental data for the PV/T system by Joshi et al. (2009c) for a typical summer day in New Delhi [data from Joshi et al. (2009c)]

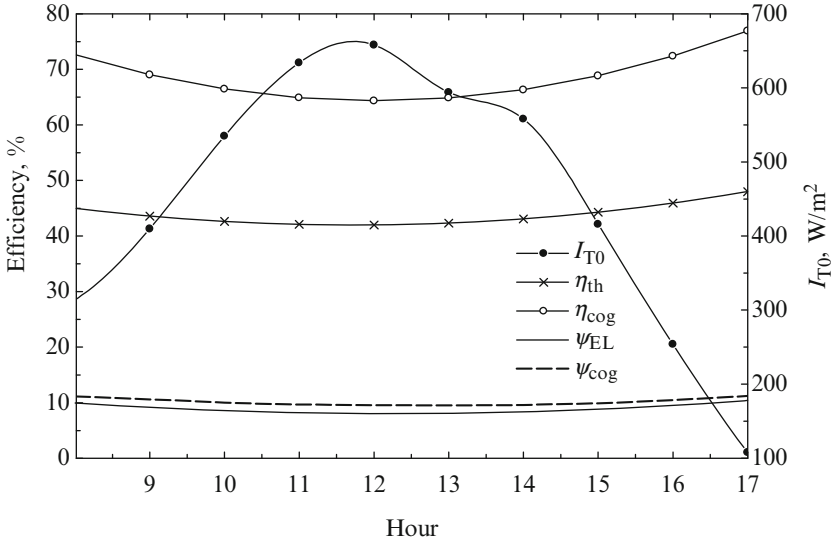

Fig. 9.30 Experimentally determined efficiencies of the PV/T system by Joshi et al. (2009c) [data from Joshi et al. (2009c)]

radiation reaches its highest value, and so does the panel's temperature, the electrical efficiency of the system is the lowest. We can conclude that the degradation of the electricity output due to the increase in cell temperature is more important than the increase in power generation due to the higher solar radiation intensity at noon.

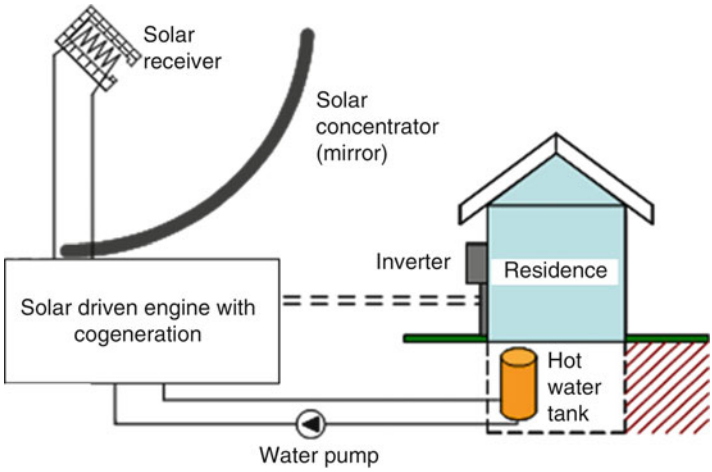

Fig. 9.31 Heat engine system for solar power and heating generation [modified from Zamfirescu et al. (2009)]

The beneficial effect of the continuous cooling of the panel with air can be observed in the early afternoon, when the radiation level is still high but the temperature of the panel stabilizes and so does the electrical efficiency.

The data from Joshi et al. (2009c) have been used here to calculate the exergy efficiencies plotted in Fig. 9.30. The exergy efficiency of the system has been calculated using the energy efficiency data and the Carnot factor associated with the solar radiation, which is $(1 - T_0/T_{\text{sun}})$, where for solar temperature we assumed here 5,777 K. The overall system efficiency has been calculated from energy efficiency data for electrical and thermal generation, according to Eq. (9.32). For calculating the exergy efficiency at heat generation the air output temperature has been used to determine the associated Carnot factor.

As observed on the figure, the system reached maximum cogeneration energy efficiency during the evening (75%) and maximum cogeneration exergy efficiency during the morning (11%). The average thermal efficiency is 44%, and the average electric energy efficiency is 9.5%.

9.2.5.2 Solar Heat Engines for Cogeneration

Solar energy is an excellent resource to supply high-temperature thermal energy to heat engine systems for cogeneration of power and heating. Figure 9.31 shows the schematics of such a system applied for a residence. During the daytime the heat engine generates power and heat at a higher rate than consumption. The additional power is either stored in batteries or delivered to the grid. The excess thermal energy is stored as hot water in an insulated tank. Thus the energy consumption is levelized such that the needs of heating and power during the night are partly or totally covered by the storage.

The heat engine is connected thermally at the low-temperature side with the water stream (or other heat transfer fluid, e.g., glycol, air, etc.), which recovers the heat that otherwise would be ejected by the heat engine at the rate $\dot{Q}_{\mathrm{HR}}$ while generating electric energy at the rate $\dot{W}_{\mathrm{E}}$. The solar concentrator continuously tracks the sun, which irradiates solar energy at the intensity I_{T0} on the aperture area A_{a}. The electric and thermal efficiencies of the system are written as

$$\left.\begin{aligned}\eta_{\mathrm{th}} &= \frac{\dot{Q}_{\mathrm{HR}}}{I_{\mathrm{T0}} A_{\mathrm{a}}} \\ \eta_{\mathrm{e}} &= \frac{\dot{W}_{\mathrm{E}}}{I_{\mathrm{T0}} A_{\mathrm{a}}}\end{aligned}\right\}, \tag{9.34}$$

while the cogeneration efficiency can be calculated with Eq. (9.32) and the cogeneration exergy efficiency with $\psi_{\mathrm{cog}} = \left(\dot{E}x_{\mathrm{e}} + \dot{E}x_{\mathrm{th}}\right)/\dot{E}x_{\mathrm{solar}}$.

One relevant advantage of such cogeneration system comes from the opportunity to recover the rejected heat by the heat engine with minimal losses. The design of the system offers the possibility of applying good thermal insulation around it. In fact, the system may have a point or line focus solar concentrator, characterized by reduced thermal and optical losses (of 5–20% in total). Furthermore, the heat engine can be enclosed in an insulated box, forcing it to deliver the ejected heat only to the heat transfer fluid. Thus at the level of the heat engine a very small amount of heat is lost (it can be lower than 1%). Next, the storage of hot water is made at a reasonably low temperature (say 30°C to 95°C), a fact that facilitates the application of good, inexpensive thermal insulation for reducing the heat leakage (it may be another 1% to 2% from the solar heat). Thus, the solar energy utilization in such a system for heat and power cogeneration can be over 80%.

Two implementations are possible for solar-driven cogeneration engine, depending on the temperature level at which the thermal energy is needed. These two possibilities are explained schematically in Fig. 9.32. The case (a) is the same as discussed above, which corresponds with the cogeneration system presented in Fig. 9.31. This is the case when low-temperature heat is needed (say 80°C to 200°C). In this case, it is advantageous to generate high-temperature concentrated solar heat and let the heat engine operate between T_{H} and $T_{\mathrm{HR}} < T_{\mathrm{H}}$.

If the thermal process served by the system requires high temperature, the system from Fig. 9.32b becomes the logical option. In this case, the concentrated solar heat is stored at the highest temperature. A part of the generated heat is delivered to the process, while the other part is supplied to a heat engine that operates between T_{HR} and the ambient temperature T_0. This option is particularly useful when a fuel is synthesized through a thermochemical process (viz., hydrogen). Chapters 12 and 13 discuss in detail the topics of multigeneration and hydrogen.

One important advantage of the solar cogeneration system (in particular those using heat engines) consists of the possibility of mitigating pollution and carbon dioxide emissions. The mitigation potential can be quantified if one introduces the parameter $\mathcal{M}_{\mathrm{CO_2}}$—the CO_2 mitigation—expressed in kg CO_2 mitigated per kWh

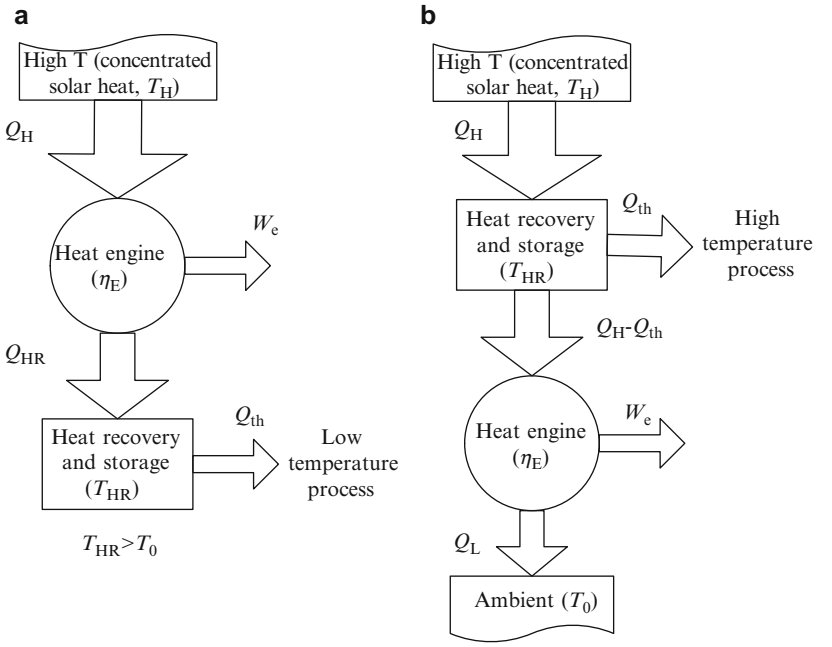

Fig. 9.32 General thermodynamic representation of heat engine systems for solar power and heat cogeneration. (**a**) Low-temperature heat; (**b**) high-temperature heat

of heat and power cogeneration. One can also denote $\mathcal{M}_W$ as the CO_2 mitigation due to avoiding electricity generation from fossil fuels (given in kg CO_2/kW $h_{electric}$) and $\mathcal{M}_Q$ as the CO_2 mitigation due to avoidance of conventional CO_2-emitting heating technologies (e.g., gas/coal combustion, electrical heat pumps). The dimensionless parameter $\tilde{\mathcal{M}}$ is defined as $\tilde{\mathcal{M}} = \mathcal{M}_Q/\mathcal{M}_W$. Note that the parameter $\tilde{\mathcal{M}}$ can vary from 0.5 if methane combustion is used, to 1 if direct electrical heating is used. With this notation the carbon dioxide mitigation $\mathcal{M}_{CO_2}$ can be calculated as

$$\mathcal{M}_{CO_2} = \mathcal{M}_W \frac{\dot{W}_e + \dot{Q}_{th}\tilde{\mathcal{M}}}{I_{T0}A_a} = \mathcal{M}_W\left(\eta_e + \eta_{th}\tilde{\mathcal{M}}\right). \tag{9.35}$$

It is shown in Zamfirescu et al. (2009) that heat engines used for power and low-temperature heat generation can mitigate at least three times more carbon dioxide than those without cogeneration. A typical figure for low-capacity solar cogeneration systems with heat engine is around 0.3 kg CO_2 mitigated per kWh of cogenerated power and heat. Note that some states and Canadian provinces started to adopt various carbon tax systems. British Columbia has already implemented a tax of $10 per ton of CO_2, expected to rise to $30 by 2012. By assuming a carbon tax of $30 per ton of emitted CO_2 in the atmosphere and a grid sell-back contract with the electrical utility at $0.80/kWh, Zamfirescu et al. (2009) showed that

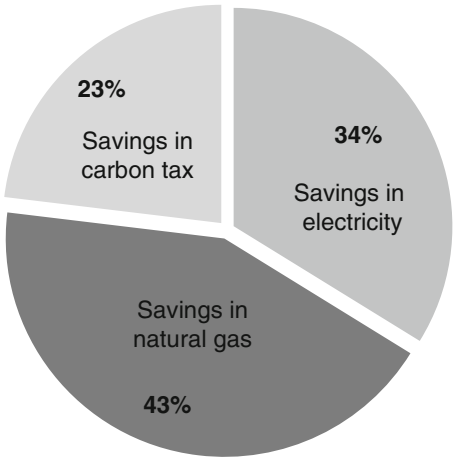

Fig. 9.33 Relative portions of financial savings from solar plant factors [data from Zamfirescu et al. (2009)]

low-capacity solar heat engines for power and heat cogeneration applied to typical Ontarian individual residences can have a payback period of 6 to 8 years. They also determined how much of the cost savings generated by the solar cogeneration system come from the reduction of electrical consumption, the reduction of natural gas (that without the system would be used for heating), and the carbon tax. These findings are summarized in Fig. 9.33, which shows that the largest part of the savings comes from solar heating.

9.3 Wind Energy

Wind energy is a significant renewable energy resource that has shown rapid growth in recent years. The cost of wind energy has come down enough that wind energy farms are now constructed in many locations around the world. Germany, Denmark, and Spain are three of the leading countries in installing wind energy capacities. Wind energy can be regarded as a meteorological variable signifying the energy content of the wind. The parameter that is important for meteorological modeling of wind is the wind velocity. In meteorology, an atmospheric boundary is considered for predicting the local or regional winds by simulation. Other meteorological variables such as temperature, pressure, and humidity of the atmosphere are also important in the occurrence of wind. Such information together with measured velocity data are necessary for determining locations where wind energy farms can be installed and for estimating their capacity and efficiency.

Wind is in fact a form of mechanical energy. It has to be harvested by appropriate engineered devices and converted into other useful energies such as electric energy. The major technical problem with a wind energy conversion system is the fluctuating

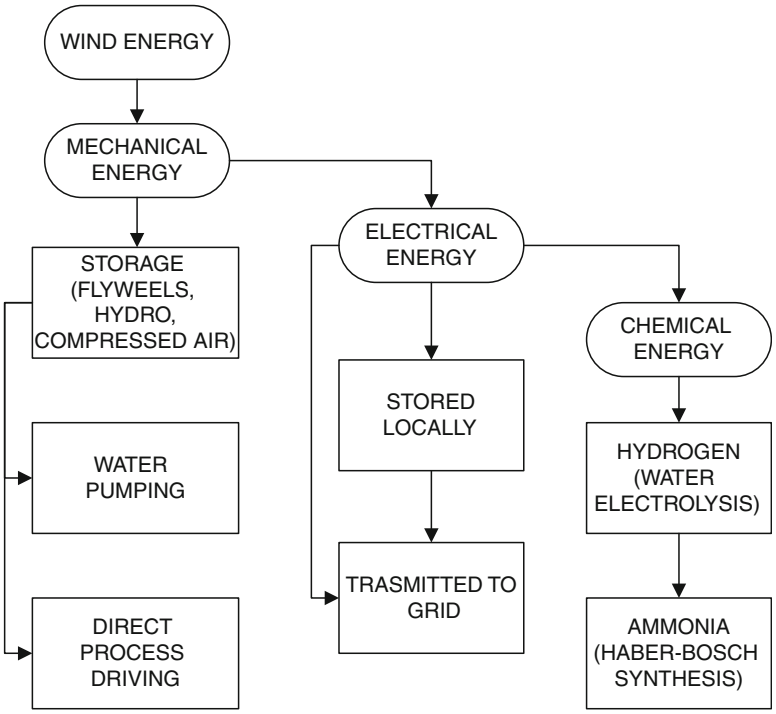

Fig. 9.34 Conversion paths of wind energy

and intermittent nature of wind. The harvesting system (typically a wind turbine) must react fast to the presence of wind or to a change in its direction and intensity. It is important to be able to store the mechanical energy harvested from wing. Several wind energy storage methods are possible, where the mechanical energy resulting from wind is stored in various forms: kinetic (flywheels), electrochemical (batteries), chemical (hydrogen), and thermomechanical (compressed air). Nevertheless, the most used systems are electrical generators actuated by wind energy and having local storage capacities in batteries and possibly being equipped with grid-connecting systems. Wind turbine efficiency reaches about 35% to 50% with the current technology.

The common conversion paths of wind energy are illustrated in Fig. 9.34. The harvested wind energy is normally converted in the shaft rotation of the wind turbine. The mechanical energy can then be used directly. For smooth generation, the mechanical energy can be stored in devices that are able to retrieve it in mechanical form, such as flywheels, hydrostorage, or compressed air. A typical direct use of wind energy is water pumping; others may be grain milling and wood cutting.

The shaft rotating mechanical energy can be converted by appropriate electric generators into electrical energy. The electrical energy can be stored locally or transmitted to the grid or further used for hydrogen generation through water

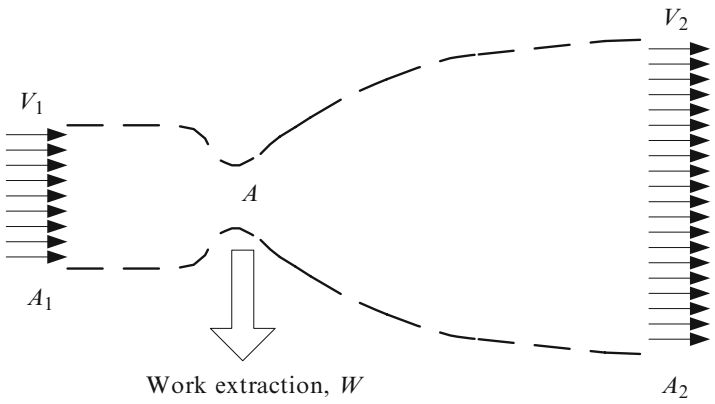

Fig. 9.35 Thermodynamic model for wind energy conversion

photosynthesis. Furthermore, hydrogen can be converted to ammonia through the well-known Haber–Bosch process; this process requires additional consumption of electricity.

9.3.1 Thermodynamic Limits of Wind Energy Conversion

As has been discussed, wind energy is an indirect form of solar energy. Therefore, from the thermodynamic viewpoint one can contemplate wind energy as a heat engine supplied with high-temperature solar thermal radiation at the source and ejecting lower-temperature heat in the terrestrial environment while generating the work necessary to move large masses of air.

9.3.1.1 Maximum Work Generation from Wind Energy

For thermodynamic analysis, a theoretical boundary can be drawn around the turbine for delimiting a control volume as indicated in Fig. 9.35. Outside this boundary, there is no significant modification of the velocity of air. In contrast, inside the control volume the air feels the presence of the turbine; thus, the turbine accelerates or decelerates according to the laws of energy conservation and applicable constraints. Basically, the upstream area of the control volume (A_1) is much smaller than the downstream area (A_2). Thus the velocity at the upstream (V_1) is much higher than the velocity downstream (V_2).

The geometry of the thermodynamic domain is similar to that of a nozzle that extracts work W from the wind. The average velocity of the wind is denoted by $\bar{V} = (V_1 + V_2)/2$, and the mass flow rate of air is approximated with $\dot{m} = \rho A \bar{V}$.

Thus, the rate of variation of wind momentum is $\dot{m} \times (V_2 - V_1) = \rho A\bar{V} \times (V_2 - V_1)$. Therefore, according to the second law of dynamics, the force exerted on the rotor is $F = -\rho A\bar{V}(V_2 - V_1)$. Based on the force and the average velocity, the work extracted by the rotor is $W = \rho A\bar{V}(V_2 - V_1) \times \bar{V}$. This work also can be calculated based on the kinetic energy variation of the air that is, $W = 0.5\rho A\bar{V}\left(V_1^2 - V_2^2\right)$. The equality of the two expressions for W results in $\bar{V} = (V_1 + V_2)/2$ which in fact justifies the definition of the average velocity as the arithmetic mean. Using the notation $\alpha = V_2/V_1$, one can obtain the work extraction as

$$W = \rho \frac{AV_1^3}{4}\left[(1+\alpha)\left(1-\alpha^2\right)\right], \tag{9.36}$$

where the quantities ρ, A, and V_1 should be assumed constant for the analysis; thus, for a given wind velocity, outside temperature and pressure (which fix the air density), and a given wind turbine area, the generated work is a function of the velocity ratio only, $W = W(\alpha)$. It is simple to show that the maximum work is obtained at $\alpha = 1/3$, which corresponds to

$$W_{\max} = \frac{8}{27}\rho \frac{AV_1^3}{4}. \tag{9.37}$$

9.3.1.2 Energy Efficiency and Wind Energy Maps

The energy efficiency of mechanical work production from wind energy must equal the useful shaft work generated per wind energy, both given per unit of turbine surface area. The wind energy is the kinetic energy (0.5). Thus the theoretical maximum energy efficiency of the wind energy conversion is

$$\eta_{\max} = \frac{(8/27)\rho(AV_1^3/4)}{(1/2)\rho AV_1^3} = \frac{16}{27} = 59.3\%. \tag{9.38}$$

Looking back to Eq. (9.36), the quantity between the square brackets defines the so-called power coefficient of the rotor efficiency given by

$$C_p = \left[(1+\alpha)\left(1-\alpha^2\right)\right]/2. \tag{9.39}$$

The turbine efficiency becomes

$$\eta = C_p. \tag{9.40}$$

As shown above, the maximum value of $C_{p,\max}$ is 0.593; however, the efficiency found in practice is in the range of 35% to 45%. With Eqs. (9.36) and (9.39) the work extraction reduces to

$$W = \rho C_p \frac{AV_1^3}{2}. \tag{9.41}$$

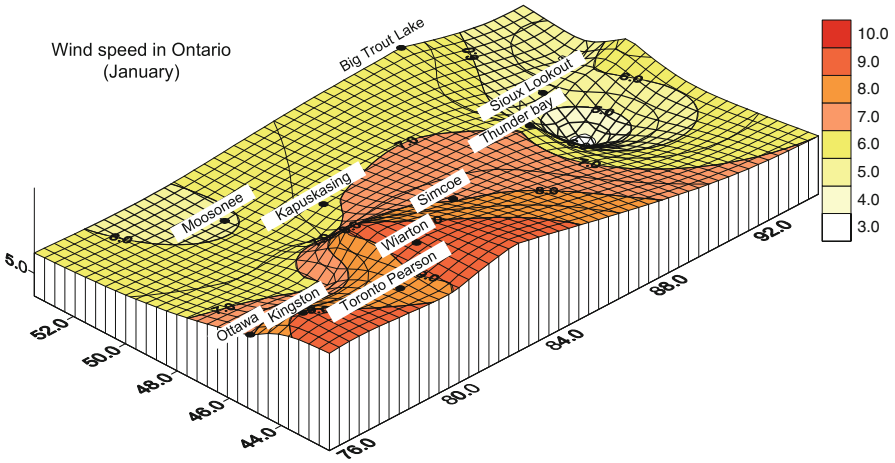

Fig. 9.36 Average wind speed distribution at a 30-m altitude in Ontario during January 3 (longitude, latitude, and amplitude are on the axes) [modified from Sahin et al. (2006)]

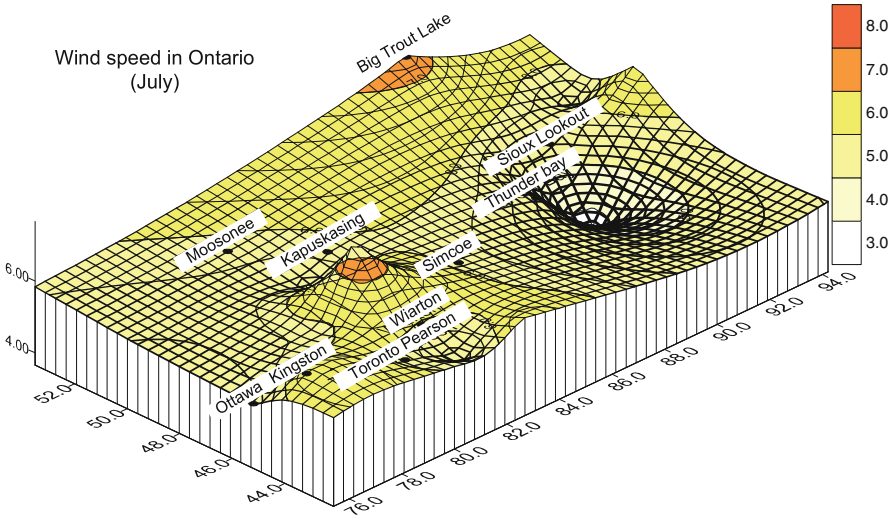

Fig. 9.37 Average wind speed distribution at a 30-m altitude in Ontario during July (longitude, latitude, and amplitude are on the axes) [modified from Sahin et al. (2006)]

Note also that during a period of time (e.g., day, month, season) the wind velocity (V_1) varies. Figures 9.36 and 9.37 exemplify wind velocity variation in Ontario during a winter month (January) and during a summer month (July), respectively.

The wind speed magnitude indicated in the maps is for a height of 30 m above ground, which is the average installation height of wind turbine rotors. In January low speeds are observed in the east and north parts of Ontario. The monthly

maximum average wind speed observed in southwestern Ontario is 9 to 10 m/s. The monthly minimum average value appears to be in Atikokan and it is below the typical wind turbine "cut-in wind speed," and as a result there is no electricity generation. In wind turbine technology, the cut-in wind speed is the minimum wind speed at which a typical wind turbine generator starts supplying electricity. Normally, the wind turbine turns the generator at increased speed when the wind velocity starts to grow. However, the generator does not produce enough voltage to supply the downstream equipment (inverter, battery, grid) unless the rotation speed passes a certain threshold.

This threshold is the cut-in speed and has values in a range, depending on the type of wind turbine and its construction; normally the cut-in wind speed is higher than 3 to 4 m/s. Wind speeds for July (Fig. 9.37) exhibit different clusters as a result of high heating during this month, which creates unstable surface conditions. The highest wind speed for this month is the lowest of the maximum of the other months. When the wind speed is too high it can damage the wind turbine; thus, if a certain higher wind limit is passed, the generator is disconnected from the turbine shaft so that the load is released and the turbine is protected against possible damage created by too high a stress; in this condition, the turbine does not generate velocity. Typically, this threshold wind speed, called the cut-off value, is about 20 to 25 m/s.

Another issue in wind energy conversion relates to the variation of the wind speed at a certain location during a year. The annual probability distribution of the wind velocity affects the total energy generated at a specific location during a year. The so-called Weibull probability distribution can be used to model the occurrence of wind velocity based on two parameters k and c, according to $h(V) = k/c(V/c)^{k-1} \exp\left[-(V/c)^k\right]$; for parameter $k = 2$, this probability distribution function is the Rayleigh distribution, which becomes

$$h(V) = \frac{2V}{c^2} \exp\left[-\left(\frac{V}{c}\right)^2\right]. \tag{9.42}$$

The Rayleigh distribution for annual variation of wind velocity is exemplified in the plot from Fig. 9.38 for the case $c = 7$ m/s; in the plot, the annual probability of occurrence of wind velocity is correlated with the cube of velocity. Two vertical lines are shown at a cut-in speed (V_{ci}) assumed to be 3 m/s and a cut-out speed (V_{co}) assumed to be 20 m/s. Outside the region delimited by V_{ci} and V_{co} the wind turbine does not operate. The hatched area from the plot, which correspond with the wind turbine operation domain, can be calculated with the integral

$$\int_{V_{ci}}^{V_{co}} h(V) d(V^3) = 100\% \times V_{RMC}^3, \tag{9.43}$$

where V_{RMC} denotes the so-called root mean cube wind velocity. Observe that Eq. (9.43) expresses the equality between the hatched area and the gray area from Fig. 9.38. The gray area defines the root mean cube wind velocity as an average

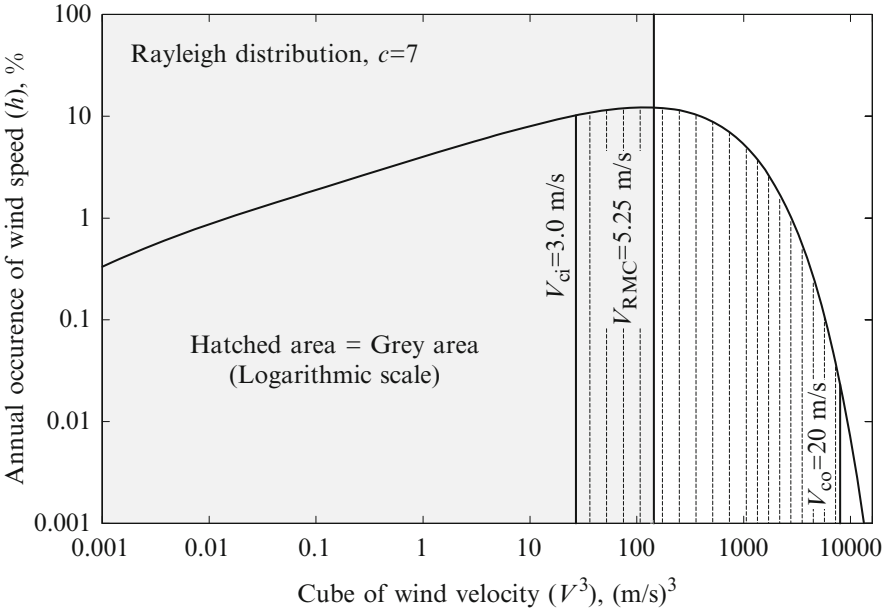

Fig. 9.38 Definition of the root mean cube wind velocity

velocity that has 100% occurrence and generates the same amount of wind energy as the probable velocity profile described by the adopted probability distribution function. Thus the generated mechanical energy by the turbine operating at a constant rate throughout the year, can be written as

$$W = \frac{1}{2}\rho C_{\mathrm{p}} A V_{\mathrm{RMC}}^3, \tag{9.44}$$

where

$$V_{\mathrm{RMC}}^3 = \int_{V_{\mathrm{ci}}}^{V_{\mathrm{co}}} h(V)\,\mathrm{d}(V^3). \tag{9.45}$$

When a wind turbine is to be selected for a location, it is important to know what is the average wind velocity in that location, because the turbine energy efficiency is specified by the manufacturer at a rated value that corresponds to a rated wind velocity (V_{r}). If the wind velocity is different from the turbine rating value, then a capacity factor can be used (as indicated by the manufacturer) to determine the generated power in the actual condition. The capacity factor is defined as the percentage of the nominal power that the wind turbine generates in actual wind conditions. In this case, the energy efficiency of the wind turbine becomes

$$\eta(V) = C_{\mathrm{f}}(V), \tag{9.46}$$

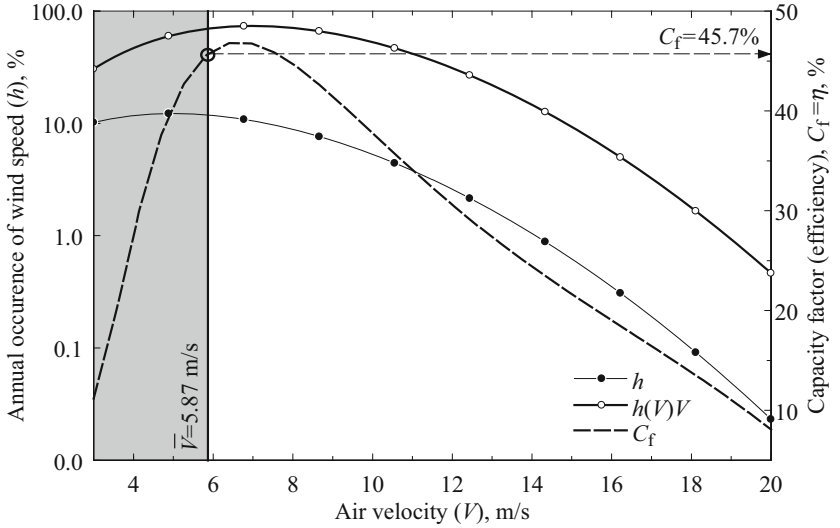

Fig. 9.39 Case study showing the capacity factor and annual wind speed occurrence probability as a function of air velocity

where $C_f(V)$ is the capacity factor expressed as a function of the actual wind velocity. The capacity factor is small at low and high velocities and has typically a maximum value at the design point.

Figure 9.39 exemplifies a typical variation of the wind capacity factor; on the same plot is superimposed an assumed annual occurrence of wind speed. It is possible to calculate the average wind velocity based on velocity occurrence, where in this case, the average velocity is defined as the velocity that occurs 100%; in other word the area between $h(V) \times V$ curve is equal to the gray area shown in the figure. Therefore,

$$\bar{V} = \int_{V_{ci}}^{V_{co}} h(V) V dV. \tag{9.47}$$

For the numerical example shown in the figure, the average wind velocity is $\bar{V} = 5.87$ m/s, which gives an average capacity factor of $C_f = 45.7\%$. In general, the average turbine efficiency is given by

$$\bar{\eta} = C_f(\bar{V}). \tag{9.48}$$

The average power generation of a wind turbine, placed in a certain location, becomes

$$\bar{W} = \frac{1}{2} \rho A C_f(\bar{V}) V_{RMC}^3. \tag{9.49}$$

Another effect, the wind chill, can influence some measures, as shown in Sahin et al. (2006), such as the efficiency of wind turbine generators. Faster cold wind makes the air feel colder than when wind is not present, because it removes heat from our bodies faster due to intensified heat transfer by convection. Wind chill is a measure of this effect and is defined as the hypothetical air temperature in calm conditions (air speed, $V = 0$) that would cause the same heat flux from the skin as occurs for the actual air speed and temperature. Wind chill temperature (see Sahin et al. 2006) can be estimated as

$$T_{\text{wch}} = 21.68 + 1.12T_0 - 38.58V^{0.16} + (0.83T_0 + 14.76)V^{0.16}, \tag{9.50}$$

where T is temperature in °C, the indices "wch" and "a" denote wind chill and surrounding air, and V is the wind speed in km/h.

Thus, a rigorous application of Eq. (9.49) implies the estimation of the air density at the wind chill temperature. The air density depends on the atmospheric pressure and temperature (a simple calculation of the air density can be based on the ideal gas law $\rho = \rho_{\text{ref}} \times T_{\text{ref}}/T_0 \times P_0/P_{\text{ref}}$, where the index 0 represents the actual environment, ref is the reference environment, T is the temperature in K, and P is the pressure. Due to expansion, air suffers additional cooling between upstream (1) and downstream (2) states. Thus the average air density is $\bar{\rho} = (\rho_1 + \rho_2)/2$, where $\rho_{1,2}$ are calculated with $(T_{1,2}, P_{1,2})$ and $T_{1,2}$ are the wind chill temperature calculated with Eq. (9.50). Thus, a more accurate energy efficiency expression accounting for wind chill temperature is

$$\bar{\eta} = C_{\text{f}}(\bar{V})\bar{\rho}/\rho_0, \tag{9.51}$$

where the index 0 indicates the surrounding temperature. Estimations by Sahin et al. (2006) for wind speeds in Ontario show that the energy conversion of wind energy can be up to 2% higher than the turbine capacity factor.

Using data representing the geographical and temporal distribution of velocity, air temperature, air pressure, and air humidity, it is possible to make accurate estimations of air density, wind chill temperature, average monthly or seasonal air velocities, and average seasonal root mean cube velocity. With these data, monthly or seasonal energy efficiency of wind energy conversion can be estimated at each geographic location. Sahin et al. (2006) provided monthly energy maps for Ontario. Two samples of these maps are shown in Fig. 9.40.

Since the average wind speed is below the cut-in wind speed in the month of January in Atikokan, the station energy efficiency is zero. At low wind speeds, efficiencies are high, but this does not mean that at these values the wind turbine is more efficient than rated for that wind speed. Rather, it means that the generated electricity is low and the potential of wind energy is low at these wind speeds. As a result, the ratio between generated electricity and potential energy is high. In July, the spatial distributions for energy efficiencies exhibit three clusters, and the general contour values are 40% to 50%.

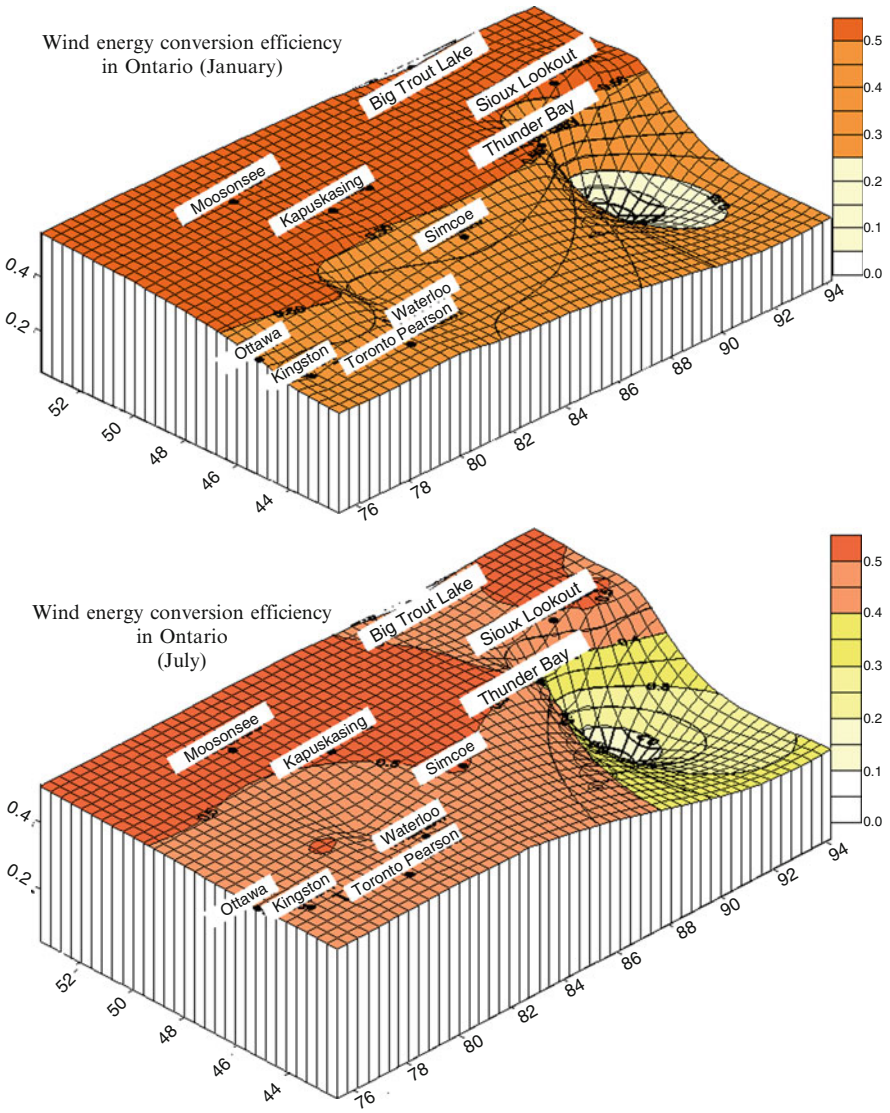

Fig. 9.40 Energy map for Ontario in January (longitude, latitude, and amplitude are on the axes) [modified from Sahin et al. (2006)]

9.3.1.3 Exergy Efficiency and Wind Exergy Maps

Exergy analysis is a useful tool for determining the thermodynamic limits and the irreversibilities of wind energy conversion. One important parameter affecting exergy analysis is the temperature of the surroundings. In the case of wind turbine, the wind chill temperature should be used as a reference state (see Sahin et al. 2006).

The exergy efficiency of a wind turbine is defined as the work produced per exergy associated with the wind. The work generated by the turbine can be calculated, as discussed above, as $W = 0.5C_f(\bar{V})\bar{\rho}AV^3_{RMC}$. The exergy associated with the wind surrounding the turbine must comprise the kinetic energy of the wind (which is a form of exergy) and the thermomechanic exergy of the wind. The thermomechanic exergy of the wind must be calculated with respect to wind chill temperature, because this is the temperature of the medium in the vicinity of the turbine. The wind has a higher exergy upstream (Ex_1) than downstream (Ex_2). Thus the exergy that enters the system is the difference ($Ex = Ex_1 - Ex_2$). Using appropriate expressions for thermomechanical and kinetic energy results in

$$\mathrm{Ex} = W + \bar{\rho}A\bar{V} \times \left\{ \bar{C}_p(T_1 - T_2) - T_0\left[\bar{C}_p \ln\left(\frac{T_2}{T_1}\right) - R \ln\left(\frac{P_2}{P_1}\right) - \bar{C}_p\left(1 - \frac{\bar{T}}{T_0}\right)\right]\right\}, \tag{9.52}$$

where $\bar{\rho}A\bar{V}$ is the mass flow rate of air, $T_{1,2}$ are the wind chill temperatures upstream and downstream of the turbine, T_0 is the temperature of the surroundings, $\bar{T}$ is the arithmetic mean of temperatures $T_{1,2}$, the pressures $P_{1,2}$ are at upstream and downstream, respectively, $\bar{C}_p$ is the specific heat, and R is the universal gas constant. The first term within the curly brackets represents the enthalpy difference, the second term is the entropy difference and the irreversibility due to heat transfer between the stream of air and the surroundings; basically, the expression between the curly brackets is the specific thermomechanical exergy consumed by the system. The exergy efficiency becomes

$$\psi = \frac{W}{Ex}. \tag{9.53}$$

Wind exergy maps were developed for Sahin et al. (2006) that correspond to the wind energy maps. These maps indicate the exergy efficiency of wind energy conversion temporally and geographically. The maps for January and July are reproduced in Fig. 9.41. The contours for exergy efficiency are seen to be lower than those for energy efficiency for all regions. The average exergy efficiency value is around 40%. In July, there is an area of high energy efficiency in northwest Ontario, but exergy analysis evaluates the lowest efficiencies in this area. The dominant efficiency in July is seen to be ~40%, except for the eastern regions of Ontario.

When comparing the results from Figs. 9.40 (energy efficiency) and 9.41 (exergy efficiency), large relative differences in energy efficiency values are observed, especially at low wind speeds. In contrast, the relative differences between energy and exergy efficiencies at high wind speeds are smaller. But these values are higher than 10% at all stations. These differences are large and should not be ignored in energy planning and management. However, for July the relative differences between the two types of efficiency are relatively low. Exergy efficiencies are lower than energy efficiencies for each station for every month considered.

Recall that the energy and exergy maps show the maximum conversion efficiency at specific geographic locations. This information is useful in selecting the wind

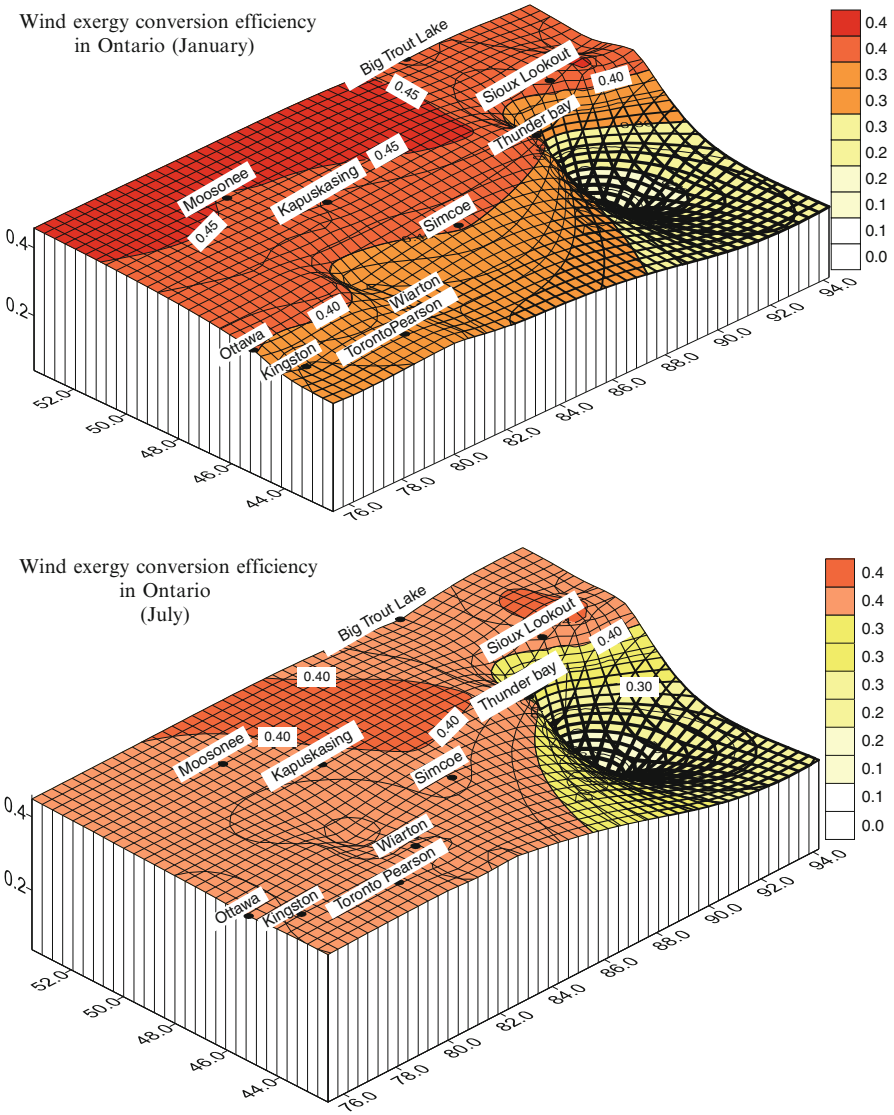

Fig. 9.41 Exergy map for Ontario in January (longitude, latitude, and amplitude are on the axes) [modified from Sahin et al. (2006)]

farm sites. However, lower efficiencies are obtained in practice due to additional losses of the actual systems.

9.3.2 Types of Wind Turbines

Basically there are two categories of wind turbine design: horizontal axis wind turbines (HAWT) and vertical axis wind turbines (VAWT). The horizontal axis wind turbines have emerged as the dominant technology. They place the rotor axis

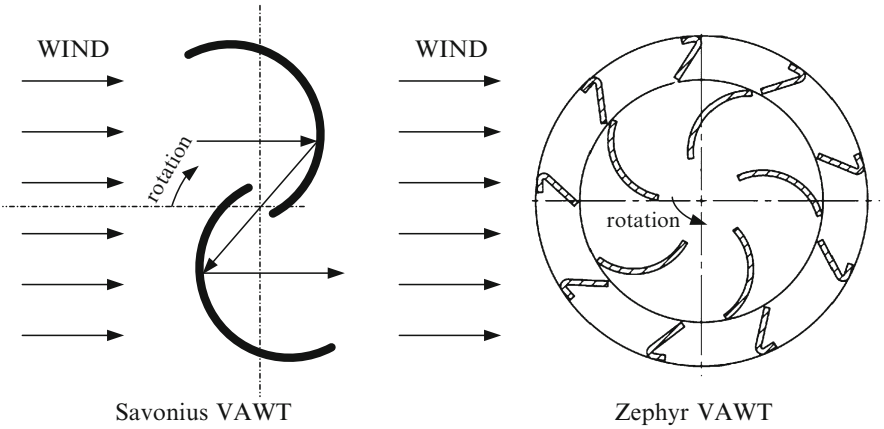

Fig. 9.42 Operating principles of the Savonius and Zephyr wind turbines

horizontal and in line with the wind direction. The common designs have the generator and the blade fixed on a rotating structure at the top of a tower. The mechanical system also comprises a gear box that multiplies the rotation of the blades. The HAWT achieves higher efficiency than the VAWT, but the VAWT operates well in fluctuating wind amplitudes provided that its direction remains quasi-constant.

One important feature of the VAWT is that it does not need to be pointed in the direction of the wind. Thus VAWT installation is appropriate where the wind changes direction very frequently. Another feature of VAWT is that it allows placing the generator and gear box lower, close to the support system of the turbine.

The HAWT construction can differ in the number of blades (generally two or three blades are used). The HAWT uses airfoils to generate lift under the wind action and rotate the propeller. The operation of some VAWT designs is based also on the aerodynamic lift principle, but there are designs that use form drag and aerodynamic friction to operate. Drag-type turbines are designed such that the form drag generates a torque; a typical drag turbine is the Savonius, used mostly in rural areas. The operating principle of the Savonius wind turbine is illustrated schematically in Fig. 9.42. The generated torque is due to the difference in pressure between the concave and convex surfaces of the blades and by reaction forces of the deflected wind coming from behind the convex surface. The efficiency of Savonius turbine is over 30%.

A more elaborated design of the VAWT, the Zephyr, is presented also in Fig. 9.42. It is designed to perform well in low wind speeds and high turbulence conditions. For this reason, several Zephyr wind turbines can be installed close to each other to form a compact wind farm. The power coefficient of the Zephyr wind turbine is rather low (0.11), but the turbine has a good utilization factor, a low cut-in speed, and a high cut-off speed, which make it competitive in urban areas. This kind of turbine was developed at the University of Ontario Institute of Technology; see Pope et al. (2010).

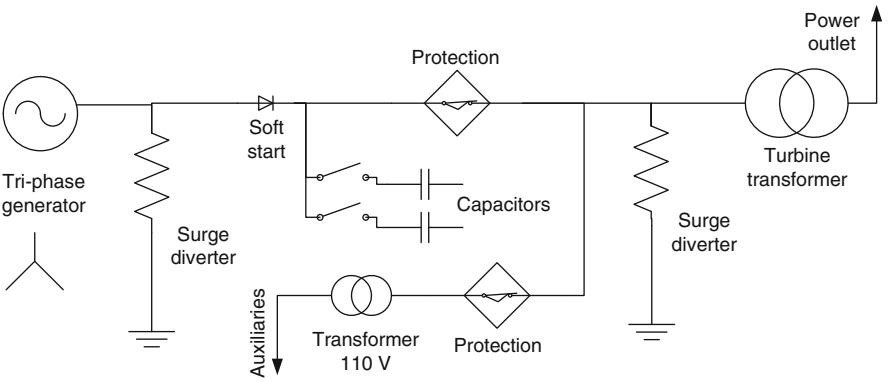

Fig. 9.43 Simplified electric diagram of a wind power generation unit

Common models of lifting VAWT turbines are the triangular (delta) Darrieus turbine, the Giromill turbine, and the Darrieus–Troposkien turbine. The triangular Darrieus turbine has straight blade geometry. The Giromill turbine is a low-load system with straight, vertical blades with an adjustable angle of attack to fit the best working conditions. The Darrieus–Troposkien turbine is the most used turbine for electric power generation. The blades of this turbine are airfoils assuming a Troposkien shape (which is a name derived from Greek meaning "the shape of a spinning rope"). Basically, the airfoil is a flexible blade connected in the vertical axis at two points (lower and upper) and while rotating approximates by revolution the shape of an ellipsoid. The blades can be made from light materials such as aluminum, fiberglass, steel, or wood.

9.3.3 Wind Power Plants

Apart from the wind turbine itself, wind power plants comprise several other important subsystems such as yaw control, speed multiplier (gear box), voltage-frequency and rotation controllers, voltage raising and lowering transformers (having the role of matching the generation, transmission, and distribution voltages at normal consumption levels), and protection systems for overcurrent, overspeed, overvoltage, atmospheric outbreaks, and other anomalous forms of operation. All these subsystems are sustained by a robust mechanical structure.

Figure 9.43 illustrates a simplified electric diagram of a wind power generation unit, its main components, and their functions. The system is equipped with general protection circuits, breakers, and overcurrent and reverse current protection. When a wind power generator is connected to the grid, it is possible that, during a low wind period, the generated voltage is lower than the grid voltage. If this situation occurs, the protection systems (see the figure) temporarily disconnect the system from the grid. Also if there is an overcurrent caused by too large a load, then the

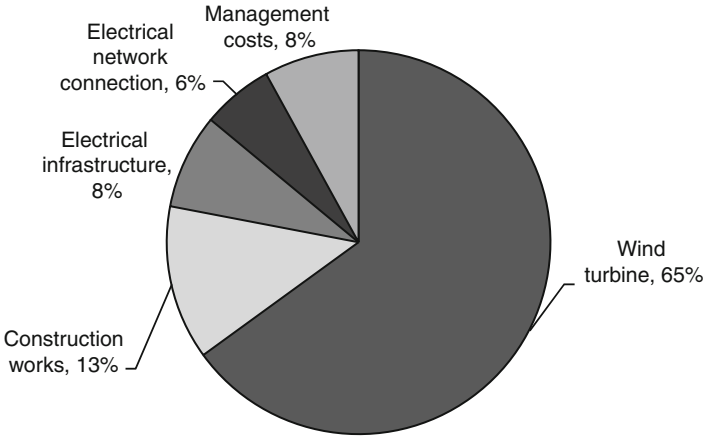

Fig. 9.44 Breakdown of costs for a typical 10-MW power plant [modified from Burton et al. (2001)]

thermal protection will disconnect the generator. The capacitors are used to correct the power factor of the generator and allow a soft start. The capacitors work together with a thyristor unit to soften the starting process of the generator. A small transformer is used to supply the auxiliary equipments. The system has a main transformer that allows connection of the unit to the grid. Local energy storage can be applied in batteries case in which the system will include an inverter. Moreover, it is possible to couple several turbines to the main transformer, when it applies, rather than equipping each turbine with its own grid connection transformer.

The electrical system and electrical infrastructure of a wind power plan may account for 13% to 15% of the total installation costs. A breakdown of various costs for installing a 10-MW wind power unit is shown in Fig. 9.44. The electrical infrastructure is costly because it involves extensive work for grounding and lightning protection. The damage produced by lightning to the wind farms and individual units is considerable. In Germany, statistics show that lightning produces damage annually to 8% of the installed wind turbines, while in Sweden this is 6% and in Denmark 4% (see Burton et al. 2001).

The noise generated by wind power plants is also a major concern. The blades, the gearbox, the generator, the generator hub, the tower, and the auxiliary system all generate significant amounts of noise during operation. The noise of a wind power plant operating 350 m away can be 10% higher than the typical rural night time background noise.

Considerable efforts were deployed in recent years to develop techniques for reducing noise from wind turbines by improving their design and installation. With the current technology, the noise level of the main power plant components ranges from 40 to 98 dB(A). Nevertheless, protection against noise increases the capital cost of the power plant. By the year 2004, the investment cost was around 50 cents per installed watt and 6 cents per generated kWh.

By expanding the wind power generation capacities in recent years, the cost of installed kW and the cost of generated kWh were reduced significantly. The investment cost is presently about 30% higher than that of natural gas power plants, while the generation cost is about 3.5 cents/kWh.

9.3.4 Hydrogen Production from Wind Electricity

Production of hydrogen by water electrolysis driven by wind-generated electricity is viewed as one promising method for promoting sustainable energy systems. The technology is mature, though the capital costs need to be reduced. Although wind energy can be considered a nonpolluting resource (renewable), the quantity of construction materials consumed per unit of hydrogen produced with wind electricity can be much higher than that for the more traditional approach of hydrogen production from natural gas.

Taking into account greenhouse gas (GHG) emissions from the construction and operation stages of wind-to-hydrogen generation plants, and their lifetimes and capacities, the indirect GHG emissions per unit of produced energy can be calculated and compared with figures specific to conventional systems. The conventional systems are characterized by significant pollution during operation, while wind-to-hydrogen systems have embedded emissions in the construction materials. A life cycle study by Granovskii et al. (2006) indicates that hydrogen obtained from natural gas reforming (including hydrogen compression to 350 bar) leads to life cycle emissions of 86 g CO_2 per MJ of energy with respect to the produced hydrogen HHV (higher heating value). In the case of using wind power, the amount of carbon dioxide for whole lifecycle is estimated to be 8 g CO_2 per MJ (including wind-electrically-driven compression of H_2 to 350 bar).

Hydrogen production from wind energy is also discussed in Chapter 13.

9.4 Geothermal Energy

Geothermal energy is a form of thermal energy that is available in some regions of the earth's surface at temperature levels in the range of about 35° to 500°C, even though most of the geothermal places provide temperature levels up to 250°C. Geothermal heat is used either for process heating or is converted into electricity through appropriate heat engines. A large palette of heat-consuming processes can be supplied by geothermal energy including space and water-heating applications, industrial processes, supplying various procedures in agriculture and food industry, and so on. Figure 9.45 illustrates the global utilization of geothermal heat.

It can be observed from the graph that most of the geothermal applications are the ground source heat pump systems. In recent years, there has been substantial development in geothermal energy, in which there is interest in a ground source

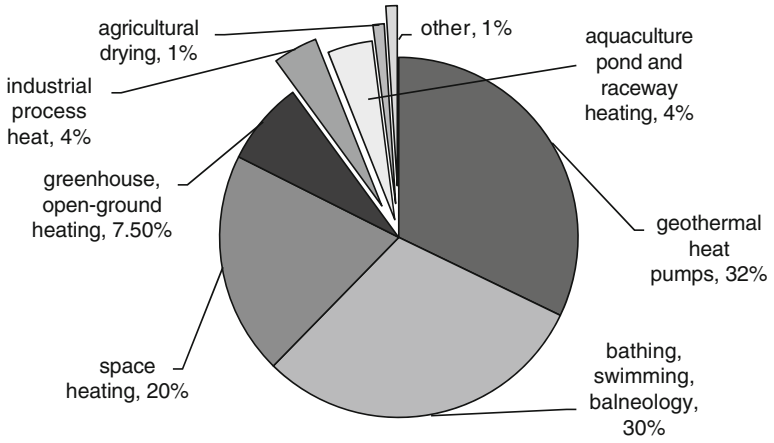

Fig. 9.45 Global utilization of geothermal energy for heating applications [data from Lund (2005)]

Table 9.7 Some historical milestones in geothermal development in Canada

Date	Milestone
1886	In Banff, Alberta, hot springs were piped to hotels and spas.
1975	Drilling to assess high-temperature geothermal resources for electricity generation in British Columbia.
1976–1986	Ten-year federal research program assesses geothermal energy resources, technologies, and opportunities for Canada.
1990	Hydro Ontario funds a program to install geothermal heat pumps in 6,749 residences.
1990s	Government take a greater interest in using renewable energy, including geothermal, as a way to decrease greenhouse gases and other emissions.
2004	Western GeoPower Corp. applies for government approval to build a $340 million, 100-MW geothermal power plant at Meager Creek, northwest of Whistler, British Columbia.
	Manitoba announces program to provide loans of $15,000 toward installation of geothermal heat pump systems.

heat pump, hydrogen production from geothermal energy, and installing electrical plants supplied by geothermal heat. Some historical milestones regarding geothermal development in Canada are listed in Table 9.7.

9.4.1 Thermodynamic Limits of Geothermal Energy Conversion

Because it is a source of heat, the limit of geothermal energy conversion is governed by the Carnot factor. Thus, it is important to assess the range of the Carnot factor for geothermal reservoirs. Additionally, it is useful to analyze relevant irreversibilities specific to geothermal energy conversion. Thus, one can obtain a general picture of the thermodynamic limits of geothermal energy conversion into work.

We will analyze, as a first step, the temperature level of the geothermal sources and the nature of the geothermal fluid. The average increase in temperature with depth, called the geothermal gradient, is about 0.03°C/m, that is, 30°C/km for a few kilometers near the earth's surface. Values as low as about 10°C/km are found in the ancient continental crust, and very high values (>100°C/km) are found in areas of active volcanism. Heat from the earth's depths is transported to the surface in three possible ways that characterize the type of geothermal field: hot water, wet steam, and dry steam. Hot water fields contain reservoirs of water with temperatures between 60° and 100°C, and are most suitable for space heating and agricultural applications. For hot water fields to be commercially viable, they must contain a large amount of water with a temperature of at least 60°C and lie within 2,000 m of the surface. Wet steam fields contain water under pressure and usually measure 100°C. These are the most common commercially exploitable fields. When the water is brought to the surface, some of the water flashes into steam, and the steam can drive turbines that produce electrical power. Dry steam fields are geologically similar to wet steam fields, except that superheated steam is extracted from the aquifer. Dry steam fields are relatively uncommon. Because superheated water explosively transforms into steam when exposed to the atmosphere, it is much safer and generally more economical to use geothermal energy to generate electricity, which is much more easily transported. The geothermal reservoirs can be categorized into three kinds according to the temperature level (Fig. 9.46).

Not only is the temperature level important when estimating the geothermal energy conversion, but also the pressure of the geothermal fluid. The exergy of a geothermal fluid (brine, steam, etc.), can be calculated based on specific thermo-mechanical exergy according to

$$\mathrm{ex} = h(T,P) - h_0 - T_0[s(T,P) - s_0], \tag{9.54}$$

where T, P represent the temperature and the pressure at which the geothermal fluid is made available to the energy conversion system (power generator). The enthalpy part shown in Eq. (9.54) represents the energy content of the stream, $e = h(T,P) - h_0$. Index 0 denotes the reference state. Thus the energy and exergy efficiencies of the geothermal generator can be expressed by

$$\left.\begin{aligned} \eta &= \frac{\dot{W}}{\dot{m} \times e} \\ \psi &= \frac{\dot{W}}{\dot{m} \times ex} \end{aligned}\right\}, \tag{9.55}$$

where $\dot{W}$ represents the generated work rate and $\dot{m}$ is the mass flow rate of the geothermal fluid.

In order to obtain an estimate of the conversion limit, one has to consider an ideal thermodynamic cycle to which the geothermal energy is transferred to generate work. Since the geothermal fluid is generally brine, it appears logical to assume that during the heat transfer process the brine exchanges sensible heat. Thus the temperature of the brine decreases to T_0.

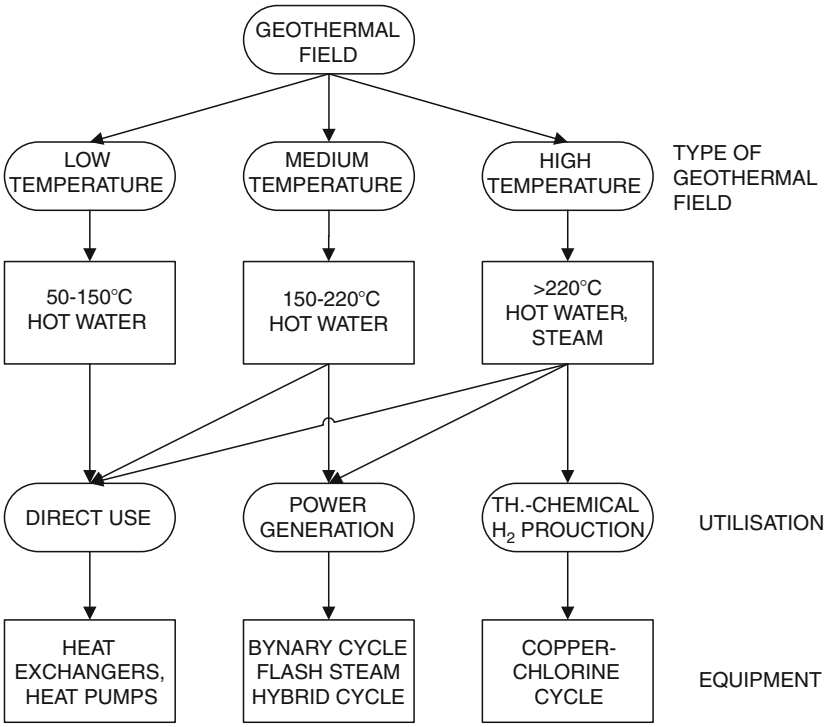

Fig. 9.46 Classification of geothermal fields and utilization of geothermal energy

Figure 9.47 suggests a thermodynamic cycle where the geothermal fluid delivers sensible heat within a cooling process through which it reaches equilibrium with the environment at (T_0, P_0). We assume the process as a straight line Ts in the diagram. The thermodynamic cycle that generates maximum work is in this case triangle shaped; the maximum generated work is indicated with the triangular gray area. The efficiency is $\eta = (T - T_0)/(T + T_0)$. In Table 9.8, figures for maximum conversion efficiency from low-, medium-, and high-temperature geothermal sources when sensible heat is extracted from the geothermal fluid are given. Note that in some cases the geothermal fluid is steam. One can assume in such cases that steam is condensed through an isothermal process, after which the entropy reaches s_0. This process is followed by an isentropic expansion to (T_0, P_0). This is an idealization; such processes cannot occur in an actual system, but it is informative to know the conversion efficiency in this case (which is the upper bound). Since this is a Carnot cycle, the efficiency is $\eta = (T - T_0)/T$; this efficiency is also reported in the table.

This analysis shows that the efficiency of geothermal energy conversion system must be much lower than 17% to 44% due to irreversibilities. Note that the energy efficiency of geothermal steam plants ranges from 10% to 17%. The energy efficiency of binary cycle plants ranges from 2.8% to 5.5%. These percentages are lower than in the case of steam power plants because binary plants are typically used for lower-temperature geothermal resources.

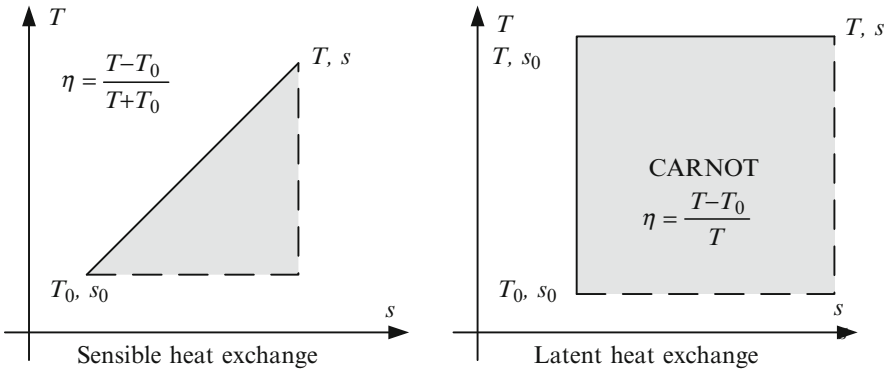

Fig. 9.47 Thermodynamic cycles for maximum work extraction from geothermal energy

Table 9.8 Thermodynamic limits of geothermal energy conversion

Geothermal source	Temperature (°C)	Sensible heat exchange (%)	Latent heat exchange (%)
Low temperature	150	17	29
Medium temperature	220	24	39
High temperature	500	44	61

The quality of a geothermal reservoir can be appreciated in terms of the exergy content of the brine. In this respect, Lee (2001) introduced the so-called specific exergy index (SExI):

$$\mathrm{SExI} = \frac{h_{\mathrm{brine}} - 273.16 s_{\mathrm{brine}}}{1{,}192}, \tag{9.56}$$

which is a straight line on an *h*-*s* plot of the Mollier diagram. Straight lines of SExI = 0.5 and SExI = 0.05 therefore can be drawn in this diagram and used as a map for classifying geothermal resources by taking into account the following criteria:

- SExI < 0.05 for low-quality geothermal resources
- $0.05 \leq$ SExI < 0.5 for medium-quality geothermal resources
- SExI ≥ 0.5 for high-quality geothermal resources

Here, the demarcation limits for these indexes are exergies of saturated water and dry saturated steam at 1 bar absolute.

9.4.2 Geothermal Power Plants

Many thermodynamic cycles were developed for geothermal power generation. The selection of the cycle depends on the kind of geothermal fluid, its flow rate, and the level of temperature. The possible geothermal fluid can be dry steam,

low-pressure brine, or high-pressure brine. The geothermal reservoir may or may not require reinjection of the fluid after its use in the power plant. The power plant design must be such that it extracts as much exergy as possible from the geothermal fluid. Figure 9.48 presents a classification of geothermal power plants.

When geothermal heat is available in the form of dry steam, then it can be converted into work by steam turbines. There are two methods: steam is created after expansion and it is condensed and reinjected into the geothermal well, or steam is simply released into the atmosphere. Figure 9.49 presents power plants diagrams with dry steam expansion and with or without reinjection.

Some geothermal reservoirs eject steam at high or lower pressure, which can be expanded in a turbine to generate power. Depending on the type of geothermal well, reinjection of the geothermal fluid may or may not be needed.

For example, if a geothermal site generates dry steam, a turbine can be used to generate power as indicated in Fig. 9.49. In the case when the steam pressure is considered low, or if there is no need to recycle the geothermal fluid, then after expansion down to atmospheric pressure, the steam can be released to the atmosphere (Fig. 9.49a). However, if the steam pressure and temperature are high enough, the amount of power generated allows for driving a recirculation pump and still generating a satisfactory yield by the turbine. In this case (Fig. 4.49b) the steam can be expanded in a vacuum, condensed, and the produced water pressurized in a pumping station and reinjected. Note that the reinjection pressure must be very high—a couple hundred bar. The reinjection is needed in many instances to keep the geothermal resources at steady production. If the geothermal reservoir is a hot rocky layer, then the water injected through one well is boiled, and it is extracted as steam through another well.

Geothermal sources generating low-pressure steam that needs to be reinjected can be coupled to an organic Rankine cycle (ORC) generator as shown in Fig. 9.50. These cycles are also known as binary cycles because sometimes they operate with binary mixtures of refrigerants (e.g., ammonia–water). The dry steam extracted from the geothermal well at point 9 is condensed (9–10) and subcooled (10–11) before water is reinjected at point 12. The heat released by the geothermal brine is then transmitted to a working fluid (toluene in the exemplary case). The working fluid is boiled and expanded as saturated toluene vapors at point 1. After expansion, internal heat is recovered in the heat exchanger (2–3/5–6), and then condensation (3–4), pressurization of the saturated liquid (4–5), preheating (5–6 and 6–7), and boiling (7–1) take place.

The calculation procedure of the cycle is presented in Table 9.9 based on EES (engineering equation solver) code, which includes all equations (energy and mass balance) needed to solve the problem and the calculated state parameters in Table 9.10. The energy and exergy efficiencies are calculated by

$$\left.\begin{aligned}\eta &= \frac{(h_1 - h_2) - (h_5 - h_4) - (h_{12} - h_{11})}{h_1 - h_6}\\ \psi &= \frac{(h_1 - h_2) - (h_5 - h_4) - (h_{12} - h_{11})}{h_9 - h_{11} - T_0(s_9 - s_{11})}\end{aligned}\right\}. \tag{9.57}$$

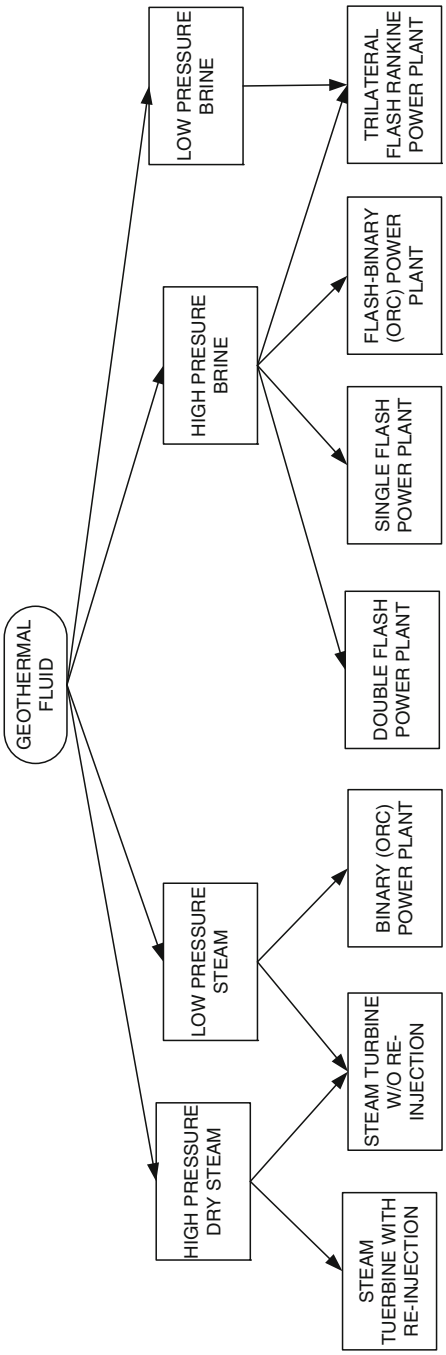

Fig. 9.48 Geothermal power plants categorized based on the kind of geothermal fluid. ORC, organic Rankine cyc

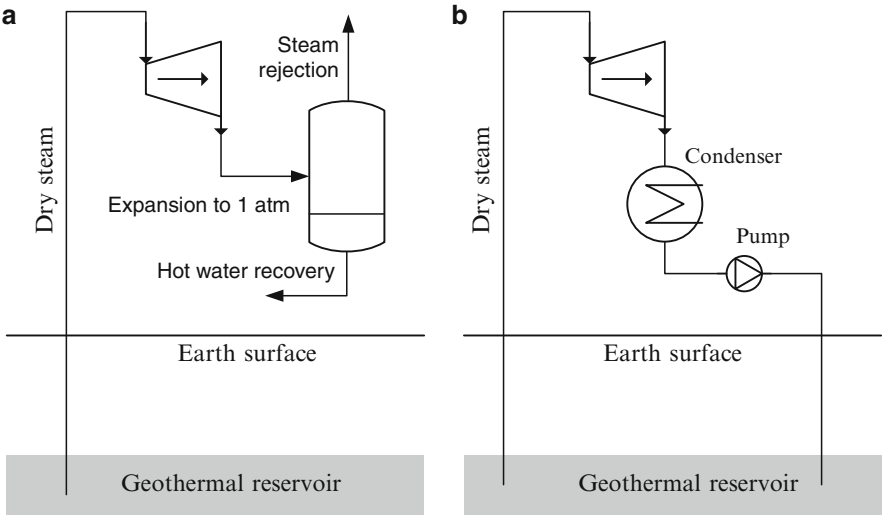

Fig. 9.49 Dry power plants with direct expansion

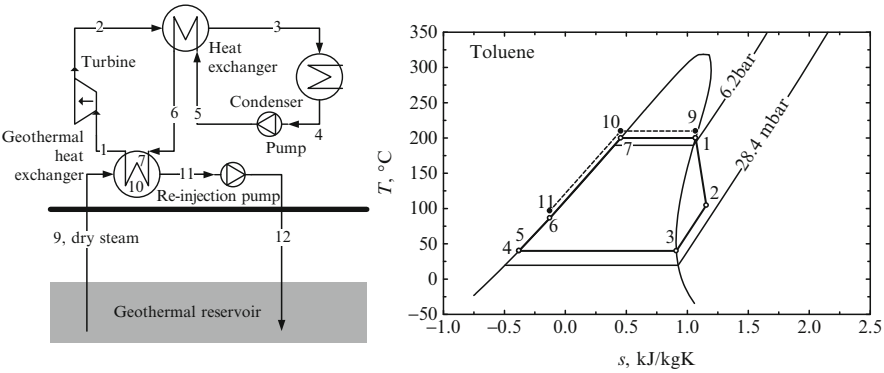

Fig. 9.50 Geothermal binary cycle power plant driven by dry steam

The energy efficiency of this cycle is 24%, the exergy efficiency is 15%, and the Carnot efficiency, calculated with the maximum temperature of the geothermal brine, is 38%.

If the pressure of the geothermal brine is high enough, then steam-flash power plant cycles can be an effective solution for power generation. Figure 9.51 presents two types of flash power plants, namely single flash and double flash. In these systems, the high-pressure geothermal brine is flashed at an intermediate pressure through an isenthalpic process (1–2). Thus, saturated vapors flash from the liquid and they are directed toward the turbine. There they are expanded to low pressure and then condensed using the ambient air as a heat sink. After condensation, the resulting water is reinjected into the well. Note also that the steam resulting from

Table 9.9 Energy and mass balance equations for modeling the system from Fig. 9.50

State	Equations	State	Equations
1	$T[1] = 200$; $x[1] = 1$ $s[1] = s$(Toluene, $T[1]$, $x[1]$) $P[1] = P$(Toluene, $T[1]$, $x[1]$) $h[1] = h$(Toluene, $T[1]$, $x[1]$)	6	$h[2] - h[3] = h[6] - h[5]$ $P[6] = P[1]$ $T[6] = T$(Toluene, $P[6]$, $h[6]$) $s[6] = s$(Toluene, $P[6]$, $h[6]$)
2	$s_{2s} = s[1]$; $P[2] = P[3]$;$\eta_T = 0.8$ $h_{2s} = h$(Toluene, $P[2]$, s_{2s}) $\eta_T \times (h[1] - h2s) = h[1] - h[2]$ $T[2] = T$(Toluene, $P[2]$, $h[2]$) $s[2] = s$(Toluene, $P[2]$, $h[2]$)	7	$h[7] = h$(Toluene, $P[7]$, $x[7]$) $P[7] = P[1]$; $x[7] = 0$; $T[7] = T[1]$ $s[7] = s$(Toluene, $T[7]$, $x[7]$)
3	$T[3] = 40$; $x[3] = 1$ $P[3] = P$(Toluene, $T[3]$, $x[3]$) $h[3] = h$(Toluene, $T[3]$, $x[3]$) $s[3] = s$(Toluene, $T[3]$, $x[3]$)	9	$T[9] = T[1] + 10$; $x[9] = 1$ $P[9] = P$(Steam, T[9], $x[9]$) $h[9] = h$(Steam, T[9], $x[9]$) $s[9] = s$(Steam, T[9], $x[9]$)
4	$T[4] = T[3]$; $x[4] = 0$; $P[4] = P[3]$ $h[4] = h$(Toluene, $T[4]$, $x[4]$) $s[4] = s$(Toluene, $T[4]$,$x[4]$)	10	$T[10] = T[9]$; $x[10] = 0$ $P[10] = P$(Steam, $T[10]$, $x[10]$) $h[10] = h$(Steam, $T[10]$, $x[10]$) $s[10] = s$(Steam, $T[10]$, $x[10]$)
5	$P[5] = P[1]$; $s_{5s} = s[4]$; $\eta_P = 0.9$ $h_{5s} =$ enthalpy (Toluene, $P = P[5]$, $s = s_{5s}$) $\eta_P \times (h[5] - h[4]) = h_{5s} - h[4]$ $T[5] = T$(Toluene, $P[5]$, $h[5]$) $s[5] = s$(Toluene, $P[5]$, $h[5]$)	11	$T[11] = T[6] + 10$; $P[11] = P[10]$ $h[11] = h$(Steam, $T[11]$, $P[11]$) $s[11] = s$(Steam, $T[11]$, P[11]) $\dot{m}_w \times (h[9] - h[11]) = h[1] - h[6]$

h enthalpy; P pressure; s entropy; T temperature; x quality
$\eta_{T,P}$ = efficiency (turbine, pump); $\dot{m}_w$ = water mass flow rate

Table 9.10 Calculated results for the system from Fig. 9.50

State	s (kJ/kg K)	T (°C)	P (bar)	h (kJ/kg)
1	1.068	200	7.475	485.7
2	1.156	104.6	0.07907	356.7
3	0.9104	40	0.07907	271.8
4	−0.3799	40	0.07907	−132.3
5	−0.3796	40.23	7.475	−131.4
6	−0.1271	86.65	7.475	−46.42
7	0.4545	200	7.475	195.5
9	6.357	210	19.06	2,798
10	2.425	210	19.06	897.7
11	1.267	96.65	19.06	406.3

flashing can be used for processes other than power generation. For instance, it can be used to produce refrigeration using ejectors in a refrigeration cycle. The double-flash cycle can be applied if the moisture content of the expanded steam is too high; this is done by expanding in two stages.

Another effective option for geothermal fields that generate high-pressure brine is the flash-binary power plant. This kind of power plant couples a flash cycle that operates with the geothermal brine as the working fluid with a bottoming organic Rankine cycle as illustrated in Fig. 9.52. After the flashing process the steam is

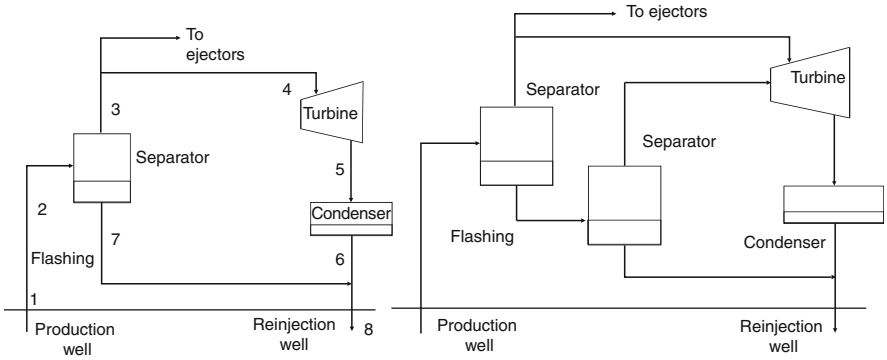

(a) Single flash power plant (b) Double flash power plant

Fig. 9.51 Types of steam-flash power plants: (**a**) single flash and (**b**) double flash

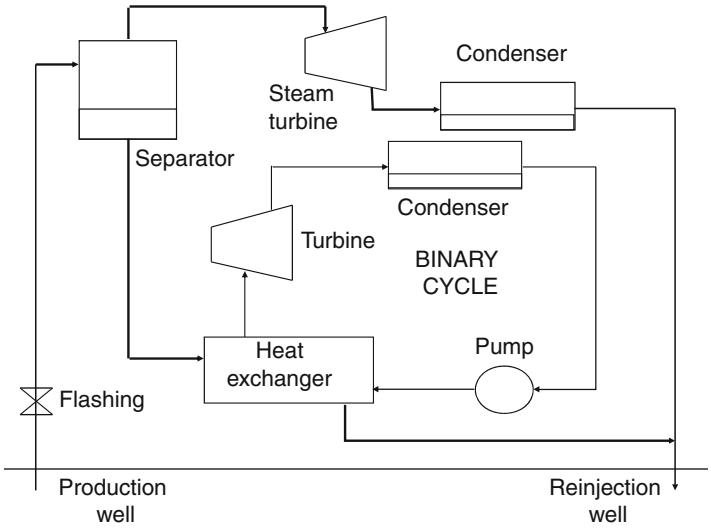

Fig. 9.52 Flash–binary power plant

expanded in a turbine, while the resulted liquid is passed through a heat exchanger that preheats and boils the working fluid of the bottoming cycle. The system will have two independent condensers. It is important to match the temperature profiles in the heat exchanger so that the available exergy could be exploited to a maximum for the benefit of an improved system performance.

Let us compare the temperature profiles in the boiler of a steam power plant with those of a binary plant operating with ammonia–water. The geothermal brine comes at the same temperature and flow rate in both cases. As observed in Fig. 9.53a, due to the necessity of having a pinch point at A, much of the flue gas exergy is wasted since it is exhausted at a rather high temperature.

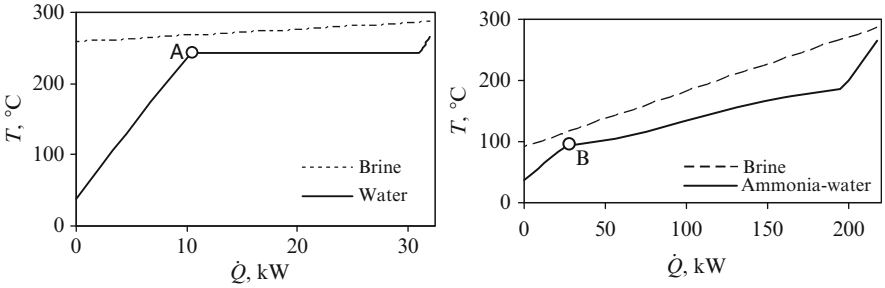

Fig. 9.53 (**a**) Temperature profiles in boiler for steam cycles and (**b**) ammonia–water cycle

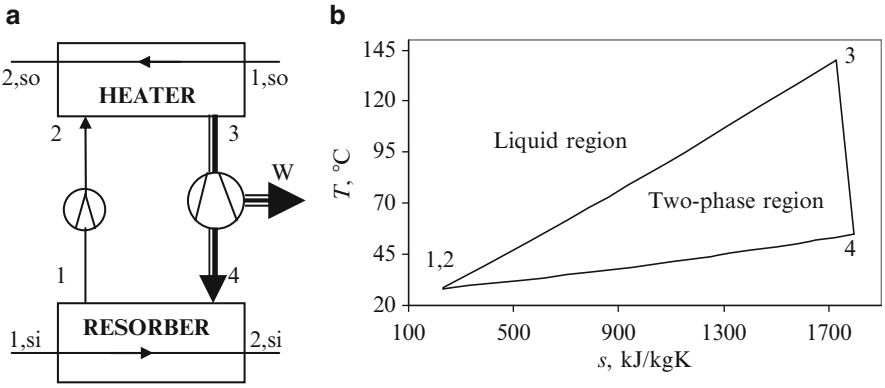

Fig. 9.54 Ammonia–water trilateral flash Rankine cycle: (**a**) the system diagram; (**b**) the thermodynamic cycle [modified from Zamfirescu and Dincer (2008b)]

If we consider the heat recovery from the same source but this time using an ammonia–water mixture with 70% ammonia concentration instead of water, the calculated temperature profiles look like the ones presented in Fig. 9.53b. The same pinch point temperature of 25°C has been considered in the two cases. The pinch point is denoted "B" in the second case.

As it can be seen from the comparative analysis of Fig. 9.53a,b, more of the brine exergy is used in the second case because the brine leaves the heat exchanger at a lower temperature. Therefore, the produced vapors in the second case have much higher enthalpy to be converted into work for power generation purposes.

Figure 9.54 illustrates another cycle that is shown to be effective for geothermal power generation when the geothermal well produces hot brine (indicated on the figure with "so", source). The cycle operates with ammonia water and comprises four elements corresponding to four processes, namely a pump, two heat exchangers (resorber and liquid heater), and an expander. In the state denoted with #1, there is a saturated ammonia water solution in liquid phase. This solution is pumped at high pressure, and it results in a subcooled liquid at #2. The liquid is then heated using the heat source stream up to the moment when it reaches the saturation in state #3.

Table 9.11 Performance comparison of geothermal power plants for 150°C brine temperature

	ORC cycles				NH_3–H_2O cycles	
Parameter	R141b	R123	R245ca	R21	Kalina	TFC
η (%)	10	9	9	9	3	8
ψ (%)	13	16	16	13	13	30

Data from Zamfirescu and Dincer (2008b)

The saturated liquid is flashed (expanded) in the volumetric expander that produces work at its shaft and a liquid–vapor mixture at its outlet, in state #4. In the resorber, cooling is applied to the two-phase mixture using the heat sink stream (indicated on the figure with "si", sink). As a consequence, a combined process of condensation and absorption occurs that eventually results in releasing a saturated liquid in state #1. Another implementation of the ammonia–water Rankine cycle is the Kalina cycle, where the ammonia–water mixture is heated in three phases: initially the subcooled liquid is preheated up to the pinch point where it becomes saturated, the fluid is then boiled and its temperature further increases, and in the last phase the vapors are superheated. The superheated vapors are expanded in a turbine and then condensed in a so-called distillation and condensation subsystem. This subsystem includes an absorber, a vapor–liquid separator, and a condenser.

Several thermodynamic cycles are compared in Table 9.11 in terms of energy and exergy efficiency assuming that the brine inlet temperature is 150°C. It can be noted that the trilateral flash Rankine cycle shows the best exergy efficiency, which is about two times higher than that of other options, which means that this cycle better recovers the exergy of the geothermal brine.

9.4.3 Thermal Applications

Geothermal energy is commonly used for a number of thermal applications such as ground source heat pumps and process heating. The domestic hot water requirement is one important parameter for the summer season. It increases on hot days when the demand for air conditioning is also high. Because of the increase in the domestic hot water requirement, pump energy consumption in total energy input increases. During the winter there is a need for space heating. Thus, a ground source heat pump can use the earth as either the source or the sink to operate both during winter and summer and to produce, as a function of the process, air conditioning, hot water, and space heating.

Basically, during the summer a ground–air heat exchanger can be used to generate air conditioning. In this case, a heat transfer fluid (water) is circulated through tubes embedded in the earth and water is cooled to a temperature of 4° to 10°C. Cold water is passed through a heat exchanger to cool the air and generate an air conditioning effect. Ground tube heat exchangers can be used for various process cooling applications. An example is cooling of electronics in shelters as studied in Vargas et al. (2005) where air is circulated directly through tubes buried in the ground that operate as a heat sink exchanger.

The ground can play the role of heat source for a heat pump that is used either for hot water or for space heating or process heating. In this case, the evaporation of the working fluid occurs at the temperature of the earth at the level of the buried heat exchanger. The thermodynamic cycle can be the typical vapor compression one. The condenser of the heat pump ejects useful heat at a temperature level convenient for space or water heating. Some other processes such as drying also can be driven with geothermal heat pumps.

9.4.4 Geothermal-Based Hydrogen Production

Geothermal energy appears to be an attractive renewable energy option for the production of hydrogen. In countries with abundant geothermal sources, certainly geothermal-based hydrogen production may become a major potential. It is the natural heat of the earth that is present in the earth's core, mantle, and crust. Also, an environmentally advantageous energy source that produces far less air pollution than fossil-fuel sources and the life of a geothermal resource may be prolonged by reinjecting the waste fluid, which is the most common method of disposal.

Although only approximately 200° to 250°C of thermal input in the hydrogen production process coupled with a geothermal source is possible today, this may change within the next decades. One should note that the technologies of hydrogen production and utilization can easily be integrated with geothermal sources and stand-alone energy systems. Using geothermal resources to produce the hydrogen would reduce the costs even further.

Geothermal-based hydrogen production offers potential advantages over other sources for a growing hydrogen economy. These advantages do not ensure that geothermal-based hydrogen will be the only option, but it will compete with other hydrogen production options. In some countries, geothermal energy is considered a primary energy source of producing hydrogen since it provides reliable energy supply in an environmentally benign manner.

Remarkable research efforts are being deployed to develop hydrogen production methods from geothermal energy. In Chapter 13, the most relevant of these are analyzed in detail.

9.4.5 District Energy

District heating and electricity can be supplied from geothermal energy. It makes sense to generate electricity from geothermal heat, using heat engines, and the heat ejected by the heat engine is further used for space heating or producing hot water, though most of the district applications using geothermal energy are for heating.

Here we present a case study analysis of the Salihli Geothermal District Heating System (SGDHS), which has a maximal yield of 87 L/s at an average reservoir

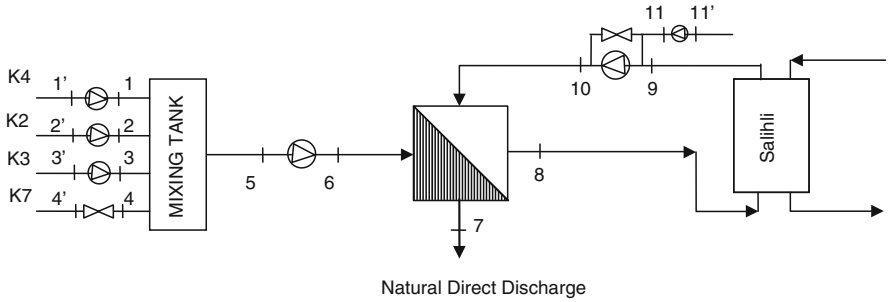

Fig. 9.55 Salihli Geothermal District Heating System [modified from Özgener et al. (2005)]

temperature of 95°C, with a minimal capacity of 838 MW (Özgener et al. 2005). The SGDHS was originally designed for about 20,000 residences. Of these, 2,400 residences are heated by geothermal energy as of February 2004. The outdoor and indoor design temperatures for the system are 4°C and 22°C, respectively.

Figure 9.55 illustrates a schematic of the SGDHS where two hospitals and office buildings heated by geothermal energy were also included. The SGDHS consists mainly of three cycles: (a) energy production cycle (geothermal well loop and geothermal heating center loop), (b) energy distribution cycle (district heating distribution network), and (c) energy consumption cycle (building substations). At the beginning of 2004, there were seven wells ranging in depth from 70 to 262 m in the SGDHS. Of these, five wells were in operation at the date studied and two wells (K5 and K6) were out of operation. Four wells (designated as K2, K3, K4, and K7) and one well (K1) are production and balneology wells, respectively.

The well head temperatures of the production wells vary from 56° to 115°C, while the volumetric flow rates of the wells range from 2 to 20 L/s. The geothermal fluid is basically sent to two primary plate–type heat exchangers and is cooled to about 45°C, as its heat is transferred to secondary fluid. The geothermal fluid (point 7) is discharged via natural direct discharge, with no recharge to Salihli geothermal field production, but reinjection studies are expected to be completed in the near future. The temperatures obtained during the operation of the SGDHS are, on average, 98°C/45°C for the district heating distribution network and 62°C/42°C for the building circuit.

By using the control valves for flow rate and temperature at the building's main station, the needed amount of water is sent to each housing unit and the heat balance of the system is achieved. Geothermal fluid, collected from the four production wells at an average well heat temperature of 95.5°C, is pumped to the inlet of the heat exchanger mixing tank and later to a main collector (from four production wells) with a total mass flow rate of about 47.62 kg/s. Geothermal fluid of intermingling molecules of different species through molecular diffusion was neglected in this study. As a result, not only irreversibility of the mixing tank was assumed to be equal to zero, but also heat losses from the tank and main collector pipe line (5–6) through the mixing process were ignored.

Taking into account the four productive wells when this study was conducted and using Eq. (9.56), the specific exergy index (SExI) is found to be 0.049, which is very close to the limit of the medium-quality geothermal resources. The energy and exergy efficiencies of the SGDHS are determined to be 55.5% and 59.4%, respectively. Here, the exergy efficiency is higher due to the recirculation and heat-recovery processes. The main parameters of this district heating system are listed in Table 9.12.

The highest exergy loss of 20.44% occurs from the natural direct discharge in this study. The second largest exergy destruction occurs from the heat exchanger with 17.90% (about 459 kW) of the total exergy input. This is followed by the total exergy destruction associated with the pumps, amounting to some 57 kW, which accounts for 2.22% of the exergy input to the system.

9.5 Hydro Energy

Hydro energy is derived from solar energy. The difference in elevation of the water level—upstream and downstream of a dam—represents an accumulation of potential energy that eventually can be transformed into mechanical work and thus into electricity. There are a number of water turbines and waterwheels that can generate rotation work when exposed to water flow. It is a worldwide potential method for electric power production and it has gained significance since many rural properties are near rivers with water streams and small water heads that can be used as the primary energy.

Energy is commonly used for stationary machine drivers, generation of electricity, and water storage in elevated reservoirs. Small electric power plants can still be used with waterwheels or, depending on the flow or the available head, with turbines. One important characteristic of a hydropower plant is the head, which represents the difference in elevation of the water level. Based on this, the hydro-energy plants are classified into two categories:

- Low-head power plants: head = 5–20 m
- High-head power plants: head = 20–1,000 m

As a function of the heat and the volumetric flow rate of water, specific turbines or water wheels can be selected. The known hydro-turbines are Pelton, Francis, Michel-Banki, Kaplan, Deriaz (where these are the name of their inventors); also some water pumps can work efficiently in reverse, as turbines.

The conversion of hydro energy into work is governed by the Bernoulli equation, which is a particular form of energy conservation equation. Accordingly, the thermodynamic limit of hydro-energy conversion into work is given by

$$W = \dot{V}\left(0.5\rho v^2 + \rho g \Delta z + P\right), \tag{9.58}$$

where $\dot{V}$ is the volumetric water flow rate, ρ the water density, v the water velocity, Δz the elevation difference, and P the water pressure.

Table 9.12 SGDHS data and energetic, exergetic, and thermodynamics parameters

Item no.	Component	Exergy destruction rate (kW)	Utilized power (kW)	Installed capacity (kW)	P (kW)	Relative irreversibility (%)	Energy efficiency, η (%)	Exergy efficiency, ψ (%)
1	Heat exchanger	458.46	10,226.83	43,961.38	1,524	44.09	–	76.87
2	K4 well pump	21.46	24.75	55	3.29	2.06	65–80	13.29
3	K2 well pump	12.74	20.25	45	7.51	1.22	65–80	37.09
4	K3 well pump	5.23	20.25	45	15.02	0.50	65–80	74.17
5	K7 well pump	–	–	–	–	–	–	–
6	Salihli booster pump	7.3	55	675	47.7	0.70	65–80	86.72
7	Salihli circulation pump	10.28	112.5	537	102.22	0.98	65–80	90.86
8	Heat exchangers and pumps	515.47	10,468.52	45,520.58	1,524	–	–	–
9	Overall system[a]	1,039.67	1,524	45,520.58	1,524	–	55.5	59.44

[a]Based on the exergy (or energy) input to thermal water and water
Data from Özgener et al. (2005)

The thermodynamic limit given by Eq. (9.58) is never reached in practice due to friction in ducts and irreversibilities in the turbine. Thus the efficiency of hydro-energy conversion is commonly 80% with respect to water head $\rho g \Delta z$. The water wheels are the least efficient devices to convert water energy due to losses because of friction, turbidity, and incomplete filling of the buckets. The water pushes the shovels tangentially around the wheel. The water does not exert thrust action or shock on the shovels as is the case with turbines. The advantage of water wheels is that they can operate in dirty water or water with suspension of solids.

The Pelton machine is a turbine of free flow (action). The potential energy of the water becomes kinetic energy through injectors and control of the needles that direct and adjust the water jet on the shovels of the motive wheel. They work under approximate atmospheric pressure with a typical head in the range of 400 to 2,000 m. Compared with the Francis turbine, the Pelton head has a better efficiency curve.

The Francis turbine is used in small hydroelectric power plants with a head in the range of 3 to 600 m while the flow rate of water is in the range of hundreds of dm^3/s. This turbine is very sensitive to cavitation and works well only close to the design point. Its operation becomes unstable at generated power lower than nominal with more than 40%.

The Michel–Banki turbine works with radial thrust. The range of power goes up to 800 kW per unit and the flow rate varies from 25 to 700 dm^3/s with the head in the range of 1 to 200 m. The number of slats installed around the rotor varies from 26 to 30, according to the wheel circumference, whose diameter is 200 to 600 mm. This multicell turbine can be operated at one or two thirds of its capacity (in the presence of low or average flows) or at full capacity (in the presence of design flows). The turbine can be operated even at 20% of its full power.

The Kaplan turbine is a hydraulic propeller turbine adapted to low heads from 0.8 to ~5 m. In addition, this turbine has the advantage of maintaining its electro-mechanical parts out of the water. This feature facilitates routine inspection and maintenance and adds safety in case of floods.

The Deriaz turbine was developed in the 1960s and can reach a capacity of up to 200 MW with flow rates in a broad range (from 1.5 to 250 m^3/s) and with heads of 5 to 1,000 m. The runner diameter may be up to 7,000 mm with six to eight runner blades. Diagonal turbines operate very economically as either turbines or pumps. The thrusting water follows an approximately conic surface around the runner.

The use of water pumps in reverse, as turbines, for small hydroelectric power plants has become quite popular because of the appreciable reduction in facility costs. These pumps, usually of small capacity, have been used for many years in industrial applications to recover energy that would otherwise be lost. They present the following advantages:

- They cost less because they are mass produced for other purposes (such as water pumps for buildings and residences).
- Their acquisition time is minimal because they have a wide variety of commercial standards and are available in hardware stores and similar shops.

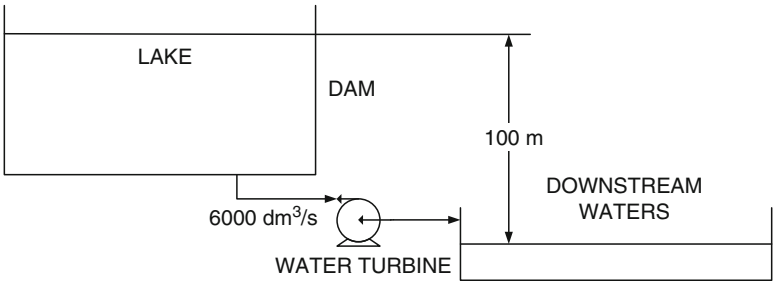

Fig. 9.56 Hydropower setting for the example in the text

However, there are a few disadvantages: slightly reduced efficiency compared with the same head height used for water pumping, and, sensitiveness to the cavitation and operating range.

Example

A typical hydropower setting is illustrated in Fig. 9.56 and has $\Delta z = 100\,\text{m}$ level difference between the lake's surface and downstream waters. On the water stream with a volume flow of $\dot{V} = 6{,}000\,\text{dm}^3/\text{s}$ a turbine coupled to an electric generator that produces $\dot{W} = 4.5$ MW power is installed with $\eta_g = 95\%$ efficiency. We want to calculate the efficiency of the water turbine itself, the overall efficiency, and the power generated by the turbine.

The energy rate supplied to the turbine-generator system is $\dot{E} = \rho \dot{V} \times g \times \Delta z$; assuming density of water of 1 kg/dm^3, the energy rate is $\dot{E} = 5.886$ MW. Thus, the overall conversion efficiency is $\eta = \dot{W}/\dot{E} = 4.5/5.886 = 76\%$. One can assume that the overall conversion efficiency is the product between the turbine and the generator efficiencies $\eta = \eta_t \times \eta_g$; thus, the turbine efficiency is $\eta_t = \eta/\eta_g = 0.76/0.95 = 80\%$. Thus the mechanical power generated by the shaft rotation of the turbine is $\dot{W}_{\text{shaft}} = \eta_t \times \dot{E} = 0.8 \times 5.886 = 4.71$ MW.

9.6 Biomass Energy

Biomass was discussed as a renewable resource in Chapter 2. Basically, any kind of fossilized living species is a form of biomass. It is one of the oldest energy sources on earth and may become one of the most significant large-scale energy sources in the future. Biomass originates from the photosynthesis portion of the solar energy distribution and includes all plant life (terrestrial and marine), all subsequent species in the food chain, and eventually all organic waste. Biomass resources come in a large variety of wood forms, crop forms, and waste forms. The basic characteristic of biomass is its chemical composition in such forms as sugar, starch, cellulose, hemicellulose, lignin, resins, and tannins.

Bioenergy (or biomass energy) can be defined as the energy extracted from biomass for conversion into a useful form for commercial heat, electricity, and transportation fuel applications. The simplest route to biomass energy conversion is

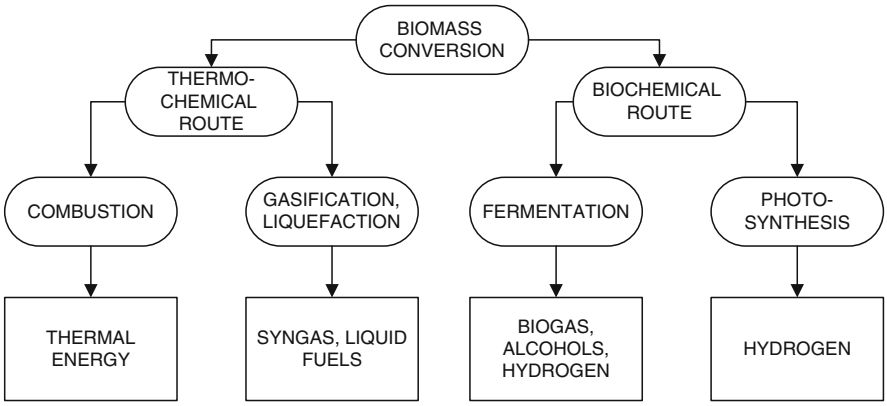

Fig. 9.57 Routes to biomass energy conversion

by combustion to generate heat. The high-temperature heat can be further converted into work through heat engines. Other biomass conversion routes are illustrated in Fig. 9.57. Combustion is a thermochemical process, as is the gasification. Gasification converts the biomass into a gaseous fuel. Liquefaction produces a liquid fuel. Another route of biomass energy conversion is biochemical. In this case, the fermentation process (anaerobic or aerobic digestion) can lead to biogas, alcohol, and hydrogen generation. Also, the photosynthesis process conducted by some phototrophic organisms can eventually produce hydrogen.

Because energy crop fuel contains almost no sulfur and has significantly less nitrogen than fossil fuels [reductions in pollutants causing acid rain (SO_2) and smog (NO_x)], its use will improve the air quality. An additional environmental benefit is in water quality, as energy crop fuel contains less mercury than coal or even none. Also, energy crop farms using environmentally proactive designs will create water quality filtration zones, uptaking and sequestering pollutants, such as phosphorus from soils that leach into water bodies.

Biomass generates about the same amount of CO_2 as do fossil fuels (when burned), but from a chemical balance point of view, every time a new plant grows, CO_2 is actually removed from the atmosphere. The net emission of CO_2 will be zero as long as plants continue to be replenished for biomass energy purposes. If the biomass is converted through gasification or pyrolysis, the net balance can even result in removal of CO_2. Energy crops such as fast-growing trees and grasses are called biomass feedstocks. The use of biomass feedstocks can help increase profits for the agricultural industry.

9.6.1 Thermodynamic Limits of Biomass Energy Conversion

The general model of biomass energy conversion into work can consist of an adiabatic combustor and a reversible heat engine. Figure 9.58 illustrates the biomass energy conversion system for maximum work generation. The biomass

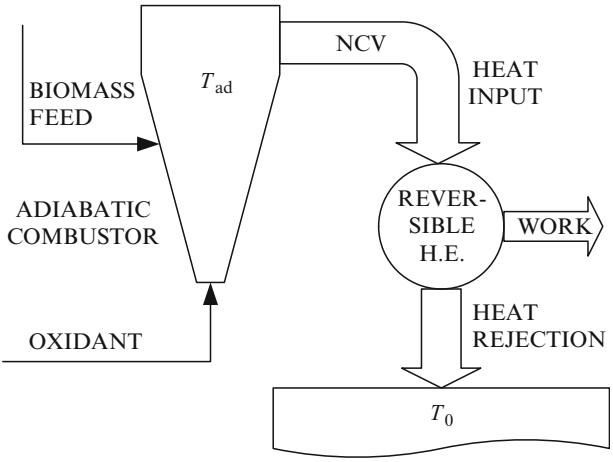

Fig. 9.58 Thermodynamic model for biomass energy conversion into work. *H.E.* heat engine

combusts in an adiabatic combustor that operates at the highest possible temperature (adiabatic flame temperature, T_{ad}). The heat generated in this process is the net calorific value of the biomass (NCV). This heat is further used to drive a reversible heat engine that generates useful work while it is in contact with the environment at the low-temperature side.

The work generated by this system is thus $\dot{W} = \text{NCV} \times (1 - T_0/T_{ad})$, and thus the efficiency of the biomass conversion process is given by the adiabatic flame temperature only $\eta = 1 - T_0/T_{ad}$. Therefore, determining the thermodynamic limit of biomass energy conversion is equivalent to determining the adiabatic flame temperature for the biomass. Thus, we will analyze the biomass composition and the way in which this affects the net calorific value of biomass and the corresponding adiabatic flame temperature.

The biomass contains various biochemicals (amino acids, fiber, cellulose, sugars, glucose, and many other). Some living micro-organisms and enzymes may be found in biomass. The most abundant chemical elements in biomass are carbon, hydrogen, oxygen, nitrogen, and sulfur. Other elements are also present, including metal atoms. When biomass is combusted, the metal atoms and other elements form ash.

Some biomass modeling equations were presented in Chapter 6. We repeat them here and we expand the theory. The general chemical model of biomass is written as $C_{X_C}H_{X_H}O_{X_O}N_{X_N}S_{X_S}\text{ash}_{X_{ash}}(H_2O)_{X_w}$, where X_i is the number of constituents of species "i." If the moisture (water) is eliminated by some drying process, then the chemical representation of the dry biomass becomes $C_{X_C}H_{X_H}O_{X_O}N_{X_N}S_{X_S}\text{ash}_{X_{ash}}$. The molecular mass of dry biomass can be calculated with

$$M = 12 \times X_C + X_H + 16 \times X_O + 14 \times X_N + 32 \times X_S + M_{ash}X_{ash}. \tag{9.59}$$

On a dry basis, the mass concentration of each major chemical element constituent is $w_C = 12 \times \frac{X_C}{M}$; $w_H = \frac{X_H}{M}$; $w_O = 16 \times \frac{X_O}{M}$; $w_N = 14 \times \frac{X_N}{M}$; $w_S = 32 \times \frac{X_S}{M}$; $w_{ash} = M_{ash} \times \frac{X_{ash}}{M}$, where $w_{ash} = 0.5$–12% dry basis. The moisture content of biomass typically has a moisture concentration in the range of $w_w = 0$–50% that can be expressed on a wet basis as

$$M_{wet} = M + X_w \times 18. \tag{9.60}$$

Thus,

$$w_w = \frac{18X_w}{M + X_w \times 18}. \tag{9.61}$$

If the mass concentration of the moisture is known, then the molar concentration can be determined by

$$X_w = \frac{w_w M}{18(1 - w_w)}. \tag{9.62}$$

Equations (9.61) and (9.62) are useful for biomass combustion calculations and for determining its calorific and exergetic content. Thus, the gross calorific value of biomass can be calculated with

$$\begin{aligned} \mathrm{GCV} = {} & 34.91w_C + 117.83w_H + 10.05w_S - 1.51w_N - 1.034w_O \\ & - 2.11w_{ash} \end{aligned} \tag{9.63}$$

(see Van Loo and Koopejan 2008). The net calorific value is calculated under the constraint that water in the exhaust gases is in the vapor phase and all exhaust gases are at the same temperature as the biomass at the feed (standard temperature). The net calorific value can be calculated with

$$\mathrm{NCV} = \mathrm{GCV}(1 - w_w) - 2.444w_w - 2.444w_H \times 8.936(1 - w_w). \tag{9.64}$$

Szargut (2005) gives an equation for the chemical exergy of biomass (where the contribution of the sulfur to the combustion process is ignored):

$$e^{ch}_{x,Bmass} = \mathrm{NCV} \times \left(1.0347 + 0.014\frac{X_H}{X_C} + 0.0968\frac{X_O}{X_C} + 0.0493\frac{X_N}{X_C}\right). \tag{9.65}$$

The stoichiometric equation for complete biomass combustion with pure oxygen is as follows:

$$\begin{aligned} & C_{X_C}H_{X_H}O_{X_O}N_{X_N}S_{X_S}\mathrm{ash}_{X_{ash}}(H_2O)_{X_w} + X_{O_2}O_2 \\ & \quad \rightarrow X_C CO_2 + X_{H_2O}H_2O + X_N/2N_2 + X_S SO_2 + X_{ash}\mathrm{ash}, \end{aligned} \tag{9.66}$$

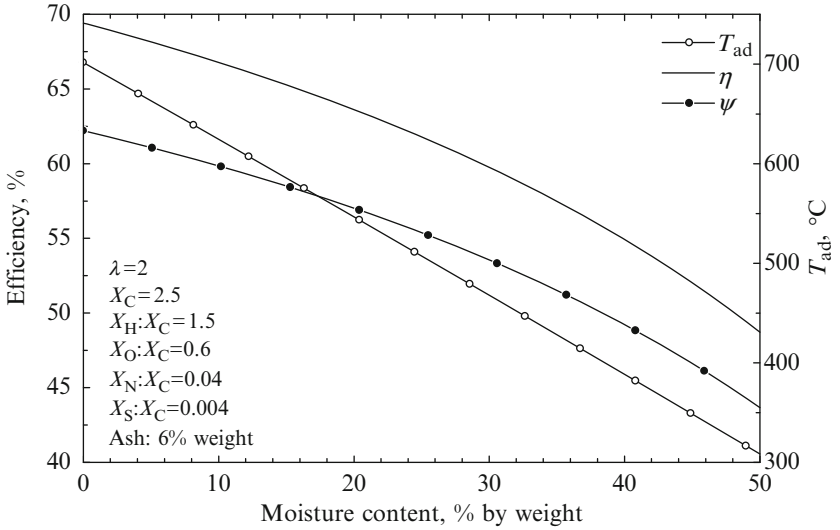

Fig. 9.59 Variation of adiabatic flame temperature, energy and exergy efficiency of biomass conversion with the moisture content

where $X_{O_2} = 2X_C + X_H/2 + 2X_S - X_O$; $X_{H_2O} = X_H/2 + X_w$. The corresponding energy balance is written as

$$h_{BMAF} = h_{BM} - X_{ash}h_{ash} = X_C h_{CO_2} + X_{H_2O}h_{H_2O} + X_S h_{SO_2} + NCV, \tag{9.67}$$

where h_{BM} is the formation enthalpy of biomass with respect to chemical elements and h_{BMAF} is the same for the ash-free biomass.

The general chemical equation of biomass combustion with enriched oxygen and flue gas recirculation is $C_{X_C}H_{X_H}O_{X_O}N_{X_N}S_{X_S}ash_{X_{ash}}(H_2O)_{X_w} + \lambda X_{O_2}[\zeta(O_2 + 3.76N_2) + (\zeta - 1)O_2] \rightarrow Prod + X_{ash}$ ash, where $\lambda \geq 1$ is the excess oxygen; 3.76 is the concentration of nitrogen in fresh air, $\zeta = 0 - 1$ is the fraction of fresh air, and "Prod" are the reaction products in the form of flue gas. Assuming complete combustion, then $Prod = X_C CO_2 + X_{H_2O}H_2O + X_S SO_2 + X_{N_2}N_2 + (\lambda - 1)X_{O_2}O_2$, where the stochiometric coefficients for nitrogen is $X_{N_2} = X_N/2 + 3.76\lambda\zeta X_{O_2}$.

Using Eqs. (9.59) to (9.67), it is easy to obtain the plot on Fig. 9.59 illustrating the variation of adiabatic flame temperature and conversion efficiency of a typical biomass with the moisture content. The energy and exergy efficiencies are calculated based on the useful work generated and the energy/exergy input (see Fig. 9.58) as

$$\left.\begin{aligned} \eta &= 1 - \frac{T_0}{T_{ad}} \\ \psi &= \frac{NCV}{ex^{ch}} \times \left(1 - \frac{T_0}{T_{ad}}\right) \end{aligned}\right\}. \tag{9.68}$$

Table 9.13 Characteristics of some biomass resources

Biomass type	Moisture content (% wb)	Bulk density (kg wb/m^3)	T_{ad} (°C)	GCV (MJ/kg db)	NCV (MJ/kg wb)	ex^{ch} (MJ/kg wb)
Wood pellets	10	600	1,140	19.8	16.4	18.3
Woodchips	30–50	250–450	530–840	19.8	8–12.2	8.9–13.6
Sawdust	50	240	530	19.8	8	8.9
Bark	50	320	540	20.2	8.2	9.2
Grass	18	200	1,020	18.4	13.7	15.3
Cereals	15	175	1,065	18.7	14.5	16.2
Straw	15	120	1,065	18.7	14.5	16.2
Olive kernels	53–63	650–1,130	370–530	21–23	6.5–8.5	7.1–9.0

db dry basis; *wb* wet basis in percent by weight

The maximum conversion efficiencies are obtained with dry biomass (moisture content 0%) and excess oxidant (air) as low as the stoichiometric one ($\lambda = 1$). In these conditions, the adiabatic flame temperature as well as the maximum biomass energy conversion efficiencies reach values around $T_{ad} = 1{,}280 - 1{,}300°C$, $\eta \cong 80\%$, and $\psi \cong 72\%$. Table 9.13 lists the characteristics of some biomass resources.

9.6.2 Conversion of Biomass in Biofuels

Biomass can be converted to a gaseous fuel by the two routes that were suggested in Fig. 9.57, namely the thermochemical and biochemical conversion routes. Through the thermochemical conversion route biosyngas is obtained, while by biochemical conversion one can generate either biogas or hydrogen.

The first step in thermochemical conversion of biomass is pyrolysis. Biomass pyrolysis refers to a process in which biomass is exposed to high temperatures in the absence of air, causing the biomass to decompose. The end product of pyrolysis is a mixture of solids (char), liquids (oxygenated oils), and gases (CH_4, CO, and CO_2). Flash pyrolysis gives high oil yields, but because of the technical effort needed to process pyrolytic oils, this energy-generating system does not seem very promising at the present stage of development. However, pyrolysis as a first stage in a two-stage gasification plant for straw and other agricultural feedstocks that pose technical difficulties in gasification does deserve consideration.

There are several widely used process designs for biomass gasification: (1) staged reformation with a fluidized-bed gasifier, (2) staged reformation with a screw auger gasifier, (3) entrained flow reformation, and (4) partial oxidation. In staged steam reformation with a fluidized-bed reactor, the biomass is first pyrolyzed in the absence of O_2. Then the pyrolysis vapors are reformed to synthesis gas with steam, providing added H_2 as well as the proper amount of O_2 and process heat that comes from burning the char. With a screw auger reactor, moisture (and O_2) is introduced at the pyrolysis stage, and process heat comes from burning some of the gas produced in the latter. In entrained flow reformation, external steam and air are introduced in a single-stage gasification reactor. Partial oxidation gasification uses

pure O_2 with no steam, to provide the proper amount of O_2. Using air instead of O_2, as in small modular uses, yields produced gas (including NO) rather than synthesis gas. A workable gasification process requires development of some technology, such as feed processing and handling, gasification performance improvement, syngas cleanup and conditioning, development of sensors, instruments and controls, process integration, and materials used for the systems.

The typical biochemical route to biomass gasification leads to biogas generation. Biogas, also termed methane or gobar gas, comprises a mixture of gases. It is a fuel of high caloric value resulting from anaerobic fermentation of organic matter called biomass. Composition of this gas varies with the type of organic material used. The caloric power of biogas depends on the amount of methane in its composition, which could reach 20 to 25 MJ/m^3. Biogas can be used for stove heating, water heaters, flowtorches, motors, and other equipment. Biogas contains typically 60% to 70% methane and 30% to 40% carbon dioxide with traces of nitrogen, ammonia, hydrogen, and hydrogen sulfide.

Several biodigester models are available. In a basic one, the digester is a reservoir built of bricks or concrete below ground level. A wall divides the biodigester into two semicylindrical parts for the purpose of retaining and providing circulation for the biomass loaded in a biofertilization process. The biodigester is loaded through the charge box, serving as a pre-fermenter. The load is typically a slurry containing biomass mixed with water. The charge box communicates with the digester through a pipe going down to the bottom. The output of the biofertilizer is through another pipe at a level that ensures that the amount of biomass entering the biodigester is the same as that leaving it in biofertilizer form. It should also have a discharge box, tank, or dam to pump and/or deliver the biofertilizer directly to the consumer. For a production capacity of 5 to 6 m^3 biogas per day, the biodigester has 3-m diameter and 3-m height, consumes 250 L of biomass per day, and has a retention time of about 50 days. The biodigester is usually buried because underground temperatures are higher and more constant. The process is affected by the material temperature (commonly 30–35°C), biodigestion acidity (i.e., pH: preferably 6–8), nutrients (e.g., N_2) and their concentration, and the concentration of solids (commonly 7–9%).

The type of biomass used in the biodigester can be diverse, including residues from industrialization of fruits, meats, cereals, and alcohol. Urban garbage can also be used as feedstock for biodigesters and transformed thus into sources of energy. The specific production of biogas is presented in Table 9.14 for various kinds of feedstock.

Similar to the case of biomass conversion into gas, its conversion into liquid fuels can be done through thermochemical or biochemical routes. Through liquefaction one obtains fuel oil. Liquefaction can be done by exposing a mixture of liquid water and solid biomass to high pressures and high temperature. The pressure is commonly of the order of 200 bar (that is close to the critical pressure of water). The biochemical route occurs through fermentation and leads to production of alcohols. In general, through biofuels, liquid fuels are obtained from biomass (biodiesel, bioethanol, biomethanol, biogasoline, etc.). However, the term *biofuel*

Table 9.14 Specific biogas production for several kinds of vegetable and manure feedstock

Feedstock	Production (m^3 gas per ton of feedstock)	Feedstock	Production (m^3 gas per ton of feedstock)
Bean straws	380	Rice straws	300
Sunflower leaves	300	Wheat straws	300
Soy straws	300	Linen stem	360
Potato leaves	270	Dry tree leaves	250
Grapevine leaves	270	Birds	55
Bovines	40	Equines	48
Suidae	64	Oviparous	70

is general, referring to any kind of fuel derived from biomass, be it gas (biogas, hydrogen, carbon monoxide), liquid, or solid (the biomass itself is a solid fuel). Thus, in general, biofuels include wood, wood waste, wood liquors, peat, railroad ties, wood sludge, spent sulfite liquors, agricultural waste, straw, tires, fish oils, tall oil, sludge waste, waste alcohol, municipal solid waste, landfill gases, other waste, and ethanol blended into motor gasoline.

Hydrogen can be also generated from biomass through several methods. These are discussed in detail in Chapter 13.

9.6.3 Electricity Generation

Several alternatives are available for generation of electric power from biomass. The simplest possibility to do this is by direct combustion of biomass to fire a steam generator that drives a turbine. Biomass combustion facilities also can be coupled with organic Rankine cycles, which are characterized by good turbine efficiency at low installed capacities. A basic biomass combustion facility coupled with a steam power plant is shown in Fig. 9.60.

In this system, biomass is first dried using the flue gas heat generated by the combustion process itself. Next, the dried biomass is combusted and the hot flue gas used to generate steam for a steam Rankine cycle power generator. Figure 9.61 shows an improved power generation system that generates electricity and steam from biomass energy. This system uses biomass gasification to generate clean synthesis gas that is fed into a solid oxide fuel cell (SOFC) system. The reaction products generated by SOFC are further combusted and the combustion heat used for air preheating and steam generation. Steam is partly used by the gasification process, and partly is supplied to users as a form of cogenerated heat. The remaining heat of the flue gases is used to dry the biomass prior to gasification.

Colpan et al. (2010a) analyzed and compared the efficiency and environmental impact of the power generation systems shown in Fig. 9.60 (conventional system) and Fig. 9.61 (advanced system with biomass gasification). Note that HRSG in the

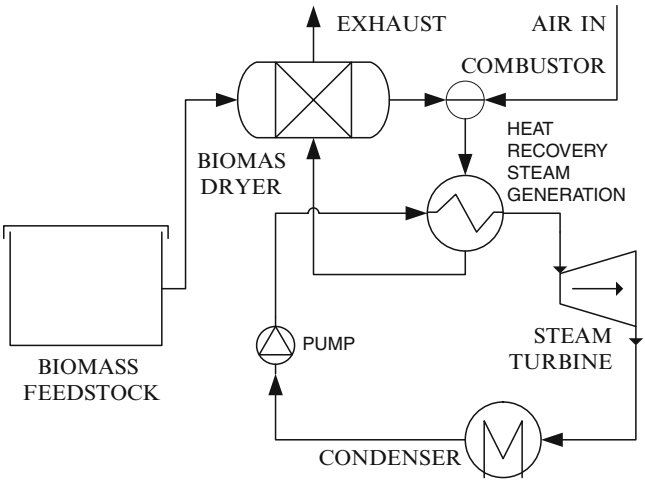

Fig. 9.60 Conventional biomass-fueled power generation system

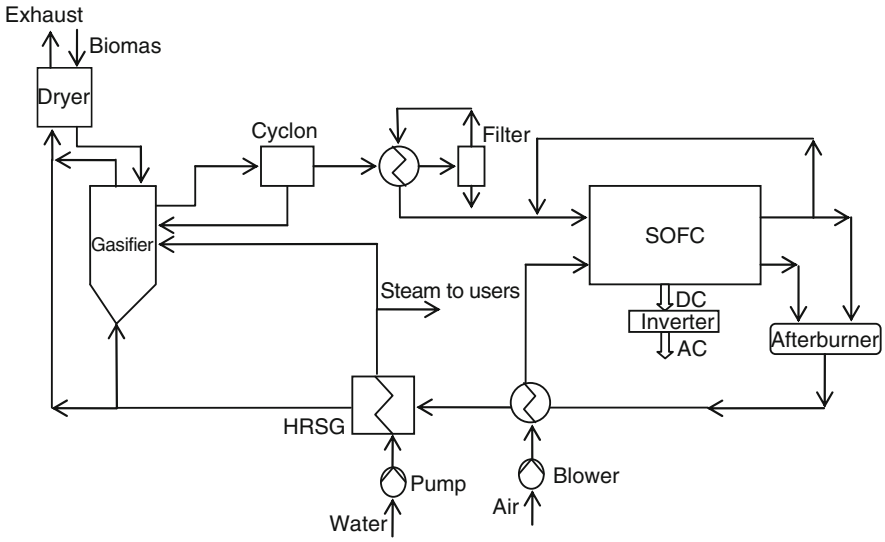

Fig. 9.61 Advanced power generation system with biomass gasifier and SOFC [modified from Colpan et al. (2010a)]

figure means heat recovery steam generator. The environmental impact of these systems can be assessed by calculating the specific greenhouse gas emissions, which are defined as the ratio of the GHG emissions from the system to the net power output of the system. From the viewpoint of energy and environment, the lower the ratio, the more environmentally friendly the system; the ratio is given as $\dot{m}_{\mathrm{GHG}}/\dot{W}_{\mathrm{net}}$. Assuming the case study data summarized in Table 9.15, the results

Table 9.15 Case study parameters for conventional and advanced biomass power generation

Environmental temperature	25°C
Type of biomass	Wood
Ultimate analysis of biomass (%wt dry basis)	50% C, 6% H, 44% O
Moisture content in biomass (%wt)	30%
Exhaust gas temperature	127°C
Conventional system (Fig. 9.60)	
Conditions of the steam entering the steam turbine	20 bar (saturated)
Pressure of the condenser	1 bar
Isentropic efficiency of the steam turbine	80%
Isentropic efficiency of the pump	80%
Electricity generator efficiency	98%
Advanced system (Fig. 9.61)	
Moisture content in biomass entering the gasifier (%wt)	20%
Temperature of syngas exiting the gasifier	900°C
Temperature of steam entering the gasifier	300°C
Molar ratio of steam to dry biomass	0.5
Number of cells per SOFC stack	50
Temperature of syngas entering the SOFC	850°C
Temperature of air entering the SOFC	850°C
Pressure of the SOFC	1 atm
Cell voltage	0.7 V
Reynolds number at the fuel channel inlet	1.2
Excess air coefficient	7
Active cell area	10×10 cm^2
Number of repeat elements per single cell	18
Flow configuration	Co-flow
Manufacturing type	Electrolyte supported
Thickness of the air channel	0.1 cm
Thickness of the fuel channel	0.1 cm
Thickness of the interconnect	0.3 cm
Thickness of the anode	0.005 cm
Thickness of the electrolyte	0.015 cm
Thickness of the cathode	0.005 cm
Pressure ratio of the blowers	1.18
Isentropic efficiency of the blowers	0.53
Pressure ratio of the pump	1.2
Isentropic efficiency of the pump	0.8
Inverter efficiency	0.95

Data from Colpan et al. (2010a)

presented in Fig. 9.62 are obtained. For the advanced system, the syngas composition is first calculated as 2.08% CH_4, 42.75% H_2, 25.80% CO, 9.44% CO_2, and 19.93% H_2O. The average current density of the cell is 0.253 A/cm^2 for the cell operating voltage of 0.7 V. It is found that the fuel utilization of the SOFC is 82%.

As shown in Fig. 9.62, the electrical and exergetic efficiencies of the conventional system are 8.3% and 7.2%, respectively, whereas the electrical and exergetic efficiencies of the advanced system are 44.9% and 41.1%, respectively. The environmental impact of the systems studied is compared calculating the specific GHG emissions from these systems. It is found that the conventional system has higher GHG emissions compared to the advanced system. As shown in Fig. 9.62,

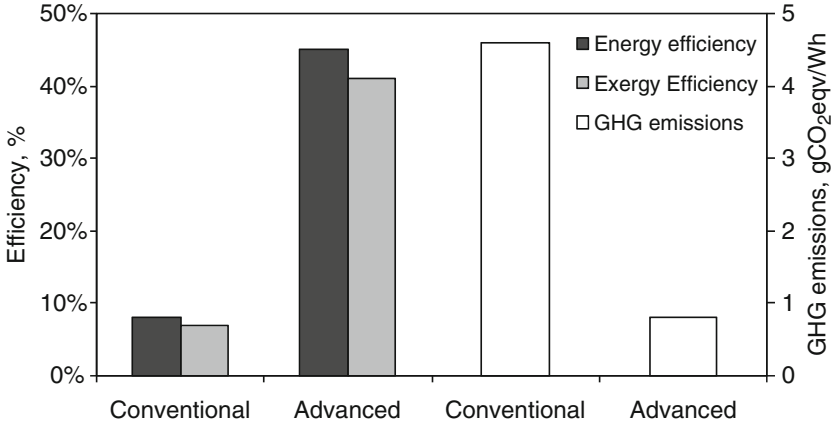

Fig. 9.62 Efficiency and GHG emission for conventional and advanced biomass power generation systems analyzed above [data from Colpan et al. (2010a)]

the specific GHG emissions are 4.564 g CO_2 eq/Wh and 0.847 g CO_2 eq/Wh for the conventional and the advanced system, respectively.

Figure 9.63 suggests an improved system that uses several thermodynamic cycles to generate power and heat through biomass gasification. The gasifier module converts biomass to a clean gas for power and steam generation with a combined system including a Brayton cycle, a steam expansion turbine, and a solid oxide fuel cell. In this system, biomass is gasified first and used in a gas turbine and a fuel cell system that operate in parallel. The uncombusted gases are directed toward a low-pressure combustor where additional combustion is applied at low pressure. The flue gases are used to generate high-pressure superheated steam that is expanded in a steam turbine. The resulting low pressure steam can be used for some heating applications. Another part of the high pressure steam is used for the gasification process.

The combined heat and power generation (via biomass gasification techniques connected to gas-fired engines or gas turbines) can achieve significantly higher electrical efficiencies, between 22% and 37%, than those of biomass combustion technologies with steam generation and steam turbine, 15% to 18%. If the gas produced is used in fuel cells for power generation, an even higher overall electrical efficiency can be attained, in the range of 25% to 50%, even in small-scale biomass gasification plants and under partial-load operation.

Due to the improved electrical efficiency of the energy conversion via gasification, the potential reduction in CO_2 is greater than with combustion. The formation of NO_x compounds can also be largely prevented, and the removal of pollutants is easier for various substances. The NO_x advantage, however, may be partly lost if the gas is subsequently used in gas-fired engines or gas turbines. Significantly, lower emissions of NO_x, CO, and hydrocarbons can be expected when the gas produced is used in fuel cells rather than in gas-fired engines or gas turbines.

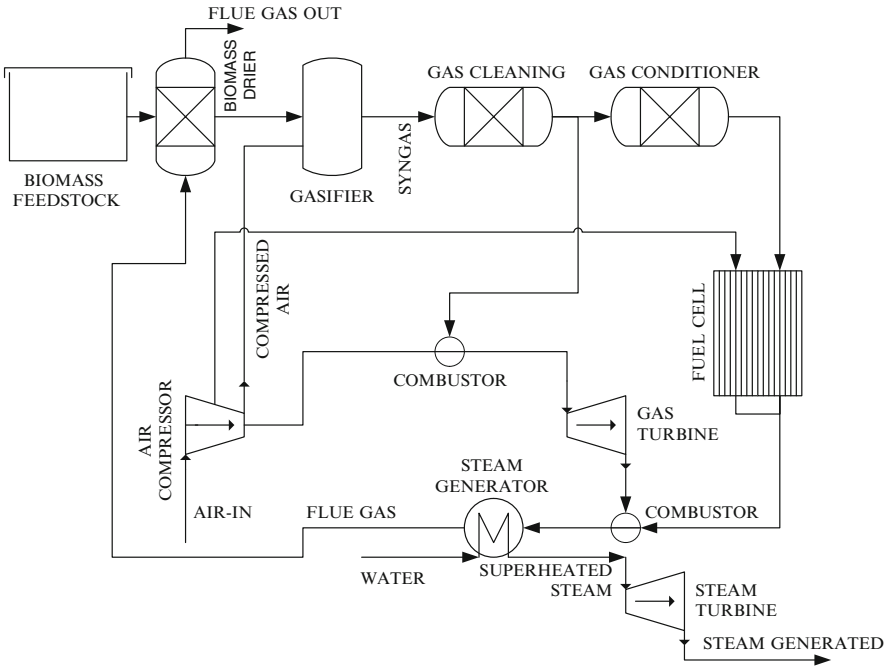

Fig. 9.63 System for electric power generation from biomass

When biomass is converted to biogas, then electric power generators based on internal combustion engines can be used for power production. It is also possible to couple biogas production facilities with micropower plants comprising gas turbines cascaded with reciprocating internal combustion engine. For micropower plants, alcohol and gasoline motors can be made to operate with methane without affecting their operational integrity. This adaptation is made by installing a cylinder of biogas in place of using conventional fuel. For gas flow regulation, a reducer is placed close to the motor.

It is interesting to introduce here the concept of biorefinery, which is an integrated hybrid system with multigeneration. The two technological platforms for biomass conversion, the biochemical and thermochemical ones, can be combined into the general concept of biorefinery. This is a facility that processes biomass to generate multiple products such as biodiesel, bioethanol, other liquid fuels, electric power, heat, hydrogen, and valuable bioproducts or biochemicals. The concept of biorefinery is illustrated schematically in Fig. 9.64.

The upper branch comprises thermochemical processes (see the figure), including gasification, gas separation, hydrogen production, Fischer–Tropsch synthesis to produce biodiesel, and heat recovery to produce steam, process heat and electricity. The lower branch comprises mostly biochemical processes including lignin separation from biomass. Lignin is a valuable commercial product that can be used in many chemical processes such as water formulation of dyes, production of humic acid and vanillin, an agent for leather tanning, and polyurethane foam.

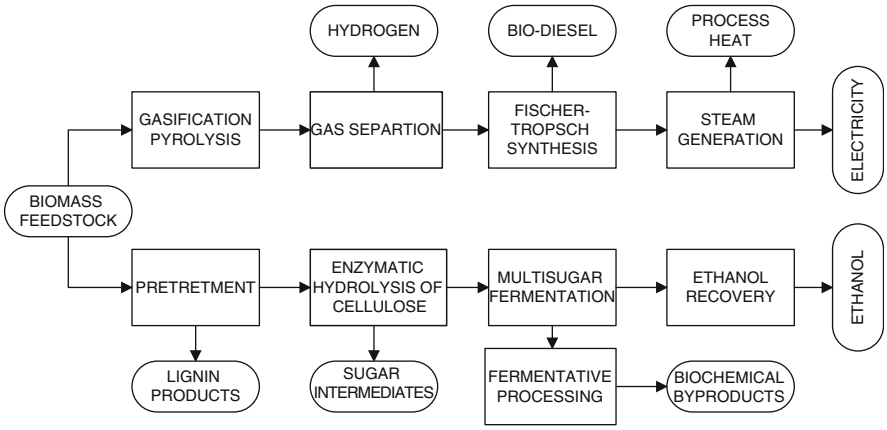

Fig. 9.64 Conceptual diagram of an integrated biorefinery

Through further enzymatic hydrolysis of cellulose one can produce a large variety of sugar intermediates. Further fermentative processes lead to production of ethanol and other biochemical by-products.

9.7 Ocean Thermal Energy

The temperature gradient of the ocean's depth results in a temperature difference just large enough over reasonable depths to extract thermal energy at low efficiency. This is called ocean thermal energy conversion (OTEC). Ammonia–water Rankine and Kalina cycles were proposed for OTEC. In arctic regions the difference in the temperature between water and cold atmospheric air can reach 40°C; in such locations there is potential for OTEC that operates between the surface water (heat source) and the atmospheric air (heat sink).

An OTEC system configuration is illustrated in Fig. 9.65. The system is basically a Rankine cycle operating with ammonia as the working fluid. The system can be installed on a floating platform or on a ship. It uses the surface water as the source. Normally, the water at the ocean surface is at a higher temperature than the water at the ocean's depths. The surface water is circulated with pumps through a heat exchanger that acts as a boiler for ammonia. Water from the deep ocean at 4°C is pumped to the surface, and used as the heat sink in an ammonia condenser.

Basically, the ocean surface in tropical oceans is warmed by the solar radiation to a depth of about 50 m. At depths of 1,000 m or more, the temperature is quasi-constant at 4°C. Therefore, all year round in tropical oceans there is a quasi-constant temperature difference between the surface and the deep water of 20° to 25°C. The thermodynamic limit for OTEC as expressed by the Carnot factor is 6% to 10%.

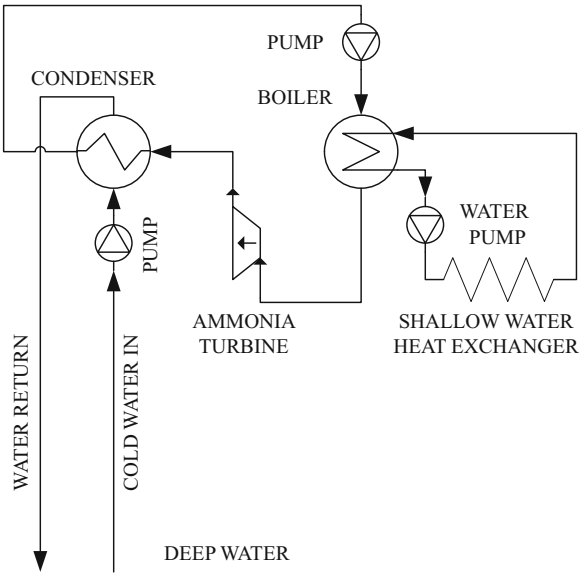

Fig. 9.65 Ocean thermal energy conversion system working with ammonia

Experimental tests and calculations show that at least 3% to 5% conversion is achievable (see comments in Zamfirescu and Dincer 2008b and Avery et al. 1985). Ammonia Rankine or Kalina cycles are the preferred solution for OTEC because the turbine shaft of the Rankine or Kalina power plant is connected with an electric generator to generate electricity. In general, it is difficult to transport the electricity generated by an OTEC plant ship since it is supposed to operate far from the shores. Thus, transporting the energy in chemicals is a better option. One cited option is to produce hydrogen from OTEC. This can be done through ocean water electrolysis. According to past studies [e.g., Avery et al. (1985)] building OTEC plant ships that generate hydrogen, transporting it to shore, and converting it into electricity are economically feasible in units of 150 to 400 MW electrical energy each.

It is suggested that hydrogen can be transported to shore either in the compressed phase, as cryogenic liquid, or by incorporating it into ammonia or methanol, which are substances relatively easy to manufacture onboard the plant ship. Calculations by Avery et al. (1985) show that when energy is transported in the form of ammonia or methanol, the overall electricity cost ends up to be about the same; however, the end-user cost is about four times higher if energy is transported in the form of liquefied hydrogen.

If the energy generated by OTEC is transported to shores in the form of ammonia or methanol and thereafter converted back to electricity, then the overall power production efficiency is about the same for both cases. However, if the OTEC energy is transported in the form of liquefied hydrogen, then the overall cost of electricity is estimated to be four times higher.

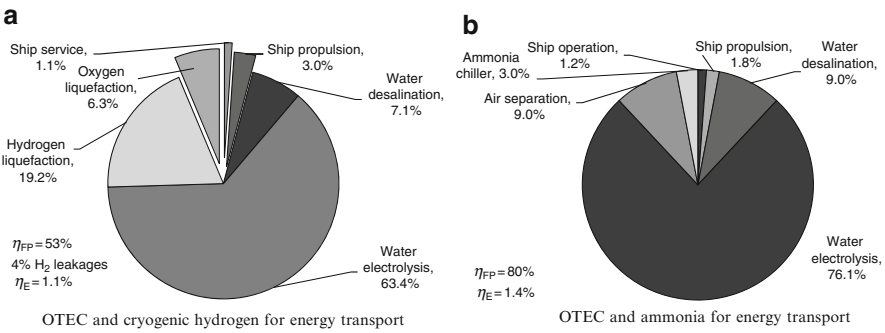

Fig. 9.66 Energy breakthroughs at OTEC using cryogenic hydrogen (**a**) or ammonia (**b**) as energy carriers [data from Avery et al. (1985)]

Figure 9.66 compares the energy breakthroughs at OTEC using cryogenic hydrogen or ammonia. The efficiency of OTEC electricity generation onboard the ship is assumed conservatively at 3%. The fuel conversion efficiency is defined as the energy in produced fuel with respect to HHV divided by the electrical energy input consumed by the fuel-generating plant. This efficiency is denoted by η_{FP}. In the case of a cryogenic hydrogen carrier, from the total of 100% electrical power input, the hydrogen production and transport facility loses (see Figure 9.66) 7.1% for water desalination, 63.4% for water electrolysis, 19.2% for hydrogen liquefaction, 6.3% for oxygen liquefaction (whereas the oxygen is to be used on the shore to produce electricity in fuel cells with improved efficiency), and 4% for hydrogen leaks during transport. At electricity production on the shore, hydrogen and oxygen are recombined in fuel cell systems cascaded with gas turbines and the Rankine cycle, operating at an assumed efficiency of 70%. Thus the hydrogen production efficiency (including the transport) is evaluated at 53%, while the overall OTEC electric power production on the shore is generated with the estimated efficiency of 1.1%.

In the case of ammonia as the carrier, the Haber–Bosch process is used for synthesis onboard. The electrolysis of water consumes 76% of the OTEC electricity generated onboard, air separation (needed to produce nitrogen) consumes 9% of the OTEC electricity, and water desalination consumes 9%. The ammonia synthesis reaction is exothermic; thus, it allows for the opportunity of heat recovery within the process. The ammonia production and transport efficiency is 80% and the overall electricity generation efficiency on the shore is 1.4%. For electricity generation, ammonia used in fuel cells is assumed to be 60% efficient.

9.8 Tidal and Wave Energy

Apart from being an immensely large thermal energy storage system (which is an indirect form of solar energy storage), oceans are at the same time huge reservoirs of mechanical energy. This mechanical energy manifests in the form of tides, ocean

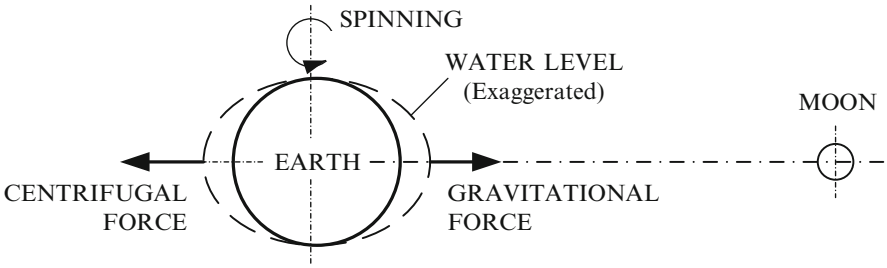

Fig. 9.67 Explaining the formation of tides

currents, and ocean waves. The kinetic energy resulting from the moon's (in addition to the sun's smaller) gravitational pull on the oceans under the earth's rotation produces a diurnal tidal effect. The formation of tides is explained in Fig. 9.67. Basically two bulges of water are formed at the equatorial belt due to the combined action of gravitational and centrifugal forces. Tidal energy shows good potential for electric energy generation. Their associated energy can be converted into electricity by two methods:

- Generation of a difference in water level through impoundment. When tides come into the shore, they can be trapped in reservoirs behind the dams. Then when the tide drops, the water behind the dam can be let out just like in a regular hydroelectric power plant. Since the tidal water level difference is rather small, Kaplan turbines are mostly used to generate power.
- Momentum transfer between the currents generated by tides and a conversion device such as water turbine. Ocean current-harvesting systems are used to rotate propellers that are coupled to electric generators.

Tidal impoundment (barrage) system can have three methods of operation depending on the phase when the tide generates power: ebb generation, flood generation, and two-way generation. When ebb generation is applied, the basin is filled during the flood tide. During the night additional water can be pumped into the basin as a means of energy storage during the off-peak hours. When the tide ebbs low enough, water is discharged over turbine systems that generate power. In flood generation, the dam gates are closed such that the water level increases on the ocean side until it reaches the maximum. Then water is allowed to flow through the turbine systems and to charge the basin while generating power. In two-way generation, electricity is generated both in the flood and the ebb phases of the tide. In Table 9.16 are listed some of the main tidal power generation systems and their principal characteristics. The world's largest tidal power generation site is in France at La Rance, with an installed capacity of 240 MW that operates with 24 reversible turbines and a hydrostatic head of 5 m.

Ocean water currents are generated by the action of tides, the earth's spinning, the heat cycle of tropical solar energy, and superficial winds. The water current's energy can be extracted through current turbines submerged in water. Basically, water current turbines are similar to wind turbines, with the difference that the

Table 9.16 Some of the major tidal impoundment sites

Location	Head (m)	Mean power (MW)	Production (GW h/year)
Minas–Cobequid, North America	10.7	19,900	175,000
White Sea, Russia	5.65	14,400	126,000
Mount Saint Michel, France	8.4	9,700	85,100
San Jose, Argentina	5.9	5,970	51,500
Shepody, North America	9.8	520	22,100
Severn, UK	9.8	1,680	15,000

Data from O'Rourke et al. (2010)

density and the viscosity of water are 100 and 1,000 times higher, respectively, than that of air. Therefore, there are some differences in operating conditions of water current turbines versus wind turbines. Similarly as for wind turbines, water current turbines are made in horizontal axis or vertical axis construction. The thrust generated by water current turbines is much higher than that specific to wind turbines; therefore, their construction material must be more massive and resistant.

Surface winds, tides, and ocean currents contribute to the formation of ocean waves. The energy of waves can be collected with floating bodies that execute elliptic movement under the action of gravity and wave motion. The wave energy can be measured in terms of wave power per meter of wave front. The highest wave power on the globe appears to be in southern Argentine across the Strait of Magellan where wave power density can reach 97 kW/m. Also along the southwestern coast of South America, the wave power density is over 50 kW/m and often over 70 kW/m. In southwestern Australian coasts the wave power reaches 78 kW/m. In the Northern Hemisphere, the highest wave intensity is found along the coast of western Ireland and the UK with magnitudes around 70 kW/m. The southern coast of Alaska records wave power density of up to 65 to 67 kW/m. The wave power density on other coastal regions varies from about 10 kW/m to 50 kW/m. This impressive amount of energy can be converted into electricity with relatively simple mechanical systems that can be classified into two kinds: buoy and turbine type.

The principle of operation schematic of a buoy-type wave energy converter is shown in Fig. 9.68 and operates based on hydraulic-pneumatic systems. The buoy oscillates according to the wave movement at the ocean's surface. It transmits the reciprocating movement to a double effect hydraulic pump that is anchored rigidly on the ocean bottom. The pump generates a pressure difference between two pneumatic-hydraulic cylinders. A hydraulic motor generates shaft work by discharging the high-pressure liquid into a low-pressure reservoir. The shaft work turns an electric generator that produces electricity.

The energy of waves is correlated with the energy of surface winds. Two issues are important in determining the interrelation between the wave height and the wind characteristics, namely the wind–water fetch (i.e., the length over which the superficial wind contacts the water) and the duration of the wind. For example, if the wind blows constantly for 30 hours at 30 km/h and contacts the water over a length of 1,200 km, the wave height can reach 20 m (see Da Rosa 2009). The power density of the wave in deep ocean water can be approximated with

$$\dot{W} = 0.5v\rho g h^2, \tag{9.69}$$

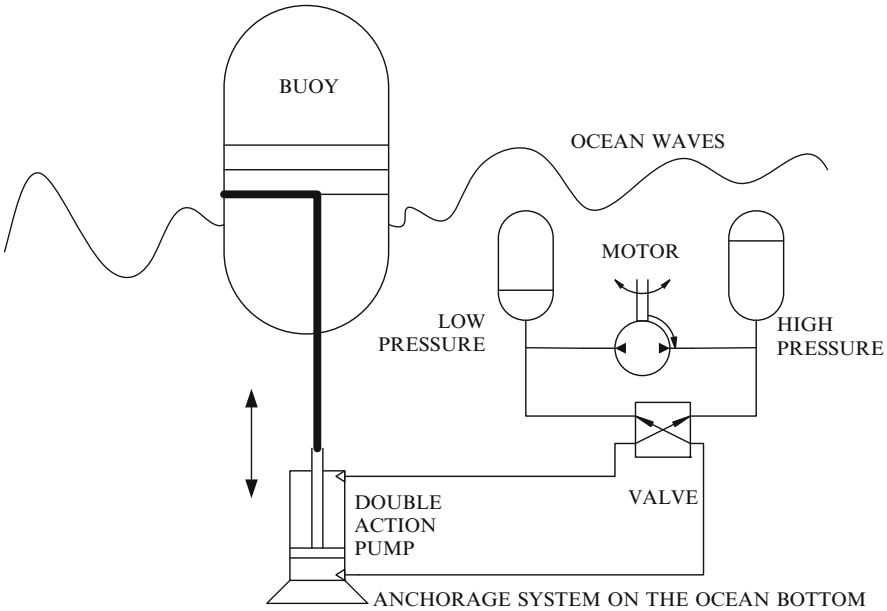

Fig. 9.68 Principle of operation of buoy-type ocean wave energy conversion system

while in shallow waters it is about half of this; in Eq. (9.69) v is the eave speed, ρ is the water density, $g = 9.81\ \text{m/s}^2$ is the gravity acceleration, and h is the height of the wave. Thus, a 10-m wave propagating with 1 m/s carries a power density of 49 kW/m.

If the waves are high, arrangements can be made in such a way that a difference of level can be created constantly through impoundment. Thus, the top of the wave carries waters over the impoundment constantly filling a small basin at a higher water level. The water-level difference is turned into shaft work by a Kaplan turbine system.

9.9 Concluding Remarks

In this chapter, renewable energy sources and the related energy conversion technologies were introduced for specific sources and applications. The renewable energy sources were classified into fundamental sources and energies derived from solar radiation (wind, waves, hydro, ocean thermal, and biomass energy). Solar energy, wind, geothermal, hydropower, biomass energy, and ocean energy were analyzed. The thermodynamic limits of renewable energy conversion into work were derived. Determining the energy and exergy efficiency of the processes was emphasized. The available technologies for converting renewable energies into work, heat, synthetic fuels, and hydrogen were analyzed. It appears that integrated hybrid systems show the potential for better renewable resource utilization and generating multiproducts.

Nomenclature

C	Concentration ratio
COP	Coefficient of performance
C_p	Power coefficient (−), specific heat (J/kg K)
e	Elementary electric charge (C)
$\dot{E}x$	Exergy rate (W)
FF	Filling factor
GCV	Gross calorific value (MJ/kg)
h	Specific enthalpy (J/kg) or (J/mol)
I	Irradiation (W/m^2), current intensity (A)
k_B	Boltzmann constant
LEC	Levelized electricity cost
M	Molecular mass (kg/kmol)
NCV	Net calorific value (MJ/kg)
Q	Heat (J)
R	Radius (m), resistance (Ω)
T	Temperature (K)
U	Heat transfer coefficient (W/m^2 K)
V	Voltage (V), velocity (m/s)
W	Work (J)
w	Moisture content

Greek Letters

α	Absorptivity
γ	Intercept factor
ε	Emissivity
η	Energy efficiency
μ	Chemical potential
ϕ	Subunitary factor
χ	Factor
ψ	Exergy efficiency
ρ	Reflectivity (−); density (kg/m^3)
ζ	Shading factor
σ	Stefan–Boltzmann constant (W/m^2 K^4)
τ	Transmissivity
θ	Dimensionless temperature
Ω	Solid angle
φ	Angle

Subscripts

0	Reference state
cog	Cogeneration
coll	Collector
db	Direct beam
e	Emitted or electric
diss	Dissipation
max	Maximum
oc	Open circuit
opt	Optical
PV	Photovoltaic
r	Receiver
rev	Reversible
S	Sun
SC	Solar constant
sc	Short circuit
T0	Tilted surface
th	Thermal

Superscripts

$(\dot{})$	Rate (per unit of time)
$()''$	Per unit of surface
$(\tilde{})$	Dimensionless

References

Avery W.H., Richards D., Dugger G.L. 1985. Hydrogen generation by OTEC electrolysis, and economical energy transfer to world markets via ammonia and methanol. *International Journal of Hydrogen Energy* 10:727–736.

Bejan A. 2006. Advanced Engineering Thermodynamics. Wiley, New York.

Burton T., Sharpe D., Jenkins N., Bossanyi E. 2001. Wind Energy Handbook. John Wiley and Sons, West Sussex.

Colpan C.O., Hamdullahpur F., Dincer I. 2010a. Solid oxide fuel cell and biomass gasification systems for better efficiency and environmental impact. Eighteenth World Hydrogen Energy Conference WHEC 16–21 May 2010, Essen, Germany.

Colpan C.O., Hamdullahpur F., Dincer I., Yoo Y. 2010b. Effect of gasification agent on the performance of solid oxide fuel cell and biomass gasification systems. *International Journal of Hydrogen Energy* 35:5001–5009.

Da Rosa A.V. 2009. Fundamentals of Renewable Energy Processes, 2nd ed. Elsevier, Burlington, MA.
Dincer I., Dilmac S., Ture I.E., Edin M. 1996a. A simple technique for estimating solar radiation parameters and its application for Gebze. *Energy Conversion and Management* 37:183–198.
Dincer I., Dost S. 1996. A perspective on energy storage systems for solar energy applications. *International Journal of Energy Research* 20:547–557.
Dincer I., Edin M., Ture E. 1996b. Investigation of thermal performance of a solar powered absorption refrigeration system. *Energy Conversion and Management* 37:51–58.
Granovskii M., Dincer I., Rosen M.A. 2006. Economic aspects of greenhouse gas emissions reduction by utilisation of wind and solar energies to produce electricity and hydrogen. IEEE EIC Climate Change Conference, pp. 1–5.
Joshi A.S., Dincer I., Reddy B.V. 2009a. Development of new solar exergy maps. *International Journal of Energy Research* 33:709–718.
Joshi A.S., Dincer I., Reddy B.V. 2009b. Performance analysis of photovoltaic systems: A review. *Renewable and Sustainable Energy Reviews* 13:1884–1897.
Joshi A.S., Tiwari A., Tiwari G.N., Dincer I., Reddy B.V. 2009c. Performance evaluation of a hybrid photovoltaic thermal (PV/T) (glass-to-glass) system. *International Journal of Thermal Sciences* 48:154–164.
Karakilcik M., Dincer I., Rosen M.A. 2006. Performance investigation of a solar pond. *Applied Thermal Engineering* 26:727–735.
Lee, K.C. 2001. Classification of geothermal resources by exergy. *Geothermics* 30:431–442.
Lund J.W. 2005. 100 years of geothermal power product. Proceedings Thirtieth Workshop on Geothermal Reservoir Engineering, Stanford University, Stanford, California, January 31–February 2, SGP-TR-176. Internet source http://iga.igg.cnr.it/index.php (accessed on September 15, 2009).
Markvart T., Landsberg P.T. 2002. Thermodynamics and reciprocity of solar energy conversion. *Physica E* 14:71–77.
O'Rourke F., Boyle F., Reynolds A. 2010. Tidal energy update 2009. *Applied Energy* 87:398–409.
Özgener L., Hepbasli A., Dincer I. 2005. Energy and exergy analysis of Salihli geothermal district heating system in Manisa, Turkey. *International Journal of Energy Research* 29:393–408.
Pope K., Dincer I., Naterer G.F. 2010. Energy and exergy efficiency comparison of horizontal and vertical axis wind turbines. *Renewable Energy* 35:2102–2113.
Sahin A.D., Dincer I., Rosen M.A. 2006. New spatio-temporal wind exergy maps. *Journal of Energy Resource Technology* 128:194–202.
Szargut J. 2005. Exergy Method. Technical and Ecological Applications. WIT Press, Boston.
Tiris G., Tiris M., Dincer I. 1995. Investigation of the thermal efficiencies of a solar drier. *Energy Conversion and Management* 36:205–212.
Van Loo S., Koopejan J. 2008. The Handbook of Biomass Combustion and Co-Firing. Earthscan, Sterling, VA.
Vargas J.V.C., Ordonez J.C., Zamfirescu C., Bejan A., Campos M.C. 2005. Optimization of the ground cooling of electronic packages. *Heat Transfer Engineering* 26:8–20.
Zamfirescu C., Dincer I. 2008a. How much work one can extract from incident solar radiation? *Journal of Applied Physics* 105/044911:1–5.
Zamfirescu C., Dincer I. 2008b. Thermodynamic analysis of a novel ammonia–water trilateral Rankine cycle. *Thermochimica Acta* 477:7–15.
Zamfirescu C., Dincer I., Verrelli T., Wagar W.R. 2008. Residential solar power generation systems for better environment. Proceedings of Global Conference on Global Warming, July 6–10, Istanbul, paper #805.
Zamfirescu C., Dincer I., Verrelli T., Wagar W.R. 2009. Environmental impact and cost analysis of residential systems for concentrated solar power and heat production. Proceeding of Global Conference on Global Warming, July 5–9, Istanbul, paper #531.

Study Questions/Problems

9.1 Explain and classify the renewable energies.
9.2 Describe the conversion paths of solar energy.
9.3 What is the thermodynamic limit of solar energy conversion with a blackbody receiver?
9.4 Define the exergy of solar radiation.
9.5 Define the concentration ratio.
9.6 Explain the existence of an optimum receiver temperature.
9.7 Calculate the optimum receiver temperature using Eq. (9.10) under reasonable assumptions.
9.8 Explain the concept of electric potential, chemical potential, and electrochemical potential and the differences among them.
9.9 Define the filling factor.
9.10 Comment on the utility of solar energy maps with respect to solar energy maps.
9.11 Describe the principle of operation of solar ponds.
9.12 Elaborate a calculation procedure of a flat plate solar collector for determining its efficiency.
9.13 Explain thermal and optical efficiency of solar concentrators and the difference between them.
9.14 Consider the system from Fig. 9.22a. Make reasonable assumption and calculate the cycle and its efficiency according to the first and second law of thermodynamics.
9.15 Explain the routes for solar-biochemical conversion.
9.16 Define the cogeneration efficiency of PV/T systems.
9.17 Consider the system described in Table 9.6. Make reasonable assumptions and calculate its efficiency under maximum solar radiation intensity.
9.18 Explain the wind-chill effect on the energy and exergy efficiency of wind turbines.
9.19 Comment on the role of wind exergy maps.
9.20 Describe the global utilization of geothermal energy.
9.21 Explain the thermodynamic limits of geothermal energy conversion.
9.22 Consider the system from Fig. 9.50. Make reasonable assumptions and calculate the cycle and determine its efficiency.
9.23 Consider the system from Fig. 9.52. Make reasonable assumptions and calculate the cycle and determine its efficiency.
9.24 Explain the advantage of ammonia–water in geothermal systems.
9.25 Using the ammonia–water diagram from Appendix B (Diagram B.5, p. 799), try to calculate the heat transfer process illustrated graphically in Fig. 9.53b.
9.26 Calculate the trilateral flash Rankine cycle with ammonia–water in EES or using the ammonia enthalpy diagrams.
9.27 A typical hydropower setting has a$\Delta z = 250\,\mathrm{m}$ level difference between the lake's surface and downstream waters. On the water stream with a volume

flow of $\dot{V} = 10{,}000\,\mathrm{dm}^3/\mathrm{s}$ a turbine coupled to an electric generator is installed that produces $\dot{W} = 9\,\mathrm{MW}$ power with $\eta_g = 99\%$ efficiency. Calculate the efficiency of the water turbine itself, the overall efficiency, and the power generated by the turbine.

9.28 Calculate the adiabatic flame temperature for a biomass having $X_C = 2$, hydrogen per carbon of 2, oxygen per carbon of 0.1, nitrogen per carbon of 0.4, sulfur per carbon of 0.1, and 20% moisture by weight.

9.29 For the above case, determine the maximum energy and exergy efficiency of combustion.

9.30 Consider the system from Fig. 9.63. Under reasonable assumptions calculate the cycle and determine its efficiency.